The Second *Swift* BAT Gamma-Ray Burst Catalog

T. Sakamoto[1,2,3], S. D. Barthelmy[3], W. H. Baumgartner[1,2,3], J. R. Cummings[1,2,3], E. E. Fenimore[4], N. Gehrels[3], H. A. Krimm[1,5,3], C. B. Markwardt[1,6,3], D. M. Palmer[4], A. M. Parsons[3], G. Sato[7], M. Stamatikos[8], J. Tueller[3], T. N. Ukwatta[9,3], B. Zhang[10]

ABSTRACT

We present the second *Swift* Burst Alert Telescope (BAT) catalog of gamma-ray bursts (GRBs), which contains 476 bursts detected by the BAT between 2004 December 19 and 2009 December 21. This catalog (hereafter the BAT2 catalog) presents burst trigger time, location, 90% error radius, duration, fluence, peak flux, time-averaged spectral parameters and time-resolved spectral parameters measured by the BAT. In the correlation study of various observed parameters extracted from the BAT prompt emission data, we distinguish among long-duration GRBs (L-GRBs), short-duration GRBs (S-GRBs), and short-duration GRBs with extended emission (S-GRBs with E.E.) to investigate differences in the prompt emission properties. The fraction of L-GRBs, S-GRBs and S-GRBs with E.E. in the catalog are 89%, 8% and 2% respectively. We compare the BAT prompt emission properties with the BATSE, *BeppoSAX* and *HETE*-2 GRB samples. We also correlate the observed prompt emission properties with the redshifts

[1]Center for Research and Exploration in Space Science and Technology (CRESST), NASA Goddard Space Flight Center, Greenbelt, MD 20771

[2]Joint Center for Astrophysics, University of Maryland, Baltimore County, 1000 Hilltop Circle, Baltimore, MD 21250

[3]NASA Goddard Space Flight Center, Greenbelt, MD 20771

[4]Los Alamos National Laboratory, P.O. Box 1663, Los Alamos, NM, 87545

[5]Universities Space Research Association, 10211 Wincopin Circle, Suite 500, Columbia, MD 21044-3432

[6]Department of Astronomy, University of Maryland, College Park, MD 20742

[7]Institute of Space and Astronautical Science, JAXA, Kanagawa 229-8510, Japan

[8]Center for Cosmology and Astro-Particle Physics, Department of Physics, The Ohio State University, 191 West Woodruff Avenue, Columbus, OH 43210

[9]Center for Nuclear Studies, Department of Physics, The George Washington University, Washington, D.C. 20052

[10]Department of Physics and Astronomy, University of Nevada, Las Vegas, NV 89154

for the GRBs with known redshift. The BAT T_{90} and T_{50} durations peak at 70 s and 30 s, respectively. We confirm that the spectra of the BAT S-GRBs are generally harder than those of the L-GRBs. The time-averaged spectra of the BAT S-GRBs with E.E. are similar to those of the L-GRBs. Whereas, the spectra of the initial short spikes of the S-GRBs with E.E. are similar to those of the S-GRBs. We show that the BAT GRB samples are significantly softer than the BATSE bright GRBs, and that the time-averaged $E^{\rm obs}_{\rm peak}$ of the BAT GRBs peaks at 80 keV which is significantly lower energy than those of the BATSE sample which peak at 320 keV. The time-averaged spectral properties of the BAT GRB sample are similar to those of the *HETE*-2 GRB samples. By time-resolved spectral analysis, we find that 10% of the BAT observed photon indices are outside the allowed region of the synchrotron shock model. The observed durations of the BAT high redshift GRBs are not systematically longer than those of the moderate redshift GRBs. Furthermore, the observed spectra of the BAT high redshift GRBs are similar to or harder than the moderate redshift GRBs. The T_{90} and T_{50} distributions measured at the 140-220 keV band in the GRB rest frame form the BAT known redshift GRBs peak at 19 s and 8 s, respectively. We also provide an update on the status of the on-orbit BAT calibrations.

Subject headings: gamma rays: bursts

1. Intruduction

The *Swift* mission (Gehrels et al. 2004) has revolutionized our understanding of gamma-ray bursts (GRBs) and their usage to study the early universe with the sophisticated on-board localization capability of the *Swift* Burst Alert Telescope (BAT; Barthelmy et al. (2005a)), the autonomously spacecraft slewing to point the X-Ray Telescope (XRT;Burrows et al. (2005a)), the UV/Optical Telescope (UVOT; Roming et al. (2005)) to the GRB location, and by the coordinations with multi-wavelength observatories on the ground. Since the release of the first BAT GRB catalog (Sakamoto et al. 2008), there have been more notable discoveries. On April 23, 2009, *Swift* BAT detected GRB 090423 at a redshift of 8.2. This implies that massive stars were produced about 630 Myr after the Big Bang (Tanvir et al. 2009; Salvaterra et al. 2009). Extraordinary bright variable optical emission, which peaked at the visual magnitude of 5.3, has been observed while the prompt gamma-ray emission was still active for GRB 080319B. This observation suggests for the first time that there can exist a prompt optical emission component that tracks the gamma-ray light curve but belongs to a different spectral component. *Swift* has been increasing the identifications of host galaxies

for short duration bursts. Based on the Swift samples, we are realizing a wide variety in their characteristics (e.g., Berger 2009). Furthermore, the properties of the host galaxies of optically dark GRBs are in progress for the Swift GRBs. Investigations of the host galaxies of dark GRBs are important to understand the different environment of the GRB birth place comparing to GRBs with bright optical afterglows (e.g,. Perley et al. 2009).

The first BAT GRB catalog (the BAT1 catalog; Sakamoto et al. (2008)) consisted of 237 bursts from 2004 December 19 to 2007 June 16. The BAT1 catalog contained burst trigger time, location, 90% error radius, duration, fluence, peak flux and time-averaged spectral parameters for 237 GRBs as measured by BAT. Here we present the second BAT GRB catalog (the BAT2 catalog), including 476 GRBs detected by BAT from 2004 December 19 to 2009 December 21. The GRB samples in the BAT1 catalog have been re-analyzed by the latest BAT software and calibration files. In addition to the parameters in the BAT1 catalog, the BAT2 catalog includes time-resolved spectral parameters. The catalog shows correlations between the prompt emission properties and the redshifts of known redshift GRBs.

In §2, we summarize the updates to the in-orbit calibration of the BAT instrument. In §3, we describe the analysis methods for the catalog. In §4, we describe the content of the tables in the catalog and show the prompt emission properties of the BAT GRBs from the catalog. Our conclusions are summarized in §5. All quoted errors in this work are at the 90% confidence level.

2. Updates to In-orbit Calibrations

The BAT is a highly sensitive, large field of view (FOV) (2.2 sr for $> 10\%$ coded FOV), coded-aperture telescope that detects and localizes GRBs in real time. The BAT detector plane is composed of 32,768 pieces of CdZnTe (CZT: $4 \times 4 \times 2$ mm), and the coded-aperture mask is composed of $\sim$ 52,000 lead tiles ($5 \times 5 \times 1$ mm) with a 1 m separation between mask and detector plane. The energy range is 14–150 keV for imaging or mask-weighting, which is a technique to subtract the background based on the modulation resulting from the coded mask, and there is also a non-coded response up to 350 keV. Further detailed descriptions, references and the in-orbit calibration status of the BAT can be found in the BAT1 GRB catalog.

There have been two major updates to the energy calibration of the BAT since the publication of the BAT1 catalog. The first update is the identification of the problem in the energy response above 100 keV. The mobility-lifetime products of electrons and holes

($\mu\tau$) which are used to model the energy response of an individual CZT detector(Sato et al. 2005; Suzuki et al. 2005) are 1.7 times larger than those originally determined. This fix eliminates the correction which we were applying above 100 keV to reproduce the canonical Crab spectrum and also reduces the level of systematic errors (see Figure 1).

The second update is a correction to the measured gain of the detectors. An analysis of four years of on-board ^{241}Am spectra shows a shift in the 59.5 keV line of 2.5 keV. The BAT team has developed new calibration files (coefficient to convert from PHA channel to energy) to correct this gain change as a function of time. After applying the new gain correction, the scatter of the 59.5 keV line energy is $\sim$0.1 keV over the four-year period.

Figure 2 shows the Crab photon index and the flux in the 15-150 keV band as a function of the incident angle using the latest BAT software and calibration files. Both the photon index and the flux are within $\pm$5% and $\pm$10% respectively of the canonical Crab values over the BAT field of view. The deviation of the derived parameters from the Crab canonical values are larger toward the edge of the BAT field of view. Therefore, a larger systematic error in the spectral parameters could exist if the source is located at the edge of the field of BAT. We also notice that the photon index is systematically harder by $\sim$0.02 than the Crab canonical value of -2.15 for observations of $\theta < 10°$.

3. Analysis for the GRB catalog

We used standard BAT software (HEASOFT 6.8) and the latest calibration database to process the BAT GRBs from December 2004 (GRB 041217) to December 2009 (GRB 091221). The GRBs included in the BAT1 catalog have been reprocessed. The BAT2 catalog sample also include bursts which were found in ground processing. The burst pipeline script, `batgrbproduct`, was used to process the BAT event data. Since the burst emissions are longer than the duration of the event data for GRB 060124 and GRB 060218, we used both the event data and the survey data (Detector Plane Histogram data) to calculate the fluence and the time-averaged spectral parameters. We used raw light curve data (quad-rate data) to measure the duration of most of the bursts found using ground data because the event data are incomplete for these bursts. In some cases, `battblocks`, which is one of the task runs in `batgrbproduct`, failed to find the burst interval. In those cases, we fitted the mask-weighted light curve in the full BAT energy range with a liner-rise exponential decay model ("BURS" model in ftools qdp[1]) to find the burst time intervals (T_{100}, T_{90}, T_{50} and peak 1-s intervals) and created the T_{100} and peak 1-s PHA files based on these time intervals.

[1]http://heasarc.gsfc.nasa.gov/docs/software/ftools/others/qdp/qdp.html

We put comments in Table 1 for the bursts which have a problem in either the data or the processing.

For the time-averaged spectral analysis, we used the time interval from the emission start time to the emission end time (T_{100} interval). Since the BAT energy response generator, `batdrmgen`, uses a single fixed incident angle of the source, it is not appropriate to use the response at the fixed position if the GRB location at the detector plane is changing due to the spacecraft slewing. To take into account this problem, we created the detector energy response matrices (DRM) for each five-second period during the time interval taking into account the changing position of the GRB in detector coordinates especially during the spacecraft slew. We then weighted these DRMs by the five-second count rates and created an averaged DRM using `addrmf`. The weighted BAT DRM have been tested on a subset of GRBs which were simultaneously detected by the Konus-Wind and the *Suzaku* Wide-band All-sky Monitor instruments. The joint spectral analysis using the weighted BAT DRM for those GRBs shows no systematic trend in the derived parameters compared to the spectral parameters derived by other GRB instruments (Sakamoto et al. 2010).

We extracted the time-resolved spectra for the intervals determined with `battblocks`. `battblocks` determines the interesting time intervals based on time variable events or rate data using the Bayesian Block algorithm (Scargle 1998). Since the first and the last intervals identified by `battblocks` are the pre- and post-burst backgrounds, the spectrum for these two intervals were not created. For the time-resolved spectral analysis, we created a DRM for each spectrum by taking into account the GRB position in detector coordinates and updating the keywords of the spectral files using `batupdatephakw` before running `batdrmgen` to generate the DRM. We also created individual DRMs for the peak spectra used to calculate the peak flux (see below).

The spectra were fitted with a simple power-law (PL) model,

$$f(E) = K_{50}^{\rm PL} \left(\frac{E}{50\,{\rm keV}} \right)^{\alpha^{\rm PL}} \tag{1}$$

where $\alpha^{\rm PL}$ is the power-law photon index and $K_{50}^{\rm PL}$ is the normalization at 50 keV in units of photons cm^{-2} s^{-1} keV^{-1}. We also used a cutoff power-law (CPL) model,

$$f(E) = K_{50}^{\rm CPL} \left(\frac{E}{50\,{\rm keV}} \right)^{\alpha^{\rm CPL}} \exp\left(\frac{-E\,(2+\alpha^{\rm CPL})}{E_{\rm peak}} \right) \tag{2}$$

where $\alpha^{\rm CPL}$ is the power-law photon index, $E_{\rm peak}$ is the peak energy in the $\nu {\rm F}_\nu$ spectrum and $K_{50}^{\rm CPL}$ is the normalization at 50 keV in units of photons cm^{-2} s^{-1} keV^{-1}. All of the BAT spectra are acceptably fit by either a PL or a CPL model. The same criteria as in the

BAT1 catalog, $\Delta\chi^2$ between a PL and a CPL fit greater than 6 ($\Delta\chi^2 \equiv \chi^2_{\rm PL} - \chi^2_{\rm CPL} > 6$), was used to determine if the CPL model is a better spectral model for the data. Note that none of the BAT spectra show a significant improvement in χ^2 with a Band function (Band et al. 1993) fit compared to that of a CPL model fit.

The fluence, the 1-s and the 20-ms peak fluxes were derived from the spectral fits. The fluences were calculated by fitting the time-averaged spectrum with the best fit spectral model. The 1-s and 20-ms peak fluxes were calculated by fitting the spectrum of the 1-s and the 20 ms interval bracketing the highest peak in the light curve. Those intervals were identified by `battblocks`. Similarly, we used the best fit spectral model to calculate the peak fluxes. Since the shortest burst duration observed by BAT is around 20 ms, we choose this window size to measure the peak flux on the shortest time scale. Note that since the total number of photons for a 20-ms spectrum is generally small, we created a spectrum in 10 logarithmically spaced channels from 14 keV to 150 keV to use for the fit. Since the duration of the 20-ms spectrum is extremely short, the spectral analysis of 29 GRBs shows an unacceptable reduced χ^2 ($\chi^2_\nu > 2$) in both the PL and CPL fit. Furthermore, 31 GRBs could not create the 20-ms peak spectrum because `battblocks` failed to find the interval.

For GRBs with known redshift, we calculated the T_{90} and T_{50} durations in the 140-220 keV band at the GRB rest frame. By fixing the energy range in the GRB rest frame, there is no need to apply a correction to the measured duration because of the difference in the GRB width as a function of the observed energy band (e.g., Fenimore et al. 1995). We created the light curves in the energy range 140/(1+z) keV to 220/(1+z) keV with `batbinevt`. This energy band has been determined as a compromise between the redshift range of 0.1257 (GRB 060614) ,which constrains the upper boundary of 220 keV (220 keV / (1+0.1257) = 195 keV), to 8.26 (GRB 090423), which constrains the lower boundary of 140 keV (140 keV / (1+8.26) = 15 keV), and the BAT observed energy range of 14 keV to 150 keV. We used the same algorithm in `batgrbproduct` [2] to find the best T_{90} and T_{50} durations in the observed 140/(1+z) - 220/(1+z) keV band. Then, we divided the duration by (1+z) to correct for the time dilation effect due to cosmic expansion.

---

[2] `batgrbproduct` calls `battblocks` with inputting 4 ms, 16ms, 1s and 16s bin mask-weighted light curve to measure T_{90} and T_{50} durations. Then it applies a set of criteria starting from the shortest bin size to decide whether to accept a duration estimate or not. If a measured duration is greater than 2 times the bin size, and 30% greater than the previous best estimate, then current estimate becomes the new best estimate.

4. The Catalog

The BAT2 catalog includes GRBs detected by BAT in five years of operation between 2004 December 19 and 2009 December 31. The 476 GRBs in the catalog include 25 GRBs found in ground processing (eight of the 25 were found by the BAT slew survey; Copete et al. (2007)) and four possible GRBs. 476 GRBs are listed in Table 1. The first column is the GRB name. The next column is the BAT trigger number. The next column specifies the BAT trigger time in UTC in the form of *YYYY-MM-DD hh:mm:ss.sss* where *YYYY* is year, *MM* is month, *DD* is day of month, *hh* is hour, *mm* is minute, and *ss.sss* is second. Note that the definition of the BAT trigger time is the start time of the foreground time interval of the image from which the GRB is detected on-board. The next four columns give the locations derived by the ground process [3] in equatorial (J2000) coordinates, the signal-to-noise ratio of the BAT image at that location, and the radius of the 90% confidence region in arcmin. The 90% error radius is calculated based on the signal-to-noise ratio of the image using the following equation derived from the BAT hard X-ray survey process[4]

$$r_{90\%} = 10.92 \times \mathrm{SNR}^{-0.7} \ (\mathrm{arcmin}),$$

where SNR is the signal-to-noise ratio of the BAT image. However, due to the limitation of the BAT point spread function, we quote the minimum allowed value of $r_{90\%}$ as $1'$ in the catalog. The next two columns specify the burst durations which contain from 5% to 95% (T_{90}) and from 25% to 75% (T_{50}) of the total burst fluence. These durations are calculated in the 15–350 keV band.[5] The next two columns are the start and stop time from the BAT trigger time of the event data. The last column contains the comments.

The energy fluences calculated in various energy bands are summarized in Table 2. The first column is the GRB name. The next column specifies the spectral model which was used in deriving the fluences (PL: simple power-law model; Eq.(1), CPL: cutoff power-law model; Eq.(2)). The next five columns are the fluences in the 15-25 keV, the 25-50 keV, the 50-100 keV, the 100-150 keV, and the 15-150 keV bands. The unit of fluence is 10^{-8} ergs cm^{-2}. The next two columns specify the start and the stop time relative to the BAT trigger time

---

[3] `batgrbproduct` creates the BAT sky image in the 15-350 keV band using the event data before the autonomous spacecraft slew to a GRB location. The foreground and background intervals to create the image are determined by `battblocks`. If `battblocks` failed to find the intervals, `batgrbproduct` uses the same intervals which identified by the BAT on-board software.

[4] http://heasarc.gsfc.nasa.gov/docs/swift/analysis/bat_digest.html

[5] The coded mask is transparent to photons above 150 keV. Thus, photons above 150 keV are treated as background in the mask-weighted method. The effective upper boundary is $\sim$ 150 keV.

which was used to calculate the fluences. The last column contains the comments. Note that fluences are not reported for GRBs with incomplete data.

Table 3 and 4 summarize the 1-s peak photon and energy fluxes in various energy bands. The first column is the GRB name. The next column specifies the spectral model used in deriving the 1-s peak flux. The next five columns are the peak photon and energy fluxes in the 15-25 keV, the 25-50 keV, the 50-100 keV, the 100-150 keV, and the 15-150 keV band. The unit of the flux is photons cm^{-2} s^{-1} for the peak photon flux and 10^{-8} ergs cm^{-2} s^{-1} for the peak energy flux. The last two columns in Table 3 specify the start and the stop time relative to the BAT trigger time which were used to calculate the peak fluxes. The last column contains the comments.

Table 5 shows the 20-ms peak energy and photon flux in the 15-150 keV band. The first column is the GRB name. The next column shows the spectral model used in deriving the flux. The next two columns are the peak energy flux and photon flux in the 15-150 keV band. The unit of the flux is photons cm^{-2} s^{-1} for the peak photon flux and 10^{-8} ergs cm^{-2} s^{-1} for the peak energy flux. The next two columns specify the start and the stop time relative to the BAT trigger time which were used to calculate the 20-ms peak flux. The last column contains the comments.

The time-averaged spectral parameters are listed in Table 6. The first column is the GRB name. The next three columns are the photon index, the normalization at 50 keV in the unit of 10^{-4} photons cm^{-2} s^{-1} keV^{-1}, and χ^2 of the fit for a PL model. The next four columns are the photon index, $E^{\rm obs}_{\rm peak}$ in the unit of keV, the normalization at 50 keV in the unit of 10^{-3} photons cm^{-2} s^{-1} keV^{-1} and χ^2 of the fit in a CPL model. The spectral parameters in a CPL are only shown for the bursts which meet the criteria described in the section 3. The degree of freedom is 57 for a PL fit and 56 for a CPL fit except for GRB 060124 and GRB 060218 (see the comment column of the table). The last column contains the comments.

The time-resolved spectral parameters are listed in Table 7. The total number of time-resolved spectra is 3323. The first column is the GRB name. The next two columns specify the start and the stop time relative to the BAT trigger time which were used to extract the spectrum. The next four columns are the photon index, the normalization at 50 keV in the unit of 10^{-4} photons cm^{-2} s^{-1} keV^{-1}, χ^2 and the energy flux in the 15-150 keV band in the unit of 10^{-8} ergs cm^{-2} s^{-1} of the fit for a PL model. The next five columns are the photon index, $E^{\rm obs}_{\rm peak}$ in the unit of keV, the normalization at 50 keV in the unit of 10^{-3} photons cm^{-2} s^{-1} keV^{-1}, χ^2, and the energy flux in the unit of 10^{-8} ergs cm^{-2} s^{-1} of the fit in a CPL model. The last column contains the comment. Similar to the table of the time-averaged spectral parameters, we only show CPL parameters for the fits which meet our $\Delta\chi^2$ criteria.

Table 8 shows the T_{90} and T_{50} durations measured in the 140-220 keV band at the GRB rest frame for the GRBs with known redshift. The first column is the GRB name. The T_{90} and T_{50} durations at the GRB rest frame are in the second and the third columns. The last column contains the comments.

Table 9 lists redshift measurements of *Swift* GRBs and their associated references.

4.1. Short GRB with Extended Emission

A distinct class of short duration GRBs (S-GRBs) has been claimed based on their prompt emission properties, called S-GRB with extended emission (E.E.)(e.g., Norris et al. 2000; Barthelmy et al. 2005b). The initial short spike of a S-GRB with E.E. shows negligible spectral lag which is one of the strong indications that the burst is a S-GRB (Norris et al. 2000). We identified 10 S-GRBs with E.E. in our catalog from the samples in Norris et al. (2010)[6]. The BAT light curves of 10 S-GRBs with E.E. included in this catalog are shown in Figure 3. The initial short spike is usually composed of multiple pulses with a total duration of less than 2 seconds. The E.E. lasts from a few tens to a few hundreds of seconds. We distinguish among long GRBs (L-GRBs), S-GRBs and a S-GRBs with an E.E. throughout the paper to investigate the prompt emission properties of these three different classes of GRBs. The spectral parameters and the energy fluences of the initial short spike are reported in Table 11 and 12. Note that our definition of S-GRBs is whether T_{90} is smaller than 2 s or not. The GRBs classified as S-GRBs or S-GRBs with E.E. in our study are identified in Table 1. Table 10 summarizes the statistics of the samples in the catalog based on the classifications. The fractions of L-GRBs, S-GRBs and S-GRBs with E.E. in the catalog are 89%, 8% and 2% respectively.

4.2. BAT GRB Position and Sky Locations

Figure 4 shows the angular difference between the BAT ground position and the enhanced XRT position (Evans et al. 2009). The BAT ground position is within 1.1′, 1.8′ and 3.5′ from the XRT position for 68%, 90% and 99% of the bursts, respectively.

Figure 5 shows the sky map of the 476 BAT GRBs in galactic coordinates. L-GRBs,

[6]GRB 060614 is classified as a L-GRB because the duration of the initial spike is ∼6 s long. GRB 050911 is also classifed as a L-GRB because our standard pipeline process does not detect the significant extended emission as reported on Norris et al. (2010). The T_{90} of GRB 050911 based on our analysis is 16.2 s.

S-GRBs and S-GRBs with E.E. are marked in different colors. All GRBs are distributed uniformly in the sky. However, we do notice that several S-GRBs are located along the galactic plane region. These S-GRBs could be good candidates for previously unknown Soft Gamma-ray Repeaters or Anomalous X-ray Pulsars (e.g., Palmer et al. 2005; Sakamoto et al. 2009a).

4.3. Durations and Hardness

The histograms of T_{90} and T_{50} in the BAT full energy band are shown in Figure 6. The average of the BAT T_{90} and T_{50} durations are 71 and 31 s, respectively. In Figure 7, we compare the T_{90} distributions of BAT, BATSE, *BeppoSAX* and *HETE*-2. The BATSE T_{90} are extracted from the 4B catalog (Paciesas et al. 1999), and they are measured in the 50-300 keV band. The *BeppoSAX* T_{90} are extracted from Frontera et al. (2009), and they are measured using the light curve of the GRBM instrument in the 40-700 keV band. The *HETE*-2 T_{90} are extracted from Pélangeon et al. (2008), and they are measured using the light curve of the FREGATE instrument in the 6-80 keV band. There is a clear shift in the peak of the L-GRB populations measured with different instruments. The peak of L-GRBs T_{90} distribution from the BATSE, the *BeppoSAX* and the *HETE*-2 samples are around 10-30 s, whereas the BAT distribution is around 70 s. It is clear from this comparison that the duration measurement depends upon the sensitivity of the instruments. Another distinct difference in the BATSE distribution compared to that of the BAT, the *BeppoSAX* and the *HETE*-2 distributions is a clear bimodality between S-GRBs and L-GRBs (e.g., Kouveliotou et al. 1993). The lack of S-GRBs in imaging instruments such as the BAT and *HETE*-2 is a result of the larger number of photons needed to "image" a GRB with these instruments. This requirement is usually difficult to achieve for S-GRBs because they are usually faint and their emissions are short. However, note that BAT has been triggering and localizing S-GRBs at a much higher rate than other GRB imaging instruments because of its large effective area and its sophisticated flight software. As mentioned in Frontera et al. (2009), the lack of S-GRBs in the *BeppoSAX* samples is likely to be due to the lower efficiency of the trigger system to S-GRBs.

Figure 8 shows the fluence ratio between the 50-100 keV and the 25-50 keV band versus the T_{90} and T_{50} durations of the BAT GRBs. It is clear from the figures that there is not a large number of S-GRBs that have soft spectra. Most of the S-GRBs have a fluence ratio of about 2. On the other hand, the averaged fluence ratio of the L-GRBs is 1.3. Based on this comparison, we can conclude that the S-GRBs are generally harder than the L-GRBs. However, note that there is a large overlap in the hardness between L-GRBs and S-GRBs in

the BAT sample. The S-GRBs with E.E. overlap the L-GRB samples.

The comparisons in the fluence ratio-T_{90} plane for the BAT, the BATSE, the *BeppoSAX* the *HETE*-2 GRBs are shown in Figure 9. Both fluences and T_{90} values for the BATSE sample are extracted from the 4B catalog. For the *BeppoSAX* sample, we used the best fit simple power-law model in the catalog (Frontera et al. 2009) to calculate the fluence ratios in the 50-100 keV and the 25-50 keV band. For the *HETE*-2 sample, we calculated the fluences in those energy bands using the spectral parameters reported in Sakamoto et al. (2005) and Pélangeon et al. (2008). We only calculated the fluences for sources listed with CPL or Band parameters.[7] The T_{90} values of the *HETE*-2 sample are from Pélangeon et al. (2008). As seen in Figure 9, although the GRB samples of different missions are overlaid each other, there is a large scatter in the BATSE sample especially in the hardness of the S-GRBs. This could be either because the BATSE was detecting a wider population of GRBs than other missions or because there is a systematic problem in the reported fluence values in the 4B catalog.

4.4. Peak Fluxes and Fluences

Figure 10 shows the 1-s and the 20-ms peak photon fluxes versus the fluence in the 15-150 keV band. As we showed in the BAT1 catalog, there is a positive correlation between these two parameters. Based on the correlation between the 20 ms peak flux and the 15-150 keV fluence (lower panel of Figure 10), it is now clear that most of the BAT S-GRBs are populated in a low fluence but a high peak flux region. The systematically lower 1-s peak flux than the 20-ms peak flux for the S-GRBs is because the 1-s time window is usually larger than the actual S-GRB duration for calculating the flux. The S-GRB population with low fluences and high peak fluxes for the BAT samples could be due to the selection effect of the imaging requirement in the trigger algorithm.

The fluence in the 50-150 keV band versus that in the 15-50 keV band for the BAT GRBs is shown in the top of Figure 11. Assuming a Band function with a low energy photon index of -1 and a high energy photon of -2.5, 43% of the BAT GRBs have $E_{\rm peak}^{\rm obs} > 100$ keV , 50% of the BAT GRBs have 30 keV $< E_{\rm peak}^{\rm obs} \leq 100$ keV, and 7% of the BAT GRBs have $E_{\rm peak}^{\rm obs} \leq 30$ keV. The similar number of GRBs in the range $E_{\rm peak}^{\rm obs} > 100$ keV and 30 keV $< E_{\rm peak}^{\rm obs} \leq 100$ keV is consistent with the *HETE*-2 GRB sample (Sakamoto et al. 2005). The systematically smaller number of GRBs with a soft spectrum ($E_{\rm peak}^{\rm obs} \leq 30$ keV) is likely

[7]Because of this spectral model requirement, we are excluding a large number of X-ray flashes in the *HETE*-2 sample where a PL is the usual accepted model.

due to a lack of the sensitivity below 15 keV with the BAT. The S-GRBs generally have low fluences with hard spectra with a small overlap with the L-GRBs properties. On the other hand, the S-GRBs with E.E. lie in the same region as the L-GRBs. However, the initial short spikes of the S-GRBs with E.E. have the similar characteristics of the S-GRBs. The bottom of Figure 11 compares the BAT, the BATSE, and the *HETE*-2 GRBs in the same fluence-fluence plane. The fluences for the BATSE sample and the *HETE*-2 are calculated using the best fit spectral parameters of a CPL model and a Band function as reported in Kaneko et al. (2006) and Pélangeon et al. (2008). The majority of the BATSE bursts have high fluences with hard spectra. The *HETE*-2 and the BAT samples have a similar characteristics in the fluences.

4.5. Time-averaged Spectral Parameters

Figure 12 shows the histograms of the BAT time-averaged photon index from a PL fit for L-GRBs, S-GRBs, S-GRBs with E.E. and the initial short spikes of the S-GRBs with E.E. A Gaussian fit to the histogram of PL photon indices of L-GRBs shows a peak at -1.6 with a σ of 0.3. This BAT photon index based on a PL fit is systematically steeper than the typical low-energy photon index α (~ -1) and also shallower than the high-energy photon index β (~ -2.5) based on a Band function fit (e.g., Kaneko et al. 2006). As demonstrated in the detailed spectral simulation study of Sakamoto et al. (2009b), the distribution of the BAT photon index in a PL fit reflects the fact that more than half of $E^{\rm obs}_{\rm peak}$ in BAT GRBs are located within the BAT energy range (15-150 keV). This is consistent with the discussion in section 4.4 that 50% of $E^{\rm obs}_{\rm peak}$ in the BAT GRBs are located 30 keV $< E^{\rm obs}_{\rm peak} \leq$ 100 keV assuming typical spectral parameters from a fit to a Band function. The histogram of PL photon indices of S-GRBs has a shift toward a shallower index compared to that of the L-GRBs. The time-averaged PL photon index for the S-GRBs is -1.2. We used a Kolmogorov-Smironov (K-S) test to check whether the L-GRBs and the S-GRBs are drawn from the same population. The K-S test statistics of 10^{-7} strongly indicates that the time-averaged PL photon index distributions of the L-GRBs and S-GRBs are different. Although the number of samples is limited, the time-averaged PL photon index of S-GRBs with E.E. is consistent with the L-GRBs. On the other hand, the PL photon index of the initial short spikes of the S-GRBs with E.E. is much more consistent with that of the S-GRBs.

Figure 13 shows the BAT time-averaged photon index from a PL fit versus the fluence in the 15-150 keV band. Similar to the trend in Figure 11 and 12, the S-GRBs are located in a lower fluence and a harder spectral region compared to the L-GRBs. The time-averaged properties of the S-GRBs with E.E. overlay the L-GRBs in the PL photon index - fluence

plane. The initial short spikes of the S-GRBs with E.E. seem consistent with the properties of S-GRBs in this plane, but in a systematically higher fluence region than the S-GRBs.

The low-energy photon index α and $E^{\rm obs}_{\rm peak}$ from a CPL fit are shown for the BAT, the BATSE and the *HETE*-2 GRBs in Figure 14. 77 out of 456 time-averaged spectra (17%) show a significant improvement of χ^2 in a CPL fit over a PL fit ($\Delta\chi^2 > 6$). The BATSE and the *HETE*-2 spectral parameters from a CPL fit are taken from Kaneko et al. (2006) and Pélangeon et al. (2008) respectively. The low-energy photon index α is consistent among the all instruments. However, most of the $E^{\rm obs}_{\rm peak}$ of the BATSE GRBs are larger than 100 keV, whereas the majority of $E^{\rm obs}_{\rm peak}$ in the BAT and the *HETE*-2 GRBs are less than 100 keV. This is more clearly represented in the histograms of $E^{\rm obs}_{\rm peak}$ shown in Figure 15. The Gaussian fits to the log-normal $E^{\rm obs}_{\rm peak}$ histograms of the BAT, the BATSE and the *HETE*-2 samples reveal the peaks to be at 79 keV, 320 keV, and 65 keV with σ in $\log(E^{\rm obs}_{\rm peak})$ of 0.18, 0.22, and 0.31 respectively. The K-S test probabilities in the log-normal $E^{\rm obs}_{\rm peak}$ distributions for the BAT and the BATSE, and the BAT and the *HETE*-2 are 9×10^{-21} and 0.15 respectively. As clearly seen in these histograms, although the peak and the width of the $E^{\rm obs}_{\rm peak}$ distributions differ among the instruments, they are overlapping. Moreover, there is no sign of a bimodal $E^{\rm obs}_{\rm peak}$ distribution in the measurements from a single instrument. Therefore, we may conclude that "true" $E^{\rm obs}_{\rm peak}$ has a single broad log-normal distribution. The difference of the $E^{\rm obs}_{\rm peak}$ distributions among the GRB instruments is very likely due to an instrumental selection effect.

4.6. Time-resolved Spectral Parameters

We have chosen 3284 out of 3323 spectra based on the goodness of the fit ($\chi^2_\nu < 2$) and also the constrains of the spectral parameters in the BAT time-resolved spectral study. Figure 16 compares the distributions of the photon index in a PL fit between the time-resolved and the time-averaged spectra. The best fit parameters in the Gaussian fit to those histograms have a peak at -1.53 with σ of 0.47 and a peak at -1.57 with σ of 0.32 for the time-resolved and the time-averaged spectra respectively. The K-S test probability for the time-resolved and the time-averaged PL photon index distribution is 10^{-4}. Therefore, there is a marginal difference in the photon index of a PL fit between the time-resolved and the time-averaged spectra especially in the widths of their distributions.

Figure 17 shows the differences of $E^{\rm obs}_{\rm peak}$ in a CPL fit between the time-resolved and the time-averaged spectra. 472 out of 3284 time-resolved spectra show a significant improvement of χ^2 in a CPL fit over a PL fit ($\Delta\chi^2 > 6$). The Gaussian fits to those log-normal $E^{\rm obs}_{\rm peak}$ histograms show a peak at 68 keV with $\log(E^{\rm obs}_{\rm peak})$ of 0.23 and a peak at 77 keV with

$\log(E^{\rm obs}_{\rm peak})$ of 0.19 between the time-resolved and the time-averaged spectra. We found a K-S probability of 0.04 for the comparison in $E^{\rm obs}_{\rm peak}$ distributions between the time-resolved and the time-averaged spectra. Therefore, there is no significant difference between $E^{\rm obs}_{\rm peak}$ based on a CPL fit in the BAT time-resolved and the time-averaged spectra.

Ghirlanda et al. (2009) suggested a possible resemblance between the low-energy photon index α of the S-GRBs and the initial part of the spectrum of the L-GRBs in the BATSE GRBs. Figure 12 shows a significant difference in the time-averaged photon index in a PL fit in the BAT data between the L-GRBs and the S-GRBs. Therefore, it is worth investigating this properties using our time-resolved spectral results. Figure 18 shows the histograms of the BAT photon index in a PL fit for the initial spectra of the L-GRBs and the time-averaged photon index of the S-GRBs. The K-S test probability comparing the initial PL photon indices of the L-GRBs and the time-averaged photon indices of the S-GRBs is 0.02. Furthermore, the K-S test probability comparing the initial PL photon indices of the L-GRBs and the time-averaged photon indices of the L-GRBs is 0.002. Therefore, the K-S test shows a weak indication that the PL photon indices in the initial intervals of the L-GRBs and the time-averaged PL photon indices of the S-GRBs are drawn from the same parent population.

One of the important questions about prompt emission from GRBs is whether the observed spectrum is correctly represented by the synchrotron shock model (SSM) or not (Rees & Mészáros 1992; Sari et al. 1996). According to Preece et al. (1998), 23% of the BATSE time-resolved spectra have low-energy photon indices which violate the SSM limit (the so called "line of death" problem). Although the BAT photon index based on a PL fit does not represent the low-energy photon index α of the Band function if $E^{\rm obs}_{\rm peak}$ is located inside the BAT energy range (see section 4.5), the BAT photon index should be the actual low energy photon index α if $E^{\rm obs}_{\rm peak}$ is located above the BAT energy range. Therefore, even if the photon index is derived by a PL fit, the BAT time-resolved spectra are the interesting dataset to investigate the line of death problem. Figure 19 shows the BAT photon index versus the energy flux in the 15-150 keV band of using time-resolved spectra with a PL fit. We only used the results for which the 90% error of the photon index has been constrained within ± 0.5. Out of 2968 points in the figure, 18 spectra (0.6%) are exceeding the hard side of the line of death ($>-2/3$) either in $>1.6\ \sigma$ or $\geq 3.2\ \sigma$ level. Figure 20 shows the distribution of the low-energy photon index α versus $E^{\rm obs}_{\rm peak}$ of the BAT time-resolved spectra for which there is a significant improvement of χ^2 in a CPL fit over a PL fit. Same as in the PL fit samples, we only used spectra where the low-energy photon index α is within ± 0.5 at the 90% confidence level. The low-energy photon index of 23 out of 234 spectra are harder than $-2/3$ in $>1.6\ \sigma$ or $\geq 3.2\ \sigma$ level. There is only one time-resolved spectrum (GRB 090618 from 110.5 s to 112.272 s from the trigger time) which violates the softer side of the line of death ($<-3/2$) at the significance level of $>1.6\ \sigma$. Therefore, the total fraction of the

BAT spectra in the CPL samples which violate the line of death is 10%. Although there are the spectra which violate the line of death in the BAT data, it is likely that the number of the BAT spectra which violate the limit is a factor of two smaller than the BATSE result. Figure 21, 22 and 23 show the BAT light curves with hatches for the time intervals exceeding the line of death. We noticed that the intervals exceeding the line of death are in a bright spike in the light curve. Furthermore, in some bursts, the rising part of the light curve (e.g. GRB 080318B) exceeds the limit. Although it is hard to conclude which part of the light curve violates the line of death because of the small number of samples in our study, we do see a general trend that 1) a bright peak and 2) a rising part of a peak in the light curve tend to exceed the line of death limit. This is consistent with the BATSE results that the initial part of the FRED pulses tend to violate the line of death (Lu et al. 2010).

The *Fermi* GRB 090902B which has a strong GeV detection by the Large Area Telescope shows the presence of underlining power-law component addition to the Band function component in the time-resolved spectra (Abdo et al. 2009). The extra power-law component emerges not only in the GeV energy range but also in <50 keV energy range in the observed spectra. To investigate such a spectral feature in the BAT time-resolved spectra, we perform BAT spectral simulations by inputing the spectral parameters of the interval b (from 4.6 s to 9.6 s) reported in Abdo et al. (2009): the Band parameters of $\alpha = 0.07$, $\beta = -3.9$ and $E^{\rm obs}_{\rm peak} = 908$ keV, and the extra power-law photon index of -1.94. We simulate 10,000 spectra using the BAT energy response of 30° off-axis with the `xspec fakeit` command. We also created a simulated background spectrum using the real data and subtracted it from the simulated spectra. The systematic error has been applied to the spectrum using `batphasyserr`. The simulated spectra are fit by a PL and a CPL model. Figure 24 shows one example of the simulated spectrum fit by a PL model. Since the input spectrum has a steep power-law (photon index of -1.94) and then breaks to a very flat power-law (photon index of 0.07) around 50 keV, the BAT simulated spectrum shows a significant deviation from a PL fit. In this example, the reduced χ^2 in a PL fit is 2.93. None of a CPL fit to the simulated spectra shows a significant improvement over a PL fit. Figure 25 shows the reduced χ^2 distribution of the BAT simulated spectra inputting the spectral parameters of the *Fermi* GRB 090902B interval b fit by a PL model. The Gaussian fit to the histogram shows the peak of 2.58 with σ of 0.28. 99.97% of the simulated spectra show the reduced $\chi^2 \geq 1.7$. On the other hand, the reduced χ^2 distributions of the time-averaged and the time-resolved spectra of the actual BAT GRBs either by a PL or a CPL fit are well centroid around 1 (Figure 26). There are only two time-resolved spectra (out of 3284 spectra) which show the reduced $\chi^2 > 1.7$. By eye inspection, the residuals from the best fit model for these two spectra are not similar to the residuals seen in Figure 25. The worst reduced χ^2 of the time-averaged spectra of the BAT GRBs is 1.54. Therefore, we conclude that we can

not confirm the existence of the extra power-law component which extends below 50 keV like *Fermi* GRB 090902B in the BAT GRB spectra. Although GRB 090902B and also other *Fermi* GRBs which claim to have detections of the extra power-law component could be a special type of GRBs which have never been observed by the BAT, we believe that confirmations from other GRB instruments are required to validate the existence of the extra power-law component, especially whether this component is visible at the hard X-ray range in the spectrum.

4.7. Observed Properties vs. Redshifts

Figure 27 shows the observed BAT T_{90} duration versus the redshifts. We also plot the calculated T_{90} that we would observe if the GRBs, GRB 050525A (z=0.606), GRB 061126 (z=1.1588) and GRB 061222B (z=3.355) had occurred at a different redshift. If high-z bursts have the same duration in the rest frame as low-z bursts, then we would expect the duration of a high-redshift GRB tends to be longer as shown in those trajectories. However, there is no clear indication in the BAT observed T_{90} duration that the observed duration is longer for high-z bursts.

Figure 28 shows the observed photon index of the time-averaged spectra in a PL fit versus the redshifts. If there is an intrinsic spectral shape in the GRB rest frame, we would expect the observed spectra to be softer when the redshift is higher. The overlaid curves in the figure show the expected BAT observed PL photon index as a function of redshift for a model burst with $E^{\rm src}_{\rm peak}$ of 300 keV, 100 keV and 30 keV. We used the $E_{\rm peak}$-Γ relation (Sakamoto et al. 2009b) to convert $E^{\rm obs}_{\rm peak}$ into the BAT PL photon index for these curves. As can be seen in the figure, there is no clear trend that the BAT PL photon index goes softer as the redshift goes higher. The photon index of high redshift GRBs are the same as low redshift GRBs or are even harder in the BAT data. This suggests that there is no intrinsic spectral shape in the GRB rest frame for the *Swift* known-redshift samples. This also suggests that *Swift* has not been seeing soft high redshift bursts. Furthermore, the redshifts of the BAT GRBs which have soft spectra (photon index < -2) are less than 3.5. This might indicate that redshifts of GRBs with soft spectra (like X-ray flashes)(Heise et al. 2001; Kippen et al. 2001; Sakamoto et al. 2005) are not very high.

The distributions of the peak flux and the fluence as a function of redshift are shown in Figures 29 and 30. Although the peak flux and the fluence measured in the narrow BAT energy band are not bolometric measurements, there is no obvious correlation between those parameters and the redshifts. The fluence and the peak flux of the low redshift GRBs are scattered from the lowest to the highest values. The high redshift GRBs are located in the

small peak flux and the fluence region, but they are not the dimmest populations of the BAT known redshift GRBs.

4.8. Rest-frame Properties

Figure 31 shows the distribution of T_{90} and T_{50} durations measured in the 140-220 keV band in the GRB rest frame as a function of redshifts. The averaged T_{90} and T_{50} durations in the rest frame are 18.5 s and 8.0 s respectively. The correlation coefficients between T_{90} and T_{50} and the redshifts are 0.09 in 122 samples (the null probability of 0.3) and 0.1 in 121 samples (the null probability of 0.3) respectively. Therefore, there is no clear trend between the duration in the GRB rest fame and the redshifts.

Figure 32 shows the correlation between $E^{\rm src}_{\rm peak}$ and the isotropic-equivalent energy $E_{\rm iso}$. The $E^{\rm src}_{\rm peak}$ and $E_{\rm iso}$ values of the GRB samples from BASTE, *BeppoSAX* and *HETE*-2 are extracted from Amati (2006). We only select the *Swift* GRBs for which we reported the time-averaged CPL fits in this catalog and that also have redshift measurements. For those bursts, we fit the spectrum with a Band function to measured $E^{\rm src}_{\rm peak}$ and $E_{\rm iso}$. $E_{\rm iso}$ is calculated by integrating over the 1 keV - 10 MeV band in the GRB rest frame. We used the same cosmological parameters of Amati (2006) in the calculation of $E_{\rm iso}$ for the *Swift* GRBs. Table 13 summarized the values of $E^{\rm src}_{\rm peak}$ and $E_{\rm iso}$ of *Swift* GRBs. As shown in Figure 32, the *Swift* GRB samples are consistent with the samples from other GRB missions, and following the relation originally proposed by Amati et al. (2002).

5. Summary

The BAT2 catalog includes 476 GRBs detected by BAT during 5 years of operation. We presented the observed temporal and spectral properties of the BAT GRBs mainly based on BAT event data. In this catalog, not only the time-averaged but also the time-resolved spectral properties of the BAT GRBs are presented. We also distinguish among L-GRBs, S-GRBs, and S-GRBs with E.E. to investigate the possible distinct characteristics in the prompt emission properties. Comparisons in the prompt emission properties between the BATSE, the *BeppoSAX* and the *HETE*-2 GRB samples are shown. The observed prompt emission properties for the BAT known redshift GRBs are also presented.

We have shown that the BAT T_{90} and T_{50} durations peak around 70 s and 30 s, respectively, whereas the BATSE, the *BeppoSAX* and the *HETE*-2 T_{90} durations peak around 10-30 s which can be understood by the difference in the sensitivity of the instruments.

We have confirmed that the spectra of the BAT S-GRBs are generally harder than those of the L-GRBs. The overall hardness of the S-GRBs with E.E. is comparable to that of the L-GRBs, whereas, the hardness of the initial short spikes of the S-GRBs with E.E. is comparable to that of the S-GRBs. By comparing the BAT GRBs with the BATSE and the *HETE*-2 samples using the fluences in the 50-150 keV and the 15-50 keV bands, we have shown that the majority of the BAT GRBs are systematically softer than the bright BATSE GRBs. Whereas, the *HETE*-2 samples overlap with the BAT GRBs in this fluence-fluence plane. We have confirmed that photon indicies of PL fits to the BAT S-GRBs are harder than that of the L-GRBs in the time-averaged spectral analysis. The distribution of the time-averaged PL photon indicies of the S-GRBs with E.E. is consistent with that of the L-GRBs. However, the PL photon indicies of the initial short spikes of the S-GRBs with E.E. are much more similar to those of the S-GRBs. The time-averaged $E^{\rm obs}_{\rm peak}$ of the BAT GRBs based on a CPL fit shows a log-normal distribution in the peak around 80 keV which is significantly smaller than that of the BATSE GRBs which peak around 320 keV. There is no significant difference in the $E^{\rm obs}_{\rm peak}$ based on a CPL fit between the time-averaged and the time-resolved spectra in the BAT data. We have confirmed that 10% of the BAT photon indices in the BAT time-resolved spectra are outside the allowed range of the line of death (the limit from the SSM). The intervals which violate the line of death are at a bright peak and/or at a rising part of a peak. The BAT observed T_{90} of known high redshift GRBs are not systematically longer. The observed spectra of the BAT high redshift GRBs are similar to or harder than the moderate *Swift* redshift GRBs. The T_{90} and T_{50} durations measured at the 140-220 keV band at the GRB rest frame for the BAT known redshift samples are peaked at 19 s and 8 s, respectively. The BAT GRB samples are consistent with the $E^{\rm src}_{\rm peak}$-$E_{\rm iso}$ relation (Amati relation).

REFERENCES

Abdo, A.A. et al. 2009, ApJ, 706, L128

Amati, L. et al. 2002, A&A, 390, 81

Amati, L. 2006, MNRAS, 372, 233

Band, D.L., 1993, ApJ, 413, 281

Barthelmy, S. D., et al. 2005, Space Sci. Rev., 120, 143

Barthelmy, S. D., et al. 2005, Nature, 438, 994

Berger, E. 2009, ApJ, 690, 231

Burrows, S. D., et al. 2005a, Space Sci. Rev., 120, 165

Copete, A. et al. 2007, GCN Circ. 6653, http://gcn.gsfc.nasa.gov/gcn3/6653.gcn3

Evans, P.A., et al. 2009, MNRAS, 397, 1177

Fenimore, E. E., in't Zand, J.J.M., Norris, J.P., Bonnel, J.T., & Nemiroff, R.J. 1995, ApJ, 448, L101

Frontera, F., et al. 2009, ApJS, 180, 192

Gehrels, N. et al. 2004, ApJ, 611, 1005

Ghirlanda et al. 2009, A&A, 496, 585

Heise, J., in't Zand, J., Kippen, R.M., & Woods, P.M. 2001, in Gamma-Ray Bursts in the Afterglow Era, ed. E. Costa, F. Frontera, & J. Hjorth (Berlin:Springer), 16

Kaneko, Y. et al. 2006, ApJS, 166, 298

Kippen, R.M., Woods, P.M., Heise, J., in't Zant, J.J.M., Briggs, M.S., Preece, R.D. 2003, in API Conf. Proc. 662, Gamma-Ray Burst and Afterglow Astronomy 2001, ed. G.R.Ricker & R.K. Vanderspek (New York: AIP), 244

Kouveliotou, C., et al. 1993, ApJ, 413, L101

Lu, R.-J., Hou, S.-J., Liang, En-Wei 2010, ApJ in press

Norris, J.P., Marani, G.F., & Bonnelll, J.T. 2000, ApJ, 534, 248

Norris, J.P., Gehrels, N., Scargle, J.D. 2010, ApJ, in press (arXiv/0910.2456)

Paciesas, W.S. et al. 1999, ApJS, 122, 465

Palmer, D.M. et al. 2005, Nature, 434, 1107

Pélangeon, A. et al., A&A,

Preece, R.D. et al., 1998, ApJL, 506, 23

Perley, D.A., et al. 2009, ApJ, 138, 1690

Racusin, J.L. et al. 2008, Nature, 455, 183

Rees, M.J. & Mészáros, P., 1992, MNRAS, 258, 41

Roming, P.W.A. et al. 2005, Space Sci. Rev., 120, 95

Sakamoto, T. et al. 2005, ApJ, 629, 311

Sakamoto, T. et al. 2008, ApJS, 175, 179

Sakamoto, T. et al. 2009a, in AIP Conf. Proc. 1133, Gamma-Ray Bursts 6th Huntsville Symposium, ed. C. Meegan, M. Gehrels & C. Kouveliotou (New York: AIP), 503

Sakamoto, T. et al. 2009b, ApJ, 693, 922

Sakamoto, T. et al. 2010, Submitted to PASJ

Sari, R. et al. 1998, ApJL, 506, 23

Sato, G. et al. 2005, NIM A, 541, 372

Scargle, J. D. 1998, ApJ, 504, 405

Suzuki, M. et al. 2005, IEEE Trans. Nucl. Sci., 52, 1033

Tanvir, N.R., et al. 2009, Nature, 461, 1254

Salvaterra, R. et al. 2009, Nature, 461, 1258

Table 1. BAT GRB summary

GRB Name	Trigger Number	Trigger time	R.A. (°)	Dec. (°)	R.A.(XRT) (°)	Dec.(XRT) (°)	SN_{img} (σ)	Error (′)	T_{90} (s)	T_{50} (s)	Start (s)	Stop (s)	Note
041217	100116	2004-12-17 07:28:25.920	164.790	-17.944	—	—	19.3	1.4	5.65	2.71	-2	18	
041219A	100318	2004-12-19 01:42:18.000	6.154	62.847	—	—	—	—	—	—	—	—	(1)
041219B	100367	2004-12-19 15:38:48.000	167.674	-33.458	—	—	—	—	—	—	—	—	(1)
041219C	100380	2004-12-19 20:30:34.000	343.882	-76.786	—	—	13.2	1.8	10.00	4.00	-3	17	
041220	100433	2004-12-20 22:58:26.599	291.301	60.596	—	—	31.9	1.0	5.58	2.20	-300	302	
041223	100585	2004-12-23 14:06:17.956	100.186	-37.072	—	—	83.7	1.0	109.08	29.20	-299	303	
041224	100703	2004-12-24 20:20:57.698	56.192	-6.666	—	—	11.4	2.0	177.17	37.68	-299	303	
041226	100815	2004-12-26 20:34:18.976	79.647	73.343	—	—	5.6	3.3	89.50	52.72	-299	303	(11)
041228	100970	2004-12-28 10:49:14.142	336.649	5.027	—	—	36.5	1.0	52.16	19.54	-299	303	
050117	102861	2005-01-17 12:52:36.037	358.490	65.934	—	—	53.8	1.0	166.65	83.51	-299	303	
050124	103647	2005-01-24 11:30:02.876	192.876	13.041	192.8773	13.0443	35.0	1.0	3.93	1.88	-299	303	
050126	103780	2005-01-26 12:00:54.073	278.134	42.395	—	—	15.2	1.6	48.00	16.00	-299	303	
050128	103906	2005-01-28 04:19:55.191	219.584	-34.762	219.5737	-34.7654	26.3	1.1	28.00	8.00	-300	303	
050202	104298	2005-02-02 03:35:14.800	290.583	-38.733	—	—	9.7	2.2	0.11	0.05	-299	243	(2)
050215A	106106	2005-02-15 02:15:28.543	348.411	49.322	—	—	7.8	2.6	66.41	49.00	-120	302	
050215B	106107	2005-02-15 02:33:43.199	174.467	40.792	174.4473	40.7974	15.4	1.6	10.62	4.74	-240	229	
050219A	106415	2005-02-19 12:40:01.049	166.413	-40.685	166.4125	-40.6841	34.5	1.0	23.84	10.06	-299	303	
050219B	106442	2005-02-19 21:05:51.256	81.300	-57.759	81.3170	-57.7581	29.7	1.0	28.74	6.91	-300	302	
050223	106709	2005-02-23 03:09:06.068	271.391	-62.468	271.3850	-62.4727	16.7	1.5	21.68	10.58	-299	303	
050306	107547	2005-03-06 03:33:11.876	282.313	-9.151	282.3098	-9.1532	30.5	1.0	158.43	73.72	-299	303	
050315	111063	2005-03-15 20:59:42.518	306.480	-42.589	306.4758	-42.6004	25.4	1.1	95.57	24.36	-300	302	
050318	111529	2005-03-18 15:44:37.170	49.697	-46.388	49.7127	-46.3960	30.9	1.0	40.0	20.8	-300	32	(3)
050319	111622	2005-03-19 09:31:18.449	154.172	43.580	154.1996	43.5486	8.2	2.5	151.74	124.57	-300	302	
050326	112453	2005-03-26 09:53:56.135	6.881	-71.374	—	—	72.3	1.0	29.44	19.39	-300	303	
050401	113120	2005-04-01 14:20:15.326	247.872	2.186	—	—	28.6	1.0	33.30	25.92	-300	302	
050406	113872	2005-04-06 15:58:48.407	34.417	-50.181	34.4671	-50.1879	8.3	2.5	4.79	1.64	-300	302	
050410	114299	2005-04-10 12:14:33.553	89.757	79.606	89.8061	79.6033	23.5	1.2	64.00	32.00	-299	243	
050412	114485	2005-04-12 05:44:02.894	181.099	-1.187	—	—	16.7	1.5	26.46	9.50	-299	303	

[1]The event data are not available.

[2]Short duration GRB.

[3]The event data of the part of the burst emission are not available.

Table 2. BAT GRB energy fluence

GRB Name	Spectral Model	S(15-25)	S(25-50)	S(50-100)	S(100-150)	S(15-150)	Start (s)	Stop (s)	Note
				(10^{-8} ergs cm^{-2})					
041217	CPL	30.0 ± 3.1	72.1 ± 3.3	106.0 ± 5.3	61.1 ± 8.1	270.0 ± 12.1	+0.82	+7.89	
041219A	—	—	—	—	—	—	—	—	(1)
041219B	—	—	—	—	—	—	—	—	(1)
041219C	PL	25.5 ± 2.0	34.5 ± 1.6	34.4 ± 2.5	20.0 ± 2.3	114.0 ± 5.8	+0.00	+12.00	
041220	PL	5.9 ± 0.6	9.8 ± 0.7	12.3 ± 1.2	8.6 ± 1.3	36.6 ± 2.8	-0.21	+6.81	
041223	PL	153.0 ± 5.8	347.0 ± 7.7	624.0 ± 10.4	576.0 ± 15.3	1700.0 ± 27.2	-10.54	+145.94	
041224	CPL	133.0 ± 11.0	261.0 ± 10.4	309.0 ± 14.2	149.0 ± 21.1	853.0 ± 34.3	-109.63	+116.27	
041226	PL	3.8 ± 1.5	7.4 ± 1.8	11.0 ± 3.4	8.9 ± 4.3	31.0 ± 8.2	-1.34	+93.50	
041228	PL	52.8 ± 4.2	90.2 ± 4.2	118.0 ± 6.1	84.7 ± 7.1	345.0 ± 14.8	-0.40	+66.78	
050117	CPL	112.0 ± 7.1	226.0 ± 5.9	318.0 ± 9.2	211.0 ± 15.6	867.0 ± 23.0	+4.28	+215.86	
050124	CPL	12.7 ± 1.7	30.3 ± 2.0	46.3 ± 3.1	28.5 ± 4.5	118.0 ± 6.9	-3.90	+3.07	
050126	PL	10.1 ± 1.8	20.3 ± 2.2	31.6 ± 4.0	26.1 ± 5.0	88.0 ± 10.0	-11.44	+36.56	
050128	CPL	51.2 ± 6.3	125.0 ± 6.8	201.0 ± 11.3	133.0 ± 15.2	511.0 ± 23.7	-7.56	+25.44	
050202	PL	0.4 ± 0.1	0.7 ± 0.1	1.1 ± 0.2	0.9 ± 0.3	3.2 ± 0.6	+0.00	+0.14	
050215A	PL	7.1 ± 1.9	14.4 ± 2.2	23.0 ± 4.0	19.4 ± 5.5	63.9 ± 9.9	-0.32	+71.07	
050215B	PL	6.1 ± 0.9	7.4 ± 0.8	6.6 ± 1.4	3.5 ± 1.1	23.5 ± 3.2	-1.98	+10.86	
050219A	CPL	33.9 ± 3.7	102.0 ± 4.5	173.0 ± 7.5	98.4 ± 10.6	408.0 ± 15.9	-5.81	+29.98	
050219B	CPL	186.0 ± 16.8	413.0 ± 15.5	604.0 ± 23.7	381.0 ± 29.3	1580.0 ± 49.5	-35.59	+38.57	
050223	PL	12.2 ± 1.6	18.4 ± 1.6	20.7 ± 2.8	13.3 ± 2.8	64.6 ± 6.6	-12.01	+16.57	
050306	CPL	135.0 ± 14.6	287.0 ± 13.6	426.0 ± 21.1	294.0 ± 27.5	1140.0 ± 33.9	-3.42	+187.84	
050315	PL	75.9 ± 5.4	97.8 ± 4.2	92.0 ± 6.2	51.3 ± 5.5	317.0 ± 14.3	-56.24	+69.18	
050318	—	—	—	—	—	—	—	—	(2)
050319	PL	27.8 ± 3.7	39.3 ± 3.6	41.1 ± 6.5	24.9 ± 6.0	133.0 ± 14.9	-134.09	+27.76	
050326	PL	90.4 ± 3.5	192.0 ± 4.3	321.0 ± 5.9	280.0 ± 8.5	884.0 ± 15.2	-9.84	+32.42	
050401	PL	94.8 ± 7.3	191.0 ± 8.7	298.0 ± 11.9	247.0 ± 15.4	831.0 ± 30.8	-7.68	+29.06	
050406	CPL	2.2 ± 0.5	3.4 ± 0.8	1.1 ± 0.8	0.35	6.7 ± 1.4	-2.50	+3.90	(3)
050410	CPL	59.6 ± 6.9	128.0 ± 7.3	164.0 ± 10.8	82.9 ± 15.6	435.0 ± 24.9	-27.02	+36.98	
050412	PL	3.3 ± 0.7	9.6 ± 1.2	23.2 ± 2.0	26.8 ± 3.7	62.9 ± 5.7	-8.28	+22.16	
050416A	CPL	19.7 ± 2.5	13.3 ± 2.2	5.9 ± 2.0	1.8 ± 0.9	40.7 ± 5.6	+0.03	+10.14	
050416B	CPL	10.3 ± 2.3	27.9 ± 2.7	45.6 ± 4.6	27.2 ± 6.8	111.0 ± 10.1	+0.06	+4.20	
050418	CPL	77.9 ± 6.4	143.0 ± 5.7	181.0 ± 8.2	109.0 ± 12.8	511.0 ± 19.9	-8.35	+80.50	
050421	PL	2.1 ± 0.8	3.7 ± 0.9	4.9 ± 1.7	3.6 ± 1.9	14.3 ± 4.0	+0.05	+18.11	
050422	PL	7.2 ± 1.5	14.1 ± 1.8	21.2 ± 3.3	17.1 ± 4.1	59.6 ± 8.1	-11.30	+68.70	
050502B	PL	7.0 ± 0.8	12.1 ± 0.9	16.2 ± 1.8	11.8 ± 2.0	47.1 ± 4.2	-17.32	+3.18	
050505	PL	30.0 ± 4.0	58.8 ± 4.8	89.3 ± 7.1	72.5 ± 8.9	251.0 ± 18.1	-10.06	+52.51	
050507	—	—	—	—	—	—	—	—	(2)
050509A	PL	8.3 ± 1.0	10.4 ± 0.8	9.7 ± 1.5	5.3 ± 1.3	33.6 ± 3.3	-6.26	+8.06	
050509B	PL	0.08 ± 0.03	0.16 ± 0.04	0.26 ± 0.08	0.2 ± 0.1	0.7 ± 0.2	+0.00	+0.03	
050525A	CPL	220.0 ± 9.8	440.0 ± 7.6	555.0 ± 8.8	299.0 ± 8.1	1510.0 ± 20.0	-0.12	+12.68	
050528	PL	12.1 ± 2.2	14.3 ± 2.0	12.1 ± 3.0	6.2 ± 2.3	44.7 ± 7.0	-8.20	+4.98	
050603	PL	66.3 ± 5.4	147.0 ± 7.1	257.0 ± 11.2	233.0 ± 16.1	703.0 ± 28.9	-17.77	+33.23	
050607	PL	12.5 ± 1.8	17.9 ± 1.7	19.0 ± 3.0	11.7 ± 2.8	61.2 ± 6.82	-11.37	+36.63	

[1]The event data are not available.

[2]The event data of the part of the burst emission are not available.

[3]S(100-150) is an upper limit.

Table 3. BAT GRB 1-s peak photon flux

GRB Name	Spectral Model	F^p_{ph}(15-25)	F^p_{ph}(25-50)	F^p_{ph}(50-100)	F^p_{ph}(100-150)	F^p_{ph}(15-150)	Start (s)	Note
				(photons cm^{-2} s^{-1})				
041217	PL	2.09 ± 0.25	2.24 ± 0.17	1.70 ± 0.14	0.796 ± 0.106	6.82 ± 0.48	+3.26	
041219A	—	—	—	—	—	—	—	(1)
041219B	—	—	—	—	—	—	—	(1)
041219C	PL	0.88 ± 0.14	0.78 ± 0.04	0.48 ± 0.03	0.19 ± 0.02	2.33 ± 0.23	+2.00	
041220	PL	0.52 ± 0.03	0.58 ± 0.02	0.46 ± 0.02	0.22 ± 0.02	1.78 ± 0.13	-0.02	
041223	PL	1.51 ± 0.11	2.20 ± 0.10	2.38 ± 0.10	1.48 ± 0.05	7.58 ± 0.29	+35.01	
041224	PL	0.82 ± 0.14	0.95 ± 0.10	0.79 ± 0.04	0.40 ± 0.03	2.95 ± 0.29	-0.06	
041226	PL	0.09 ± 0.02	0.11 ± 0.02	0.09 ± 0.02	0.05 ± 0.01	0.34 ± 0.05	+3.31	
041228	PL	0.63 ± 0.15	0.56 ± 0.04	0.34 ± 0.03	0.13 ± 0.02	1.65 ± 0.24	+22.03	
050117	PL	0.51 ± 0.03	0.70 ± 0.03	0.70 ± 0.03	0.41 ± 0.03	2.32 ± 0.16	+87.22	
050124	CPL	4.20 ± 0.63	11.9 ± 0.9	19.5 ± 1.5	11.1 ± 2.2	46.6 ± 3.3	-0.1	
050126	PL	0.64	0.91	1.56	2.21	4.22	+12.1	(3,4,5,6,7)
050128	PL	6.73 ± 1.02	13.9 ± 1.3	22.2 ± 2.2	18.7 ± 2.8	61.6 ± 5.66	+5.4	
050202	PL	0.58 ± 0.31	1.09 ± 0.34	1.57 ± 0.55	1.22 ± 0.69	4.46 ± 1.31	-0.4	
050215A	PL	0.27 ± 0.16	0.78 ± 0.28	1.86 ± 0.46	2.11 ± 0.80	5.02 ± 1.27	+5.6	
050215B	PL	0.78 ± 0.20	1.24 ± 0.23	1.47 ± 0.42	0.98 ± 0.42	4.47 ± 1.00	+0.1	
050219A	PL	2.78 ± 0.47	6.38 ± 0.67	11.6 ± 1.2	10.7 ± 1.7	31.4 ± 3.1	+9.5	
050219B	CPL	23.0 ± 2.6	50.7 ± 3.1	69.6 ± 4.9	40.2 ± 5.9	184.0 ± 10.0	+2.8	
050223	PL	0.65 ± 0.26	1.22 ± 0.30	1.76 ± 0.55	1.37 ± 0.67	5.00 ± 1.32	+1.6	
050306	PL	2.88 ± 0.71	6.39 ± 0.96	11.1 ± 1.5	10.0 ± 2.0	30.4 ± 3.9	+107.9	
050315	PL	2.67 ± 0.38	3.47 ± 0.36	3.30 ± 0.57	1.85 ± 0.48	11.3 ± 1.4	+24.6	
050318	—	—	—	—	—	—	—	(2)
050319	PL	1.99 ± 0.35	2.69 ± 0.36	2.68 ± 0.60	1.56 ± 0.52	8.92 ± 1.43	+0.6	
050326	PL	8.13 ± 0.40	21.0 ± 0.6	43.6 ± 1.4	44.8 ± 2.1	117.0 ± 3.6	-0.1	
050401	CPL	6.88 ± 1.53	21.2 ± 2.1	41.7 ± 4.1	29.6 ± 5.3	99.2 ± 7.9	+24.3	
050406	PL	0.53 ± 0.18	0.65 ± 0.20	0.57 ± 0.32	0.30 ± 0.25	2.04 ± 0.75	+0.5	
050410	PL	1.91 ± 0.62	2.98 ± 0.68	3.51 ± 1.12	2.33 ± 1.10	10.7 ± 2.7	-3.5	
050412	PL	0.23 ± 0.11	0.74 ± 0.22	1.98 ± 0.38	2.47 ± 0.72	5.42 ± 1.07	+1.1	
050416A	CPL	8.64 ± 0.92	9.44 ± 1.13	1.75 ± 0.94	—	19.9 ± 1.9	+0.0	(6)
050416B	PL	4.27 ± 0.82	10.6 ± 1.3	21.2 ± 2.1	21.2 ± 3.1	57.3 ± 5.4	+0.1	
050418	PL	2.79 ± 0.38	6.57 ± 0.55	12.3 ± 1.0	11.7 ± 1.4	33.4 ± 2.5	+0.7	
050421	PL	0.48 ± 0.19	0.82 ± 0.21	1.05 ± 0.41	0.75 ± 0.45	3.10 ± 0.97	+0.4	
050422	PL	0.36 ± 0.19	0.51 ± 0.20	0.55 ± 0.38	$0.80 \pm - - -$	1.76 ± 0.87	+60.2	(6)
050502B	CPL	1.12 ± 0.20	3.10 ± 0.32	4.47 ± 0.52	2.01 ± 0.81	10.7 ± 1.2	+0.2	
050505	PL	1.39 ± 0.43	3.29 ± 0.64	6.17 ± 0.95	5.89 ± 1.32	16.7 ± 2.5	+1.0	
050507	—	—	—	—	—	—	—	(2)

[1]The event data are not available.

[2]The event data of the part of the burst emission are not available.

[3]F^p_{ph}(15-25) is an upper limit.

[4]F^p_{ph}(25-50) is an upper limit.

[5]F^p_{ph}(50-100) is an upper limit.

[6]F^p_{ph}(100-150) is an upper limit.

[7]F^p_{ph}(15-150) is an upper limit.

Table 4. BAT GRB 1-s peak energy flux

GRB Name	Spectral Model	F^p_{ene}(15-25)	F^p_{ene}(25-50)	F^p_{ene}(50-100)	F^p_{ene}(100-150)	F^p_{ene}(15-150)	Note
		(10^{-8} ergs cm^{-2} s^{-1})					
041217	PL	6.5 ± 0.8	12.7 ± 0.9	19.3 ± 1.7	15.7 ± 2.1	54.2 ± 4.2	
041219A	—	—	—	—	—	—	(1)
041219B	—	—	—	—	—	—	(1)
041219C	PL	2.7 ± 0.4	4.4 ± 0.4	5.4 ± 0.7	3.7 ± 0.8	16.3 ± 1.8	
041220	PL	1.6 ± 0.2	3.3 ± 0.3	5.2 ± 0.5	4.4 ± 0.7	14.5 ± 1.3	
041223	PL	4.8 ± 0.4	12.8 ± 0.6	27.7 ± 1.2	29.4 ± 1.9	74.6 ± 3.2	
041224	PL	2.5 ± 0.4	5.4 ± 0.6	9.0 ± 1.0	7.9 ± 1.3	24.9 ± 2.6	
041226	PL	0.3 ± 0.1	0.6 ± 0.2	1.1 ± 0.4	1.0 ± 0.5	2.9 ± 0.9	
041228	PL	2.0 ± 0.5	3.1 ± 0.5	3.8 ± 0.8	2.6 ± 0.8	11.4 ± 1.8	
050117	PL	1.6 ± 0.2	4.0 ± 0.3	8.1 ± 0.6	8.2 ± 1.0	21.9 ± 1.7	
050124	CPL	4.2 ± 0.6	11.9 ± 0.9	19.5 ± 1.5	11.1 ± 2.2	46.6 ± 3.3	
050126	PL	0.6	0.9	1.6	2.2	4.2	(3,4,5,6,7)
050128	PL	6.7 ± 1.0	13.9 ± 1.3	22.2 ± 2.2	18.7 ± 2.8	61.6 ± 5.7	
050202	PL	0.6 ± 0.3	1.1 ± 0.3	1.6 ± 0.6	1.2 ± 0.7	4.5 ± 1.3	
050215A	PL	0.3 ± 0.2	0.8 ± 0.3	1.9 ± 0.5	2.1 ± 0.8	5.0 ± 1.3	
050215B	PL	0.8 ± 0.2	1.2 ± 0.2	1.5 ± 0.4	1.0 ± 0.4	4.5 ± 1.0	
050219A	PL	2.8 ± 0.5	6.4 ± 0.7	11.6 ± 1.2	10.7 ± 1.7	31.4 ± 3.1	
050219B	CPL	23.0 ± 2.6	50.7 ± 3.1	69.6 ± 4.9	40.2 ± 5.9	184.0 ± 10.0	
050223	PL	0.7 ± 0.3	1.2 ± 0.3	1.8 ± 0.6	1.4 ± 0.7	5.0 ± 1.3	
050306	PL	2.9 ± 0.7	6.4 ± 1.0	11.1 ± 1.5	10.0 ± 2.0	30.4 ± 3.9	
050315	PL	2.7 ± 0.4	3.5 ± 0.4	3.3 ± 0.6	1.9 ± 0.5	11.3 ± 1.4	
050318	—	—	—	—	—	—	(2)
050319	PL	2.0 ± 0.4	2.7 ± 0.4	2.7 ± 0.6	1.6 ± 0.5	8.9 ± 1.4	
050326	PL	8.1 ± 0.4	21.0 ± 0.6	43.6 ± 1.4	44.8 ± 2.1	117.0 ± 3.6	
050401	CPL	6.9 ± 1.5	21.2 ± 2.1	41.7 ± 4.1	29.6 ± 5.3	99.2 ± 7.9	
050406	PL	0.5 ± 0.2	0.7 ± 0.2	0.6 ± 0.3	0.3 ± 0.3	2.0 ± 0.8	
050410	PL	1.9 ± 0.6	3.0 ± 0.7	3.5 ± 1.1	2.3 ± 1.1	10.7 ± 2.7	
050412	PL	0.2 ± 0.1	0.7 ± 0.2	2.0 ± 0.4	2.5 ± 0.7	5.4 ± 1.1	
050416A	CPL	8.6 ± 0.9	9.4 ± 1.1	1.8 ± 0.9	0.1	19.9 ± 1.9	(6)
050416B	PL	4.3 ± 0.8	10.6 ± 1.3	21.2 ± 2.1	21.2 ± 3.1	57.3 ± 5.4	
050418	PL	2.9 ± 0.4	6.6 ± 0.6	12.3 ± 1.0	11.7 ± 1.4	33.4 ± 2.5	
050421	PL	0.5 ± 0.2	0.8 ± 0.2	1.1 ± 0.4	0.8 ± 0.5	3.1 ± 1.0	
050422	PL	0.4 ± 0.2	0.5 ± 0.2	0.6 ± 0.4	0.8	1.8 ± 0.9	
050502B	CPL	1.1 ± 0.2	3.1 ± 0.3	4.5 ± 0.5	2.0 ± 0.8	10.7 ± 1.2	
050505	PL	1.4 ± 0.4	3.3 ± 0.6	6.2 ± 1.0	5.9 ± 1.3	16.7 ± 2.5	
050507	—	—	—	—	—	—	(2)

[1]The event data are not available.

[2]The event data of the part of the burst emission are not available.

[3]F^p_{ene}(15-25) is an upper limit.

[4]F^p_{ene}(25-50) is an upper limit.

[5]F^p_{ene}(50-100) is an upper limit.

[6]F^p_{ene}(100-150) is an upper limit.

[7]F^p_{ene}(15-150) is an upper limit.

Table 5. BAT GRB 20-msec peak photon and energy flux

GRB Name	Spectral Model	F^{p}_{ene}(15-150) (10^{-8} ergs cm^{-2} s^{-1})	F^{p}_{ph}(15-150) (photons cm^{-2} s^{-1})	Start (s)	Note
041217	CPL	75.5 ± 31.0	9.5 ± 3.3	+3.63	
041219A	—	—	—	—	(1)
041219B	—	—	—	—	(1)
041219C	PL	20.8 ± 10.8	4.1 ± 1.6	+8.13	
041220	PL	33.0 ± 11.8	3.1 ± 1.0	+0.25	
041223	PL	124.0 ± 27.1	11.3 ± 2.2	+24.30	
041224	CPL	44.6 ± 18.5	5.9 ± 2.1	+0.68	
041226	PL	13.1 ± 7.1	1.4 ± 0.7	+2.75	
041228	—	—	—	+2.49	(2)
050117	CPL	41.9 ± 16.6	4.0 ± 1.2	+88.02	
050124	CPL	69.1 ± 20.4	9.6 ± 2.6	+0.36	
050126	PL	28.5 ± 13.2	2.9 ± 1.2	+3.44	
050128	PL	154.0 ± 54.7	14.7 ± 4.5	+6.18	
050202	PL	41.9 ± 15.3	4.3 ± 1.4	+0.08	
050215A	PL	16.7 ± 10.3	1.9 ± 1.0	+0.40	
050215B	PL	17.0 ± 10.8	1.6 ± 0.9	+1.52	
050219A	PL	71.5 ± 31.1	6.9 ± 2.5	+10.52	
050219B	PL	344.0 ± 103.0	36.4 ± 9.6	+3.06	
050223	CPL	13.7 ± 7.5	2.4 ± 1.0	+7.74	
050306	CPL	70.3 ± 35.6	7.5 ± 3.7	+107.96	
050315	PL	22.7 ± 11.2	3.2 ± 1.4	+9.86	
050318	—	—	—	—	(3)
050319	CPL	18.7 ± 7.3	3.6 ± 1.3	+0.65	
050326	PL	161.0 ± 30.1	16.0 ± 2.4	+0.48	
050401	—	—	—	+25.17	(2)
050406	PL	11.3	1.3 ± 0.6	+0.60	(4)
050410	CPL	81.0	5.0 ± 2.6	+7.84	(4)
050412	PL	12.6 ± 6.7	1.5 ± 0.6	+21.66	
050416A	CPL	25.0 ± 12.1	7.4 ± 3.3	+0.72	
050416B	PL	62.0 ± 32.8	8.6 ± 4.2	+0.20	
050418	CPL	46.1 ± 20.3	5.7 ± 2.0	+2.35	
050421	PL	15.4 ± 9.1	1.4 ± 0.8	+1.33	
050422	PL	12.9 ± 7.5	1.6 ± 0.7	+2.52	
050502B	PL	22.2 ± 9.0	2.4 ± 0.9	+0.89	
050505	PL	33.8 ± 18.3	4.7 ± 2.2	-8.37	
050507	—	—	—	—	(3)
050509A	PL	11.4 ± 6.0	1.7 ± 0.7	-4.93	
050509B	PL	31.4 ± 10.3	3.7 ± 1.0	+0.01	
050525A	CPL	494.0 ± 47.4	53.8 ± 3.9	+1.02	
050528	CPL	28.8 ± 15.2	3.6 ± 2.0	-5.01	

[1]The event data are not available.

[2]Reduced χ^2 is greater than 2.

[3]The event data of the part of the burst emission are not available.

[4]F^{p}_{ene}(15-150) is an upper limit.

Table 6. BAT time-averaged spectral parameters

GRB	$\alpha^{\rm PL}$	$K_{50}^{\rm PL}$(a)	χ^2	$\alpha^{\rm CPL}$	$E_{\rm peak}^{\rm obs}$ (keV)	$K_{50}^{\rm CPL}$(b)	χ^2	Note
041217	$-1.452^{+0.064}_{-0.064}$	$417.0^{+15.4}_{-15.4}$	73.2	$-0.663^{+0.309}_{-0.29}$	$91.5^{+22.8}_{-12.0}$	$97.5^{+37.3}_{-25.7}$	49.2	
041219A	—	—	—	—	—	—	—	(1)
041219B	—	—	—	—	—	—	—	(1)
041219C	$-2.007^{+0.087}_{-0.089}$	$103.0^{+5.4}_{-5.4}$	44.6	—	—	—	—	
041220	$-1.672^{+0.120}_{-0.122}$	$56.2^{+3.9}_{-4.0}$	30.5	—	—	—	—	
041223	$-1.153^{+0.030}_{-0.03}$	$106.0^{+1.8}_{-1.8}$	33.4	—	—	—	—	
041224	$-1.731^{+0.058}_{-0.058}$	$43.2^{+1.4}_{-1.4}$	62.8	$-0.984^{+0.281}_{-0.264}$	$68.9^{+11.7}_{-7.0}$	$10.1^{+3.7}_{-2.6}$	36.9	
041226	$-1.416^{+0.430}_{-0.417}$	$3.4^{+0.8}_{-0.8}$	85.1	—	—	—	—	
041228	$-1.617^{+0.077}_{-0.077}$	$55.1^{+2.3}_{-2.3}$	64.6	—	—	—	—	
050117	$-1.519^{+0.042}_{-0.042}$	$44.5^{+0.9}_{-0.9}$	44.4	$-1.171^{+0.182}_{-0.172}$	$130.3^{+70.6}_{-26.7}$	$6.4^{+1.3}_{-1.0}$	32.2	
050124	$-1.412^{+0.085}_{-0.085}$	$181.0^{+9.2}_{-9.2}$	55.2	$-0.698^{+0.404}_{-0.37}$	$100.2^{+48.4}_{-18.3}$	$38.8^{+20.3}_{-12.5}$	43.6	
050126	$-1.360^{+0.169}_{-0.168}$	$18.8^{+1.9}_{-1.9}$	72.3	—	—	—	—	
050128	$-1.368^{+0.071}_{-0.071}$	$162.0^{+6.9}_{-6.9}$	63.1	$-0.716^{+0.333}_{-0.313}$	$113.7^{+50.8}_{-20.2}$	$31.6^{+12.3}_{-8.5}$	49.5	
050202	$-1.357^{+0.296}_{-0.292}$	$246.0^{+42.8}_{-42.8}$	44.7	—	—	—	—	
050215A	$-1.326^{+0.267}_{-0.261}$	$9.1^{+1.2}_{-1.2}$	43.0	—	—	—	—	
050215B	$-2.173^{+0.209}_{-0.223}$	$19.6^{+3.0}_{-3.1}$	57.6	—	—	—	—	
050219A	$-1.305^{+0.056}_{-0.056}$	$121.0^{+4.1}_{-4.1}$	100.7	$-0.122^{+0.300}_{-0.282}$	$90.6^{+11.3}_{-7.9}$	$40.4^{+13.8}_{-9.8}$	39.0	
050219B	$-1.508^{+0.050}_{-0.05}$	$230.0^{+6.8}_{-6.8}$	79.4	$-0.919^{+0.236}_{-0.224}$	$107.9^{+30.2}_{-15.2}$	$41.4^{+10.6}_{-8.1}$	57.9	
050223	$-1.826^{+0.158}_{-0.163}$	$24.6^{+2.4}_{-2.5}$	49.3	—	—	—	—	
050306	$-1.467^{+0.065}_{-0.065}$	$63.4^{+2.4}_{-2.4}$	59.5	$-1.086^{+0.281}_{-0.265}$	$140.3^{+171.5}_{-35.8}$	$9.3^{+2.9}_{-2.1}$	53.3	
050315	$-2.087^{+0.084}_{-0.085}$	$27.2^{+1.3}_{-1.3}$	52.3	—	—	—	—	
050318	—	—	—	—	—	—	—	(2)
050319	$-1.934^{+0.171}_{-0.178}$	$8.9^{+1.0}_{-1.0}$	43.4	—	—	—	—	
050326	$-1.261^{+0.033}_{-0.032}$	$210.0^{+3.6}_{-3.6}$	46.9	—	—	—	—	
050401	$-1.358^{+0.064}_{-0.064}$	$232.0^{+8.6}_{-8.6}$	41.4	—	—	—	—	
050406	$-2.404^{+0.317}_{-0.365}$	$12.4^{+3.5}_{-3.5}$	73.6	$0.406^{+2.594}_{-1.754}$	$29.4^{+6.2}_{-3.2}$	$82.7^{+2170.0}_{-76.5}$	65.6	
050410	$-1.616^{+0.080}_{-0.08}$	$76.3^{+3.7}_{-3.7}$	66.4	$-0.812^{+0.386}_{-0.355}$	$75.6^{+21.0}_{-10.2}$	$19.0^{+10.1}_{-6.2}$	49.9	
050412	$-0.729^{+0.173}_{-0.165}$	$17.1^{+1.6}_{-1.6}$	30.3	—	—	—	—	
050416A	$-3.180^{+0.285}_{-0.319}$	$30.6^{+8.1}_{-7.7}$	58.6	$-0.972^{+2.279}_{-1.012}$	$13.7^{+7.9}_{-12.6}$	4870	52.2	(6)
050416B	$-1.327^{+0.128}_{-0.128}$	$285.0^{+21.7}_{-21.7}$	72.4	$-0.391^{+0.679}_{-0.585}$	$95.7^{+65.5}_{-19.4}$	$76.2^{+75.1}_{-34.4}$	64.3	
050418	$-1.665^{+0.060}_{-0.06}$	$63.4^{+2.1}_{-2.1}$	57.1	$-1.292^{+0.260}_{-0.246}$	$99.8^{+86.7}_{-21.2}$	$9.6^{+3.1}_{-2.2}$	50.2	
050421	$-1.593^{+0.412}_{-0.429}$	$8.5^{+2.1}_{-2.2}$	47.9	—	—	—	—	
050422	$-1.408^{+0.204}_{-0.205}$	$7.7^{+0.9}_{-0.9}$	41.5	—	—	—	—	
050502B	$-1.587^{+0.133}_{-0.135}$	$24.5^{+2.0}_{-2.0}$	67.9	—	—	—	—	
050505	$-1.396^{+0.118}_{-0.117}$	$41.4^{+2.9}_{-2.9}$	43.8	—	—	—	—	
050507	—	—	—	—	—	—	—	
050509A	$-2.114^{+0.165}_{-0.174}$	$25.2^{+2.7}_{-2.8}$	54.5	—	—	—	—	

[a]In the unit of 10^{-4} ph cm^{-2} s^{-1} keV^{-1}.

[b]In the unit of 10^{-3} ph cm^{-2} s^{-1} keV^{-1}.

[1]The event data are not available.

[2]The event data of the part of the burst emission are not available.

[6]$K_{50}^{\rm CPL}$ is an upper limit.

Table 7. BAT time-resolved spectral parameters

GRB	Start (s)	Stop (s)	$\alpha^{\rm PL}$	$K_{50}^{\rm PL}$(a)	χ^2	F_{PL}(15-150)(b)	$\alpha^{\rm CPL}$	$E_{\rm peak}^{\rm obs}$ (keV)	$K_{50}^{\rm CPL}$(c)	χ^2	F_{CPL}(15-150)(b)	Note
041217	0.824	5.812	$-1.385^{+0.064}_{-0.064}$	$499.0^{+18.8}_{-18.8}$	78.2	48.4 ± 1.9	$-0.517^{+0.319}_{-0.297}$	$93.6^{+21.1}_{-11.8}$	$126.0^{+49.2}_{-33.3}$	50.2	46.3 ± 2.1	
041217	5.812	7.888	$-1.763^{+0.191}_{-0.198}$	$210.0^{+25.5}_{-25.9}$	54.5	19.3 ± 2.5	—	—	—	—	—	
041219C	0.000	6.000	$-1.912^{+0.094}_{-0.096}$	$139.0^{+7.8}_{-7.8}$	52.7	12.7 ± 0.7	—	—	—	—	—	
041219C	6.000	9.000	$-2.168^{+0.169}_{-0.179}$	$88.8^{+10.4}_{-10.7}$	54.4	8.3 ± 0.9	—	—	—	—	—	
041219C	9.000	12.000	$-2.060^{+0.300}_{-0.332}$	$45.1^{+9.5}_{-9.9}$	42.3	4.2 ± 0.8	—	—	—	—	—	
041220	-0.208	1.728	$-1.479^{+0.116}_{-0.117}$	$126.0^{+8.3}_{-8.3}$	52.0	12.0 ± 0.9	—	—	—	—	—	
041220	1.728	2.936	$-1.862^{+0.236}_{-0.25}$	$59.1^{+9.4}_{-9.7}$	53.9	5.4 ± 0.9	—	—	—	—	—	
041220	2.936	6.812	$-2.029^{+0.360}_{-0.408}$	$19.3^{+5.0}_{-5.3}$	40.1	1.8 ± 0.4	—	—	—	—	—	
041223	-10.536	-0.544	$-1.363^{+0.388}_{-0.381}$	$17.1^{+4.0}_{-4.0}$	61.5	1.7 ± 0.4	—	—	—	—	—	
041223	-0.544	-0.124	$-1.529^{+0.400}_{-0.408}$	$88.9^{+21.9}_{-22.3}$	48.5	8.4 ± 2.3	—	—	—	—	—	
041223	-0.124	2.196	$-0.771^{+0.082}_{-0.081}$	$292.0^{+13.6}_{-13.7}$	57.6	34.6 ± 1.7	—	—	—	—	—	
041223	2.196	3.104	$-0.977^{+0.303}_{-0.286}$	$93.1^{+15.7}_{-15.8}$	49.6	10.2 ± 1.8	—	—	—	—	—	
041223	3.104	4.220	$-1.155^{+0.148}_{-0.146}$	$188.0^{+16.2}_{-16.2}$	58.1	19.4 ± 1.9	—	—	—	—	—	
041223	4.220	4.864	$-0.896^{+0.100}_{-0.098}$	$466.0^{+27.4}_{-27.4}$	53.7	52.3 ± 3.4	—	—	—	—	—	
041223	4.864	5.372	$-1.148^{+0.153}_{-0.152}$	$296.0^{+26.8}_{-26.9}$	61.6	30.5 ± 3.1	—	—	—	—	—	
041223	5.372	9.768	$-1.159^{+0.092}_{-0.092}$	$158.0^{+8.0}_{-8.0}$	48.5	16.2 ± 0.9	—	—	—	—	—	
041223	9.768	11.524	$-1.415^{+0.360}_{-0.365}$	$48.2^{+10.3}_{-10.4}$	54.7	4.6 ± 1.1	—	—	—	—	—	
041223	11.524	12.840	$-1.105^{+0.191}_{-0.188}$	$126.0^{+13.2}_{-13.3}$	66.2	13.1 ± 1.5	—	—	—	—	—	
041223	12.840	13.192	$-0.701^{+0.168}_{-0.162}$	$337.0^{+33.6}_{-34.0}$	69.8	41.1 ± 4.1	—	—	—	—	—	
041223	13.192	14.400	$-0.937^{+0.183}_{-0.176}$	$133.0^{+14.7}_{-14.7}$	77.0	14.7 ± 1.7	—	—	—	—	—	
041223	14.400	14.680	$-1.094^{+0.204}_{-0.201}$	$269.0^{+34.1}_{-34.1}$	63.5	28.2 ± 4.0	—	—	—	—	—	
041223	14.680	15.348	$-1.071^{+0.315}_{-0.301}$	$96.1^{+18.4}_{-18.4}$	62.3	10.1 ± 2.1	—	—	—	—	—	
041223	15.348	16.188	$-0.976^{+0.111}_{-0.11}$	$372.0^{+22.9}_{-22.9}$	69.7	40.6 ± 2.8	—	—	—	—	—	
041223	16.188	17.436	$-1.138^{+0.150}_{-0.147}$	$173.0^{+14.9}_{-14.9}$	62.4	17.9 ± 1.7	—	—	—	—	—	
041223	17.436	20.056	$-0.934^{+0.074}_{-0.073}$	$294.0^{+12.5}_{-12.6}$	67.4	32.6 ± 1.5	$-0.456^{+0.323}_{-0.3}$	$189.8^{+204.7}_{-53.3}$	$47.5^{+17.4}_{-12.1}$	59.7	31.9 ± 1.6	
041223	20.056	21.108	$-0.994^{+0.102}_{-0.101}$	$369.0^{+20.9}_{-20.9}$	52.2	40.0 ± 2.5	—	—	—	—	—	
041223	21.108	21.684	$-0.867^{+0.101}_{-0.099}$	$549.0^{+32.2}_{-32.3}$	64.9	62.4 ± 4.0	—	—	—	—	—	
041223	21.684	22.524	$-1.146^{+0.135}_{-0.134}$	$258.0^{+20.3}_{-20.3}$	59.6	26.5 ± 2.3	—	—	—	—	—	
041223	22.524	23.104	$-0.951^{+0.118}_{-0.116}$	$399.0^{+27.8}_{-27.8}$	60.6	44.0 ± 3.4	—	—	—	—	—	

[a]In the unit of 10^{-4} ph cm^{-2} s^{-1} keV^{-1}.

[b]In the unit of 10^{-8} ergs cm^{-2} s^{-1}.

[c]In the unit of 10^{-3} ph cm^{-2} s^{-1} keV^{-1}.

Table 8: BAT GRB T_{90} and T_{50} durations in the 140-220 keV band at the GRB rest frame.

GRB	T_{90}^{src} (s)	T_{50}^{src} (s)	Note
050126	8.73	4.80	
050223	—	—	(1)
050315	13.99	6.93	
050318	5.68	3.02	
050319	33.29	28.15	
050401	8.37	6.53	
050416A	—	—	(1)
050505	11.37	4.55	
050509B	—	—	(1)
050525A	4.24	2.89	
050603	2.53	0.57	
050724	—	—	(1)
050730	28.67	13.00	
050801	1.10	0.79	
050802	4.72	2.29	
050814	24.81	7.91	
050820A	—	—	(2)
050904	26.48	12.50	
050908	1.11	0.50	
050922C	1.56	0.63	
051016B	—	—	(1)
051109A	11.78	8.36	
051111	18.82	6.27	
051221A	0.17	0.08	
060115	28.80	19.86	
060124	3.94	2.73	
060206	1.10	0.43	
060210	35.74	6.24	
060218	—	—	(2)
060223A	1.93	0.70	
060418	19.28	6.43	
060502A	6.69	2.95	
060505	—	—	(1)
060510B	44.87	19.78	

[1]battblocks failed because of the weak signal in the light curve.

[2]The event data of the part of the burst emission are not available.

Table 9: Redshifts of Swift GRBs

GRB	Redshift	Reference
050126	1.290	(2)
050223	0.584	(3)
050315	1.950	(4)
050318	1.444	(4)
050319	3.2425	(1)
050401	2.8983	(1)
050416A	0.6528	(5)
050505	4.275	(6)
050509B	0.226	(7)
050525A	0.606	(8)
050603	2.821	(9)
050724	0.258	(10)
050730	3.9693	(10)
050801	1.38	(1)
050802	1.7102	(1)
050814	5.3	(11)
050820A	2.6147	(1)
050824	0.8278	(1)
050826	0.296	(12)
050904	6.295	(13)
050908	3.3467	(1)
050922C	2.1995	(1)
051016B	0.9364	(14)
051109A	2.346	(15)

[1]Fynbo et al. ApJS, 185, 526 (2009)

[2]Berger E. et al. ApJ, 629, 328 (2005)

[3]Pellizza, L.J. et al. A&A, 459, L5 (2006)

[4]Berger, E. et al. ApJ, 634, 501 (2005)

[5]Soderberg, A.M. et al. ApJ, 661, 982 (2007)

[6]Berger, E. et al. ApJ, 642, 979 (2006)

[7]Gehrels, N. et al. Nature, 437, 851 (2005)

[8]Della Valle, M. et al. ApJ, 642, L103 (2006)

[9]Berger, E. et al. GCN Circ. 3520

[10]Berger, E. et al. Nature, 438, 988 (2005)

[11]Jakobsson, P. et al. A&A, 447, 897 (2006)

[12]Mirabal, N. et al. ApJ, 661, L127 (2007)

[13]Kawai, N. et al. Nature, 440, 184 (2006)

Table 10: Statistics of the BAT2 GRB catalog

Class	Number of GRBs	Fraction	Classification
L-GRB	424	89%	$T_{90} \geq 2$ s
S-GRB	38	8%	$T_{90} < 2$ s
S-GRB w/E.E.	10	2%	Norris et al. (2010)
Un-known	4	1%	Incomplete/lost data

Table 11. Spectral parameters of the initial short spikes of the short GRBs with E.E.

GRB	start (s)	stop (s)	$\alpha^{\rm PL}$	$K_{50}^{\rm PL}$(a)	χ^2
050724	−0.024	0.416	$-1.50^{+0.14}_{-0.14}$	$515.2^{+40.9}_{-41.1}$	50.9
051227	−0.848	0.828	$-0.94^{+0.23}_{-0.25}$	$61.0^{+7.9}_{-8.0}$	65.6
061006	−23.24	−22.20	$-0.86^{+0.07}_{-0.07}$	$445.3^{+17.7}_{-17.8}$	50.8
061210	−0.004	0.080	$-0.69^{+0.12}_{-0.12}$	$2755.1^{+209.0}_{-209.8}$	58.2
070714B	−1	−2	$-0.98^{+0.08}_{-0.08}$	$158.2^{+7.2}_{-7.2}$	43.0
071227	−0.144	1.872	$-0.90^{+0.22}_{-0.24}$	$98.6^{+12.1}_{-12.3}$	51.0
080503	−0.048	0.436	$-1.62^{+0.23}_{-0.23}$	$130.6^{+19.3}_{-19.6}$	66.0
090531B	0.252	1.300	$-0.99^{+0.16}_{-0.16}$	$148.4^{+12.0}_{-12.1}$	63.3
090715A	−0.12	0.84	$-0.99^{+0.19}_{-0.20}$	$348.9^{+38.3}_{-38.8}$	55.0
090916	0.0	0.35	$-1.38^{+0.30}_{-0.30}$	$236.5^{+44.5}_{-44.5}$	72.6

[a]In the unit of 10^{-4} ph cm^{-2} s^{-1} keV^{-1}.

Table 12. BAT GRB energy fluence of the initial short spkes of the short GRB with E.E.

GRB Name	Spectral Model	S(15-25)	S(25-50)	S(50-100)	S(100-150)	S(15-150)
				(10^{-8} ergs cm^{-2})		
050724	PL	2.9 ± 0.4	5.3 ± 0.4	7.5 ± 0.8	5.7 ± 0.9	21.5 ± 1.9
051227	PL	0.8 ± 0.2	2.0 ± 0.3	4.2 ± 0.6	4.3 ± 1.0	11.3 ± 1.6
061006	PL	3.3 ± 0.3	8.9 ± 0.4	19.6 ± 0.8	21.0 ± 1.4	52.7 ± 2.3
061210	PL	1.4 ± 0.2	4.2 ± 0.4	10.5 ± 0.8	12.4 ± 1.5	28.4 ± 2.4
070714B	PL	3.7 ± 0.4	9.4 ± 0.5	19.2 ± 1.0	19.5 ± 1.6	51.8 ± 2.6
071227	PL	1.4 ± 0.4	3.9 ± 0.6	8.3 ± 1.1	8.8 ± 1.8	22.4 ± 2.9
080503	PL	0.9 ± 0.2	1.5 ± 0.2	2.0 ± 0.4	1.5 ± 0.4	5.9 ± 0.9
090531B	PL	1.2 ± 0.2	3.1 ± 0.3	6.3 ± 0.6	6.3 ± 1.0	16.8 ± 1.6
090715A	PL	2.7 ± 0.6	6.7 ± 0.9	13.4 ± 1.5	13.5 ± 2.4	36.3 ± 4.0
090916	PL	0.9 ± 0.3	1.9 ± 0.4	2.9 ± 0.6	2.3 ± 0.8	8.0 ± 1.6

Table 13. $E_{\rm peak}^{\rm src}$ and $E_{\rm iso}$ values for *Swift* GRBs.

GRB	z	$E_{\rm peak}^{\rm src}$ (keV)	$E_{\rm iso}$ (10^{52} erg)
050416A	0.6528	22^{+5}_{-4}	$0.12^{+0.01}_{-0.02}$
050525A	0.606	129^{+6}_{-7}	$2.6^{+0.9}_{-0.2}$
060115	3.5328	297^{+92}_{-111}	$6.5^{+6.7}_{-1.5}$
060206	4.0559	410^{+195}_{-179}	$4.5^{+3.2}_{-1.0}$
060707	3.4240	274^{+66}_{-77}	$4.7^{+18.8}_{-0.8}$
060908	1.8836	414^{+399}_{-120}	$8.1^{+1.9}_{-4.5}$
060927	5.4636	276^{+97}_{-54}	13^{+3}_{-3}
071010B	0.947	88^{+21}_{-21}	$2.6^{+0.5}_{-0.4}$
071117	1.3308	112^{+315}_{-52}	$6.5^{+1.6}_{-4.4}$
080413B	1.1014	163^{+51}_{-46}	$1.7^{+2.2}_{-0.3}$
080603B	2.6892	277^{+95}_{-111}	$6.6^{+6.2}_{-1.2}$
080605	1.6403	766^{+1100}_{-243}	31^{+20}_{-12}
080916A	0.6887	200^{+120}_{-51}	$1.8^{+1.8}_{-1.0}$
090205	4.6497	214^{+58}_{-87}	$0.9^{+0.7}_{-0.3}$
090423	8.26	410^{+115}_{-88}	$9.5^{+2.6}_{-1.9}$
090424	0.544	236^{+127}_{-49}	$4.3^{+2.4}_{-1.4}$
090926B	1.24	175^{+24}_{-20}	$5.4^{+2.8}_{-2.0}$
091018	0.971	$55^{+6.8}_{-17}$	$0.7^{+0.3}_{-0.1}$
091029	2.752	229^{+94}_{-59}	$8.5^{+4.5}_{-2.5}$

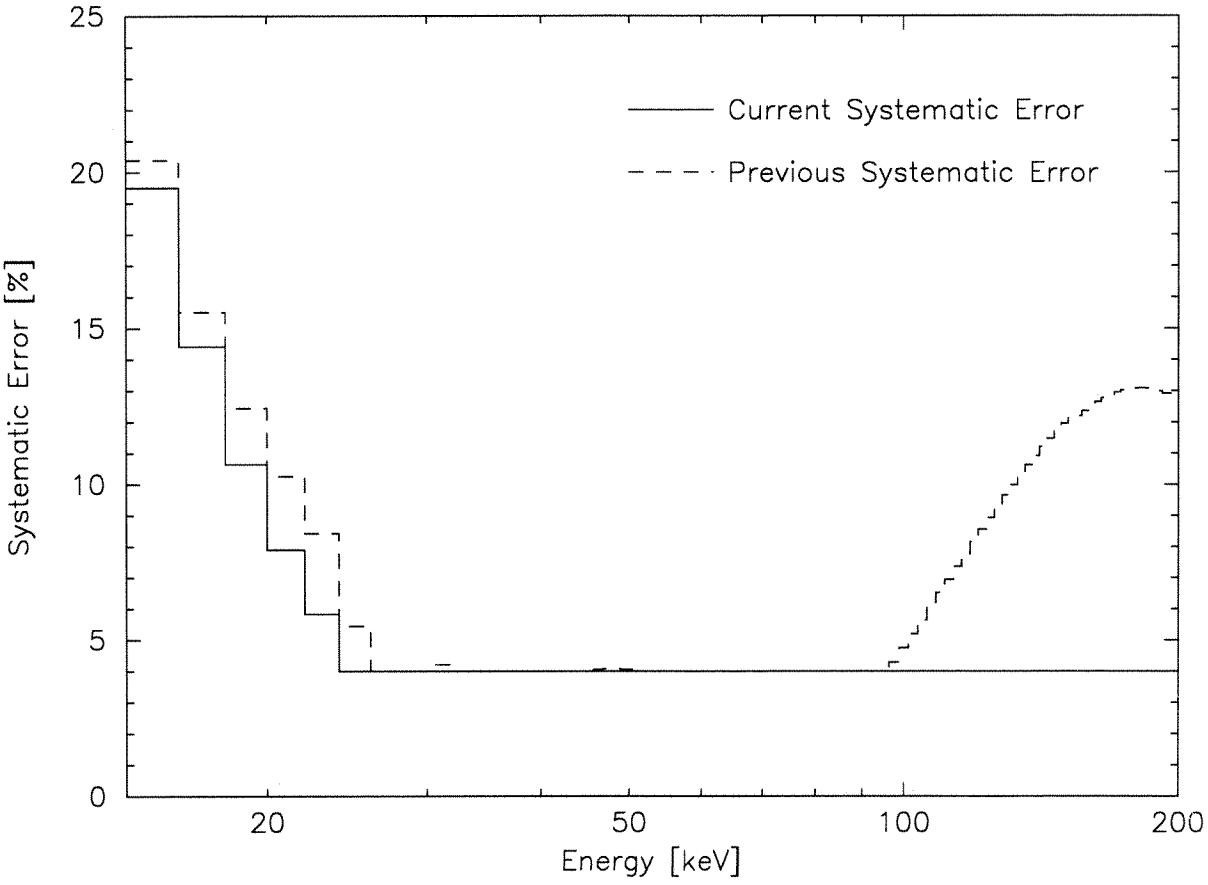

Fig. 1.— Systematic error as a function of energy. The current systematic error is shown in a solid line and the previous systematic error (used in the analysis of the BAT1 catalog) is shown in a dashed line.

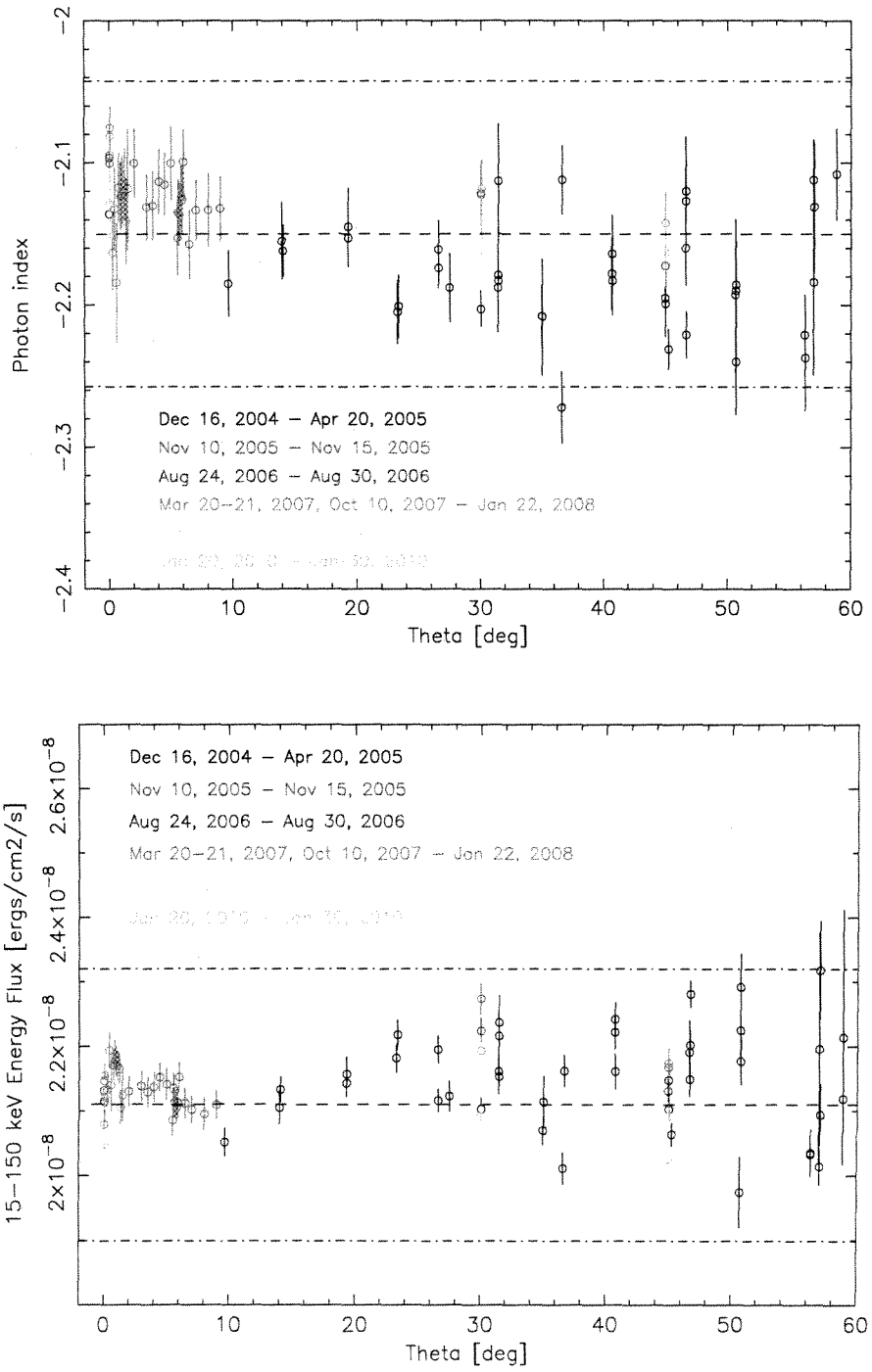

Fig. 2.— Power-law photon index (top) and the flux in the 15-150 keV band as a function of the incident angle of the Crab observed in different time periods. The horizontal dashed lines are the Crab canonical values of -2.15 for the photon index and 2.11×10^{-8} ergs cm^{-2} s^{-1} for the flux. The dashed dotted lines are $\pm 5\%$ of the photon index and $\pm 10\%$ of the flux canonical values.

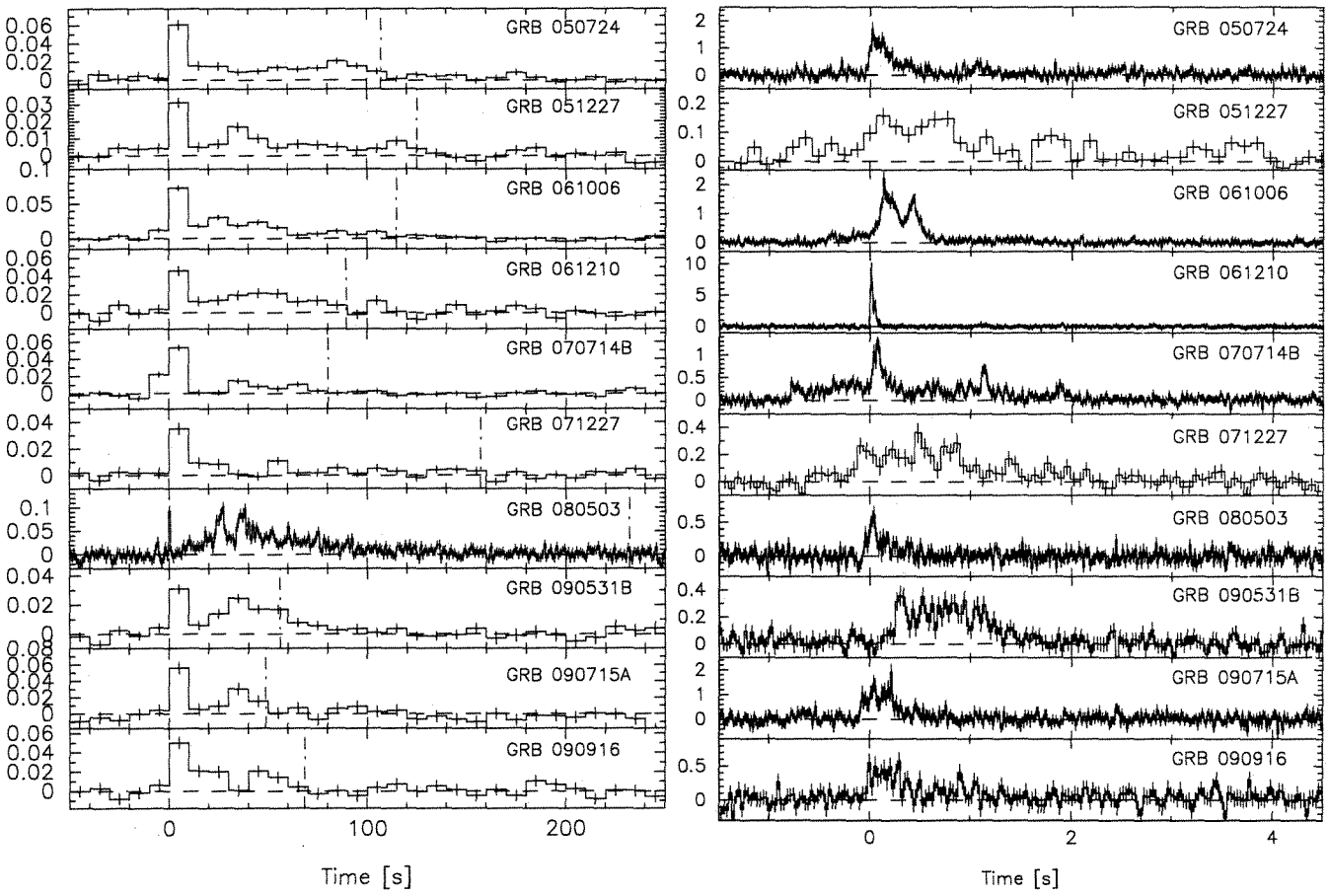

Fig. 3.— The BAT mask-weighted light curves of the 15-150 keV band in a course binning (left) and a fine binning (right) for short GRBs with extended emissions. The vertical dash-dotted lines in course binning light curves are showing the emission end time found by `battblocks`.

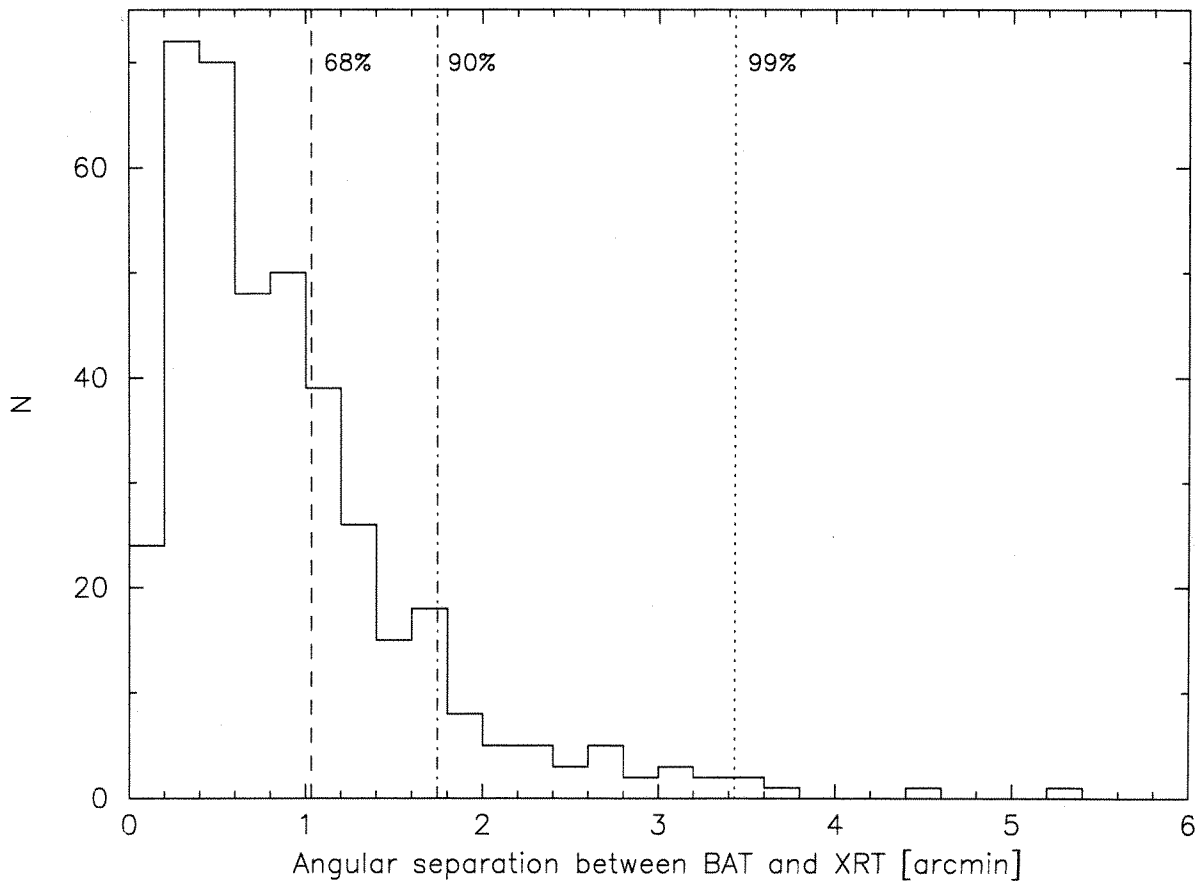

Fig. 4.— The histogram of the angular difference between the BAT ground position and the XRT position.

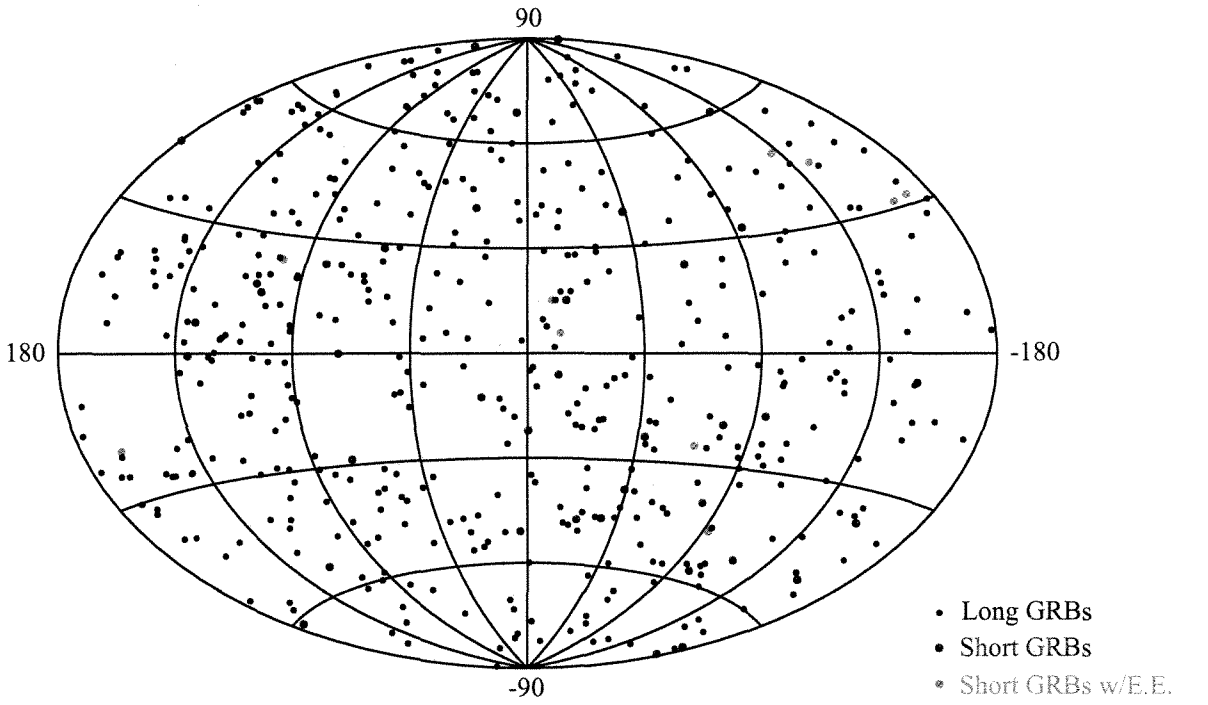

Fig. 5.— Sky distribution of the 476 BAT bursts in Galactic coordinates with long GRBs in black, short GRBs in red and short GRBs with extended emissions in green.

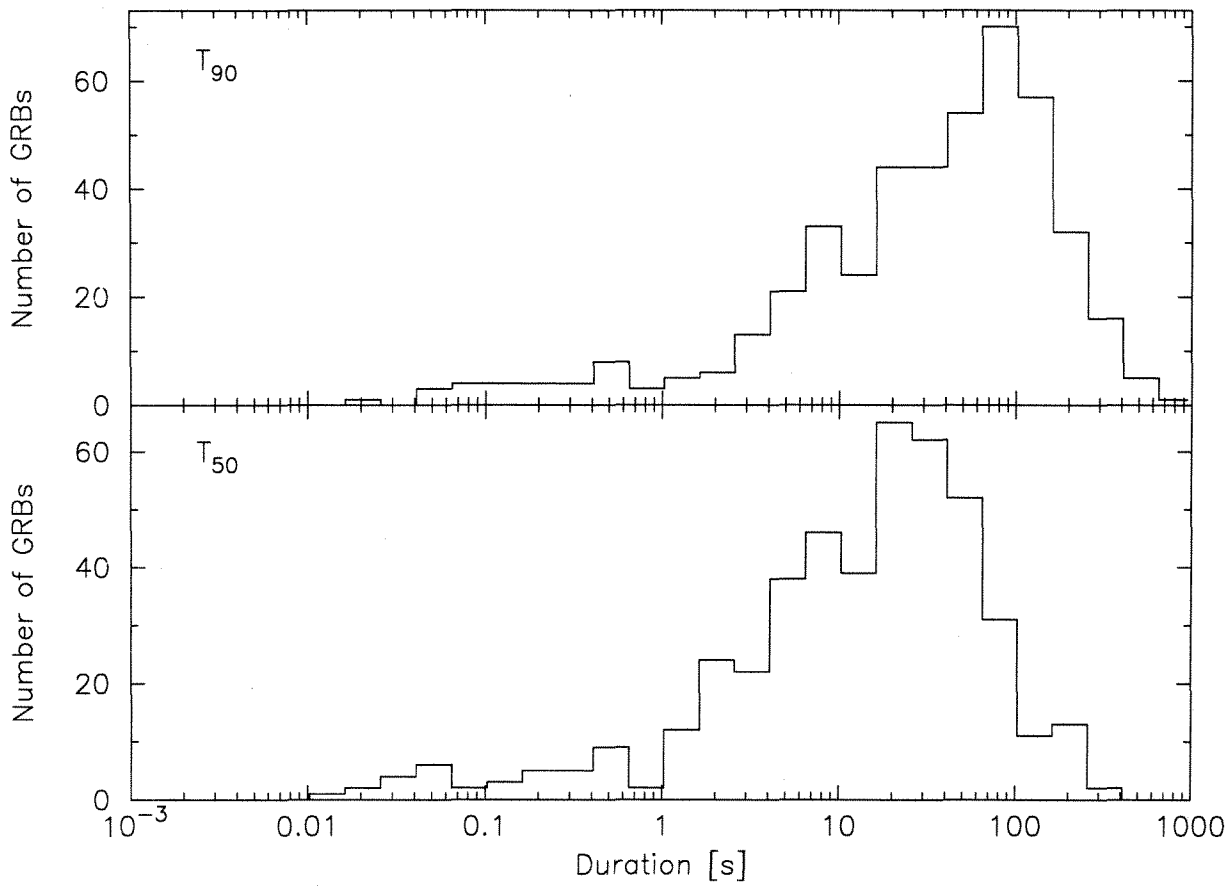

Fig. 6.— $T_{90}(top)$ and $T_{50}(bottom)$ distributions from the BAT mask-weighted light curves in the 15-350 keV band.

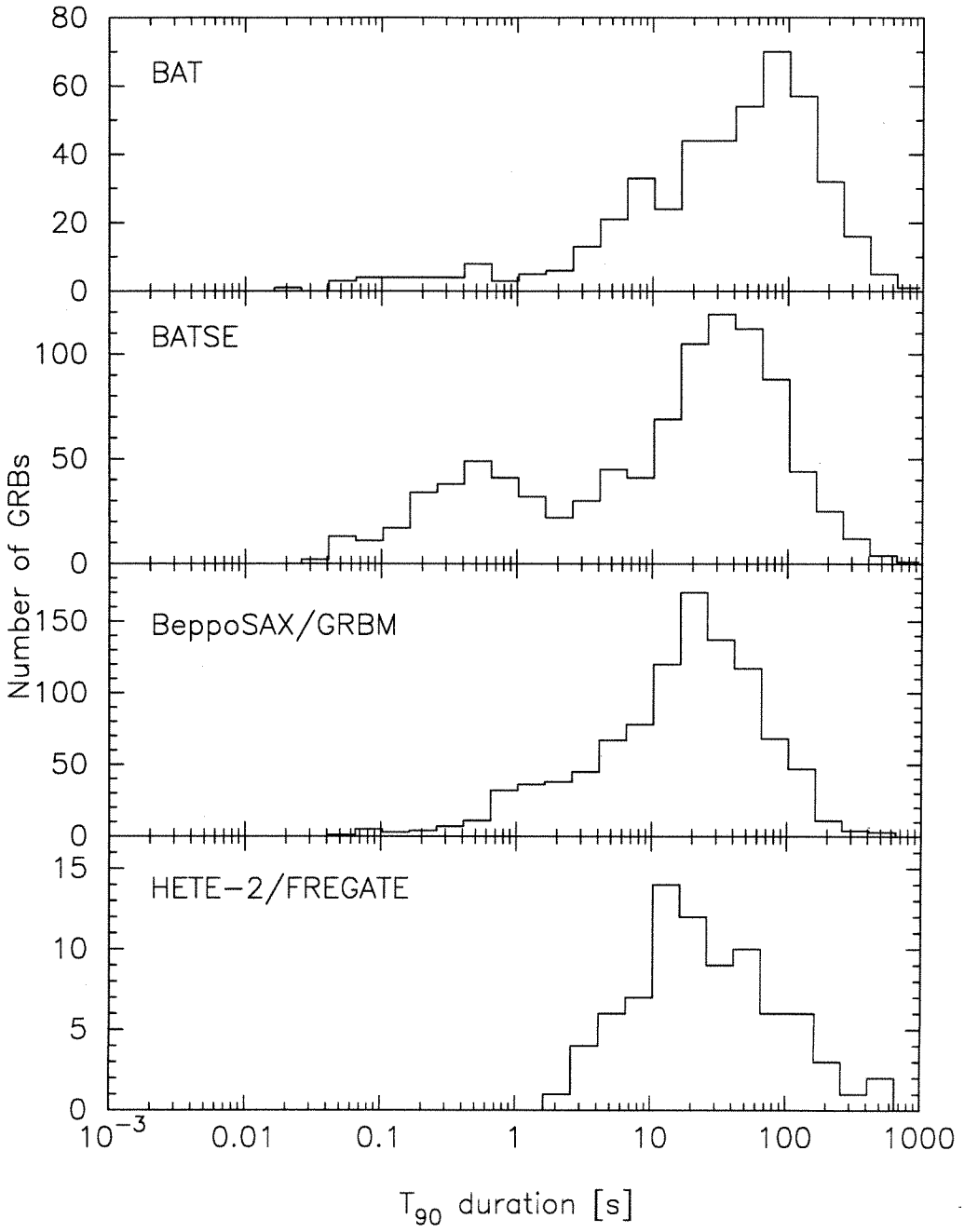

Fig. 7.— T_{90} distribution of BAT by the mask-weighted light curve in the 15-350 keV band, BATSE by the light curve in the 50-350 keV band, *BeppoSAX* by the light curve of the GRBM instrument in the 40-700 keV band, and HETE-2 by the light curve of the FREGATE instrument in the 6-80 keV band from top to bottom.

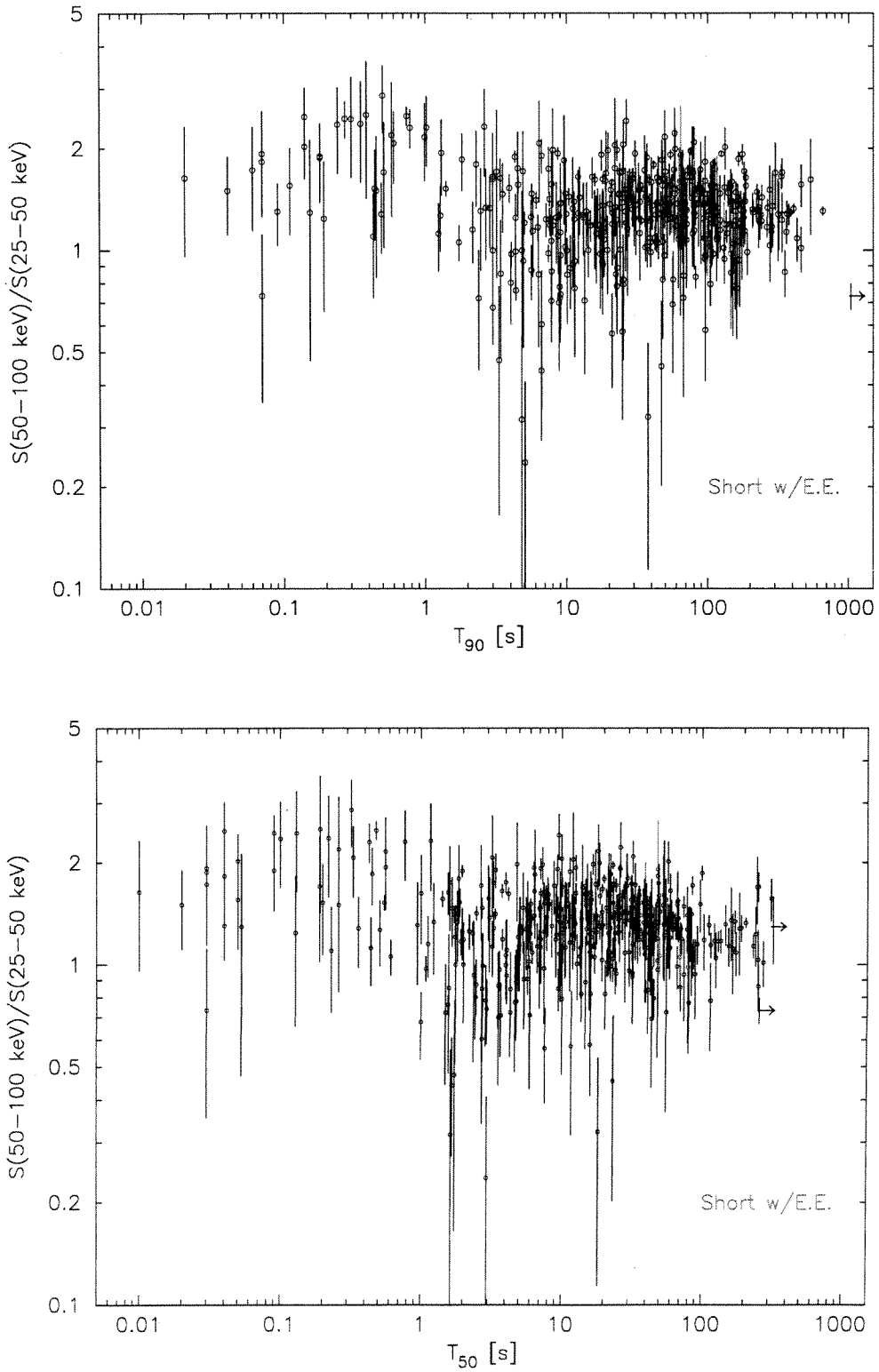

Fig. 8.— The fluence ratio between the 50-100 keV and the 25-50 keV bands and $T_{90}(top)$ and $T_{50}(bottom)$. Short GRBs with an E.E. are shown in red.

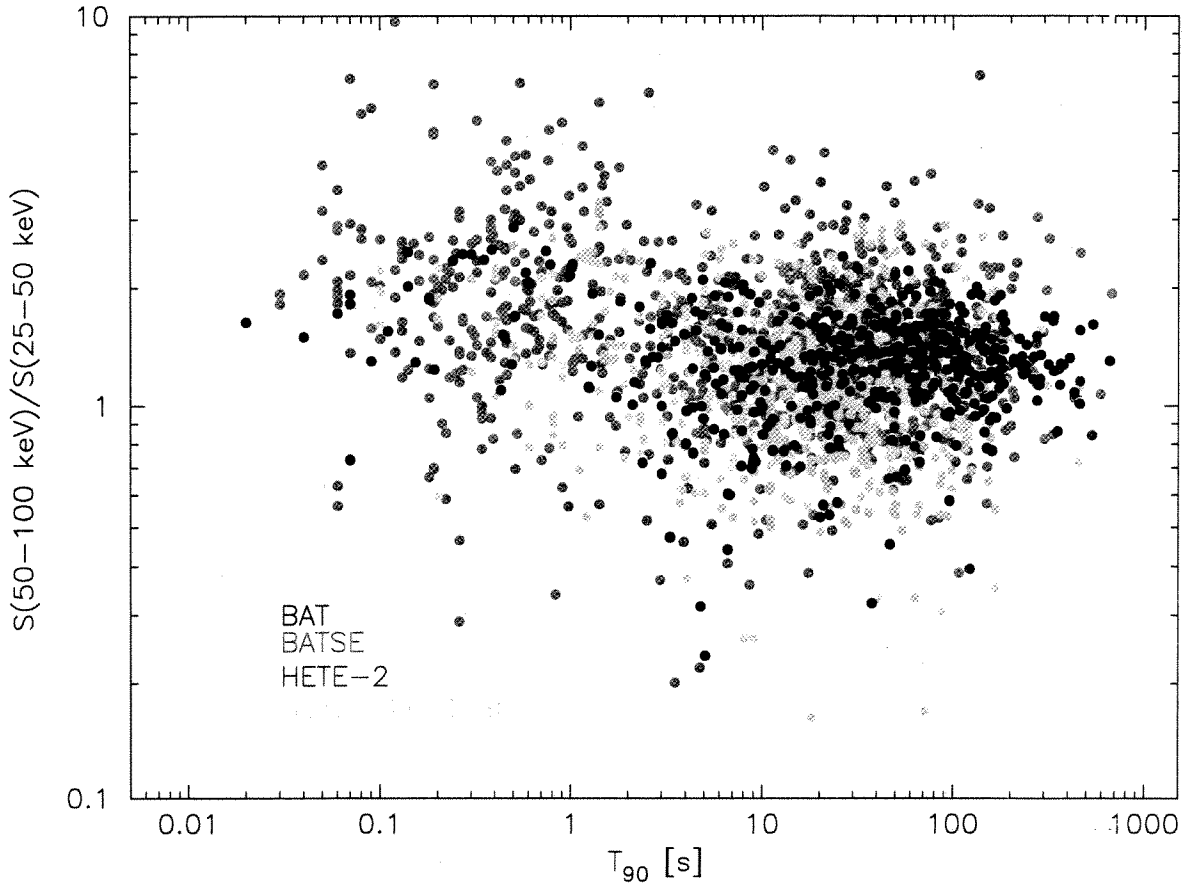

Fig. 9.— The fluence ratio between the 50-100 keV and the 25-50 keV bands versus T_{90} for BAT (black), BATSE (red), *HETE*-2 (blue) and *BeppoSAX* (green) GRBs.

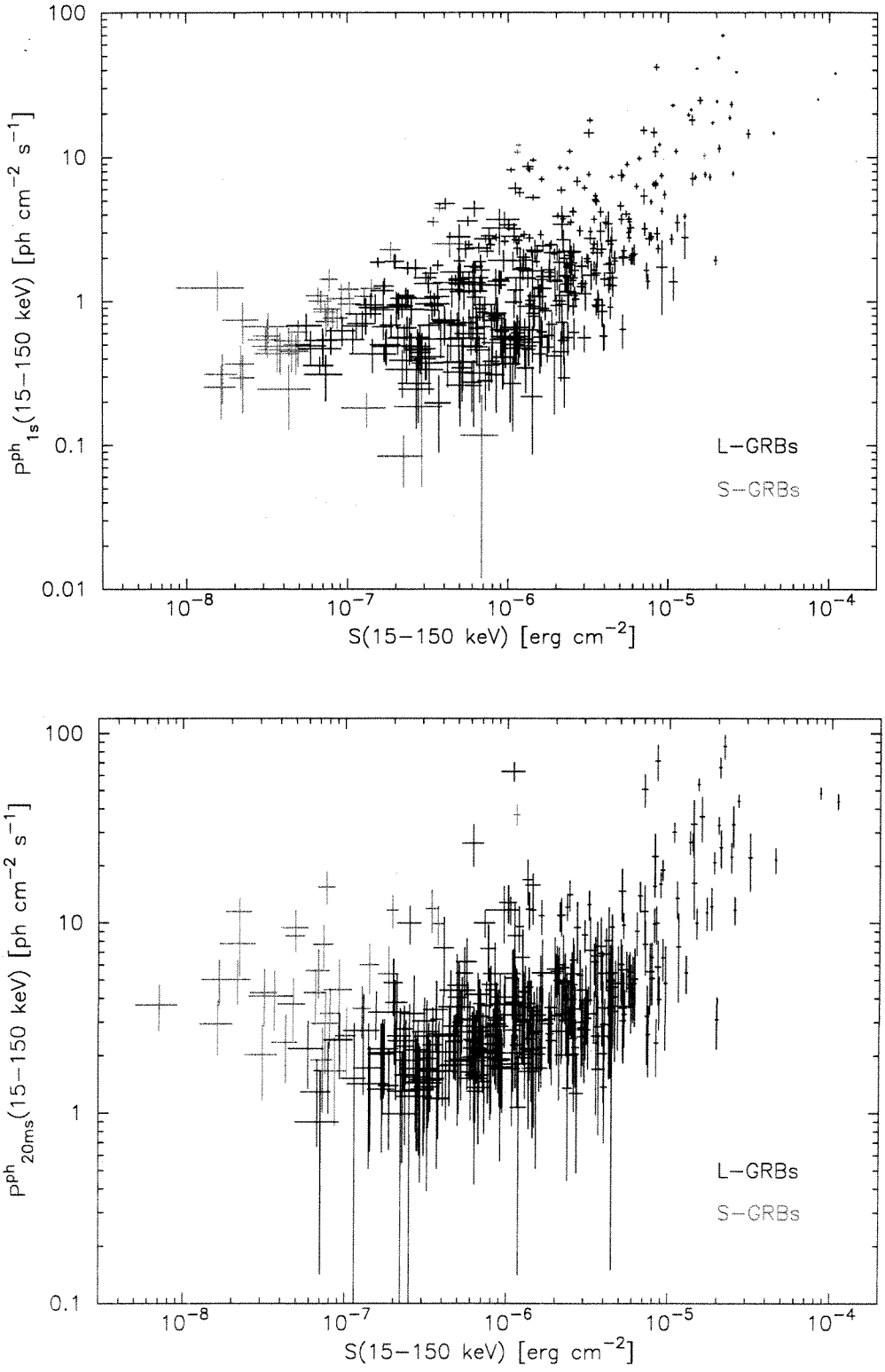

Fig. 10.— Distributions of 1 s peak photon flux (top) and 20 ms peak photon flux (bottom) in the 15-150 keV band and the energy fluence in the 15-150 keV band.

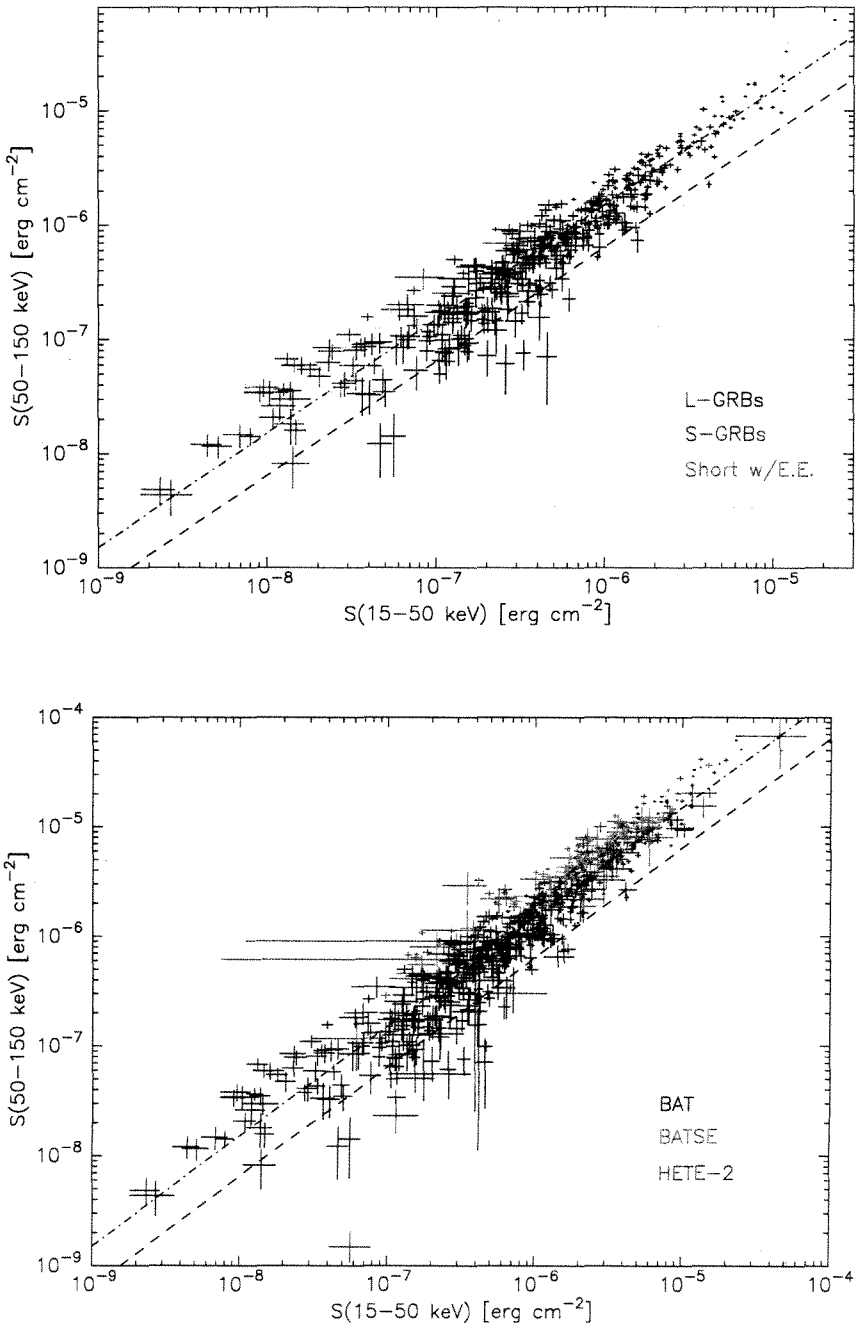

Fig. 11.— *Top*: Distribution of the energy fluence in the 50-150 keV band vs. that in the 15-50 keV band for the BAT GRBs. L-GRBs are in black, S-GRBs are in blue, S-GRBs with E.E. are in red, and the initial short spikes of S-GRBs with E.E. are in green. The dashed-dotted line is the case of the Band function of $\alpha = -1$, $\beta = -2.5$, and $E_{\rm peak}^{\rm obs} = 100$ keV. The dashed line is the case of the Band function of $\alpha = -1$, $\beta = -2.5$, and $E_{\rm peak}^{\rm obs} = 30$ keV. *Bottom*: Distribution in the same plane as top among different missions. The BAT sample is in black, the BATSE sample is in red, and the HETE-2 sample is in blue. The dashed-dotted and dashed lines are same as top.

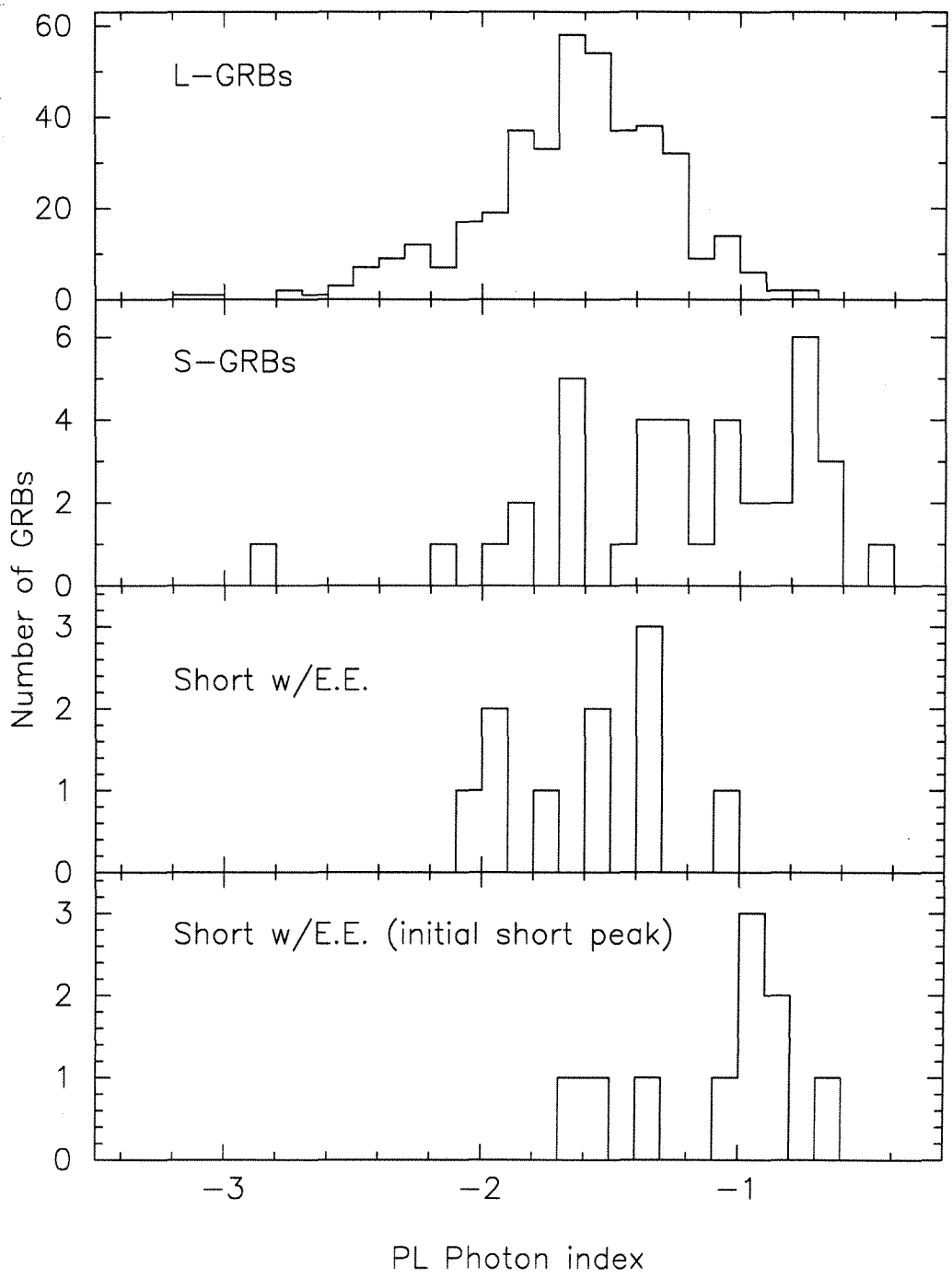

Fig. 12.— Histograms of the BAT time-averaged photon index in a PL fit for the L-GRBs, the S-GRBs, the S-GRBs with E.E. and the initial short spikes of the S-GRBs with E.E. from top to bottom.

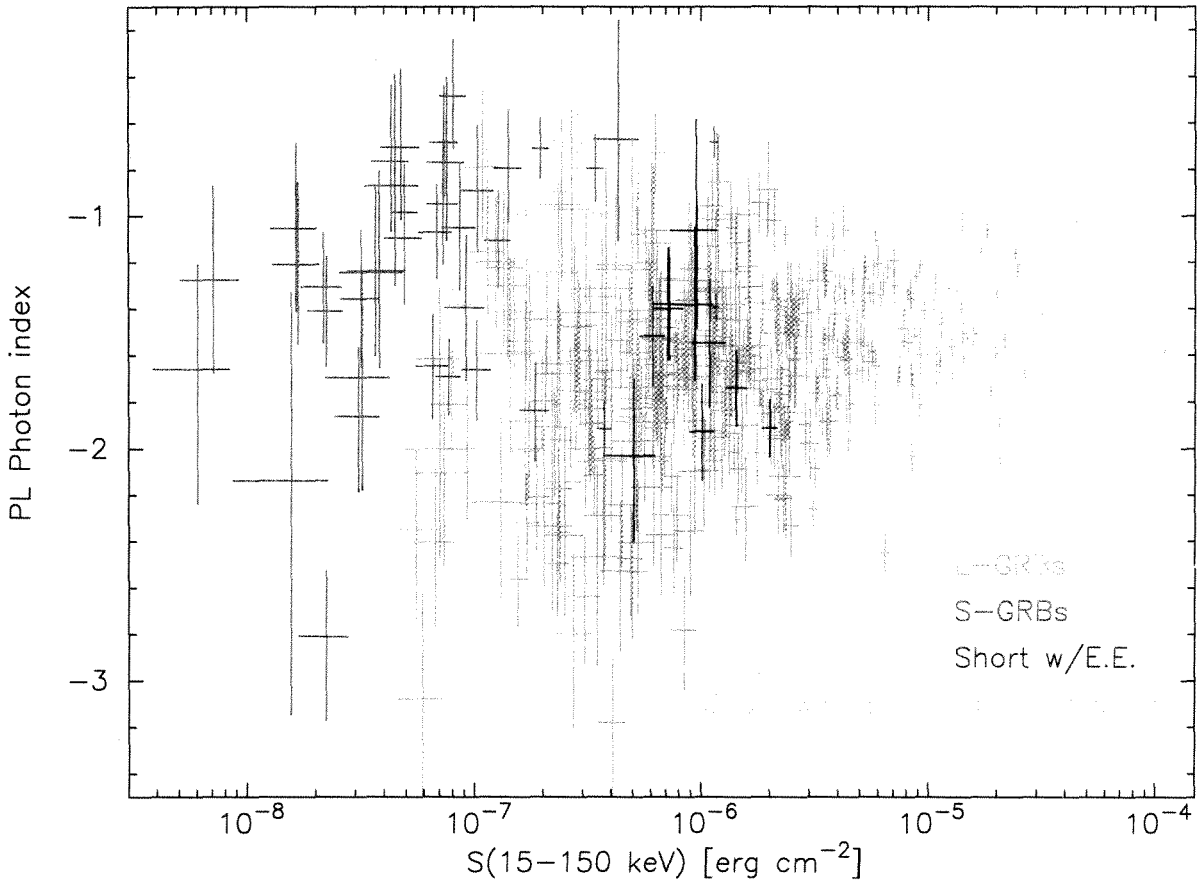

Fig. 13.— Distribution of the BAT PL photon index vs. the energy fluence in the 15-150 keV band for the L-GRBs (light gray), the S-GRBs (red), the S-GRBs with E.E. (blue) and the initial short spikes of the S-GRBs with E.E.(green).

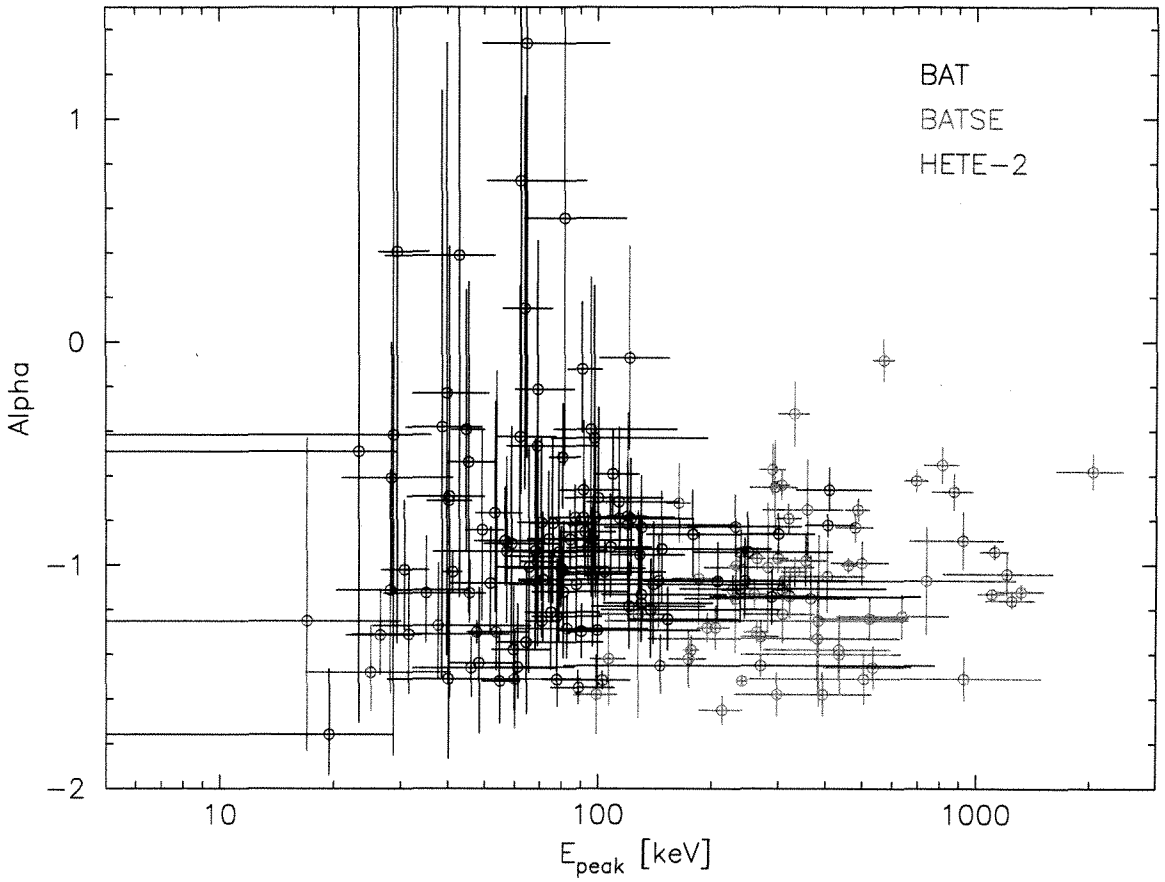

Fig. 14.— Distributions of the photon index α and $E_{\rm peak}$ in a CPL fit for the BAT (black), the BATSE (red) and the HETE-2 (blue) GRBs.

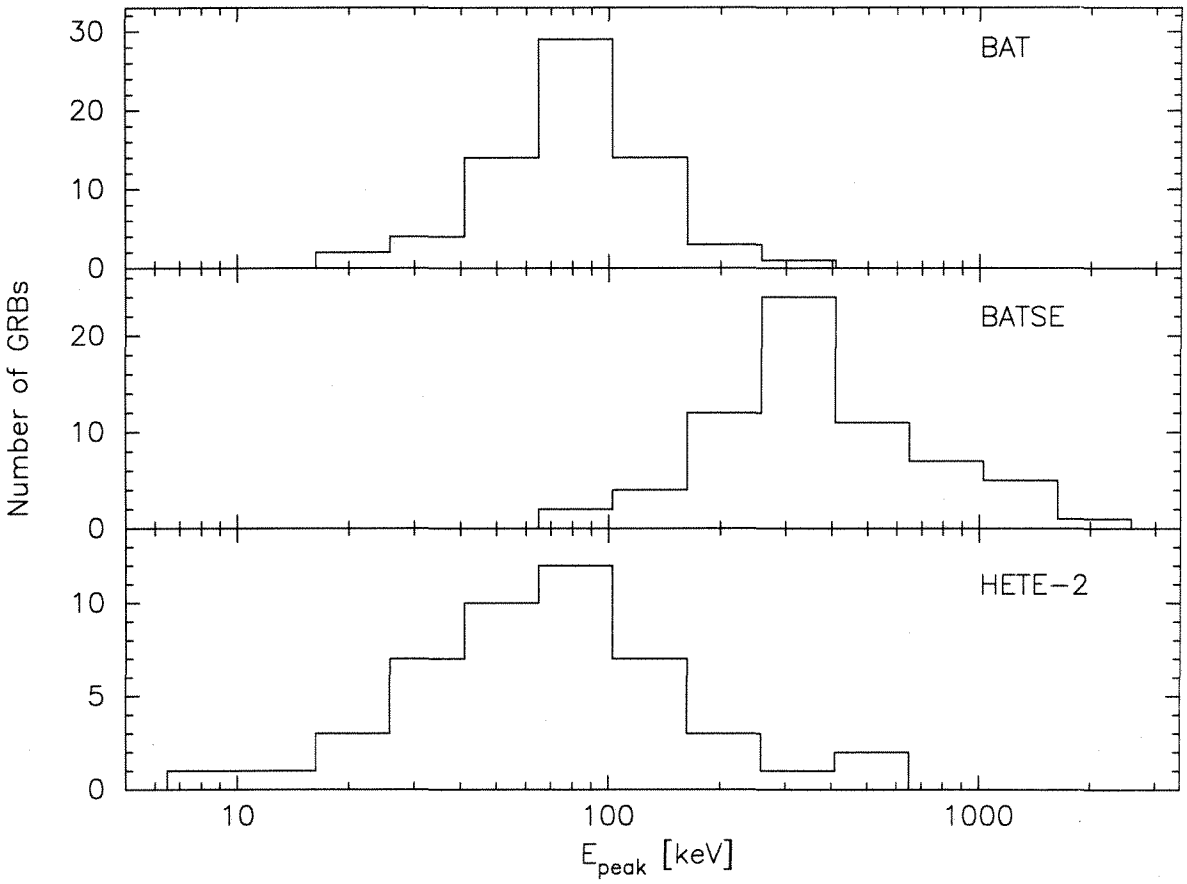

Fig. 15.— Histograms of $E_{\rm peak}$ in a CPL fit for the BAT (top), the BATSE (middle) and the HETE-2 (bottom) GRBs.

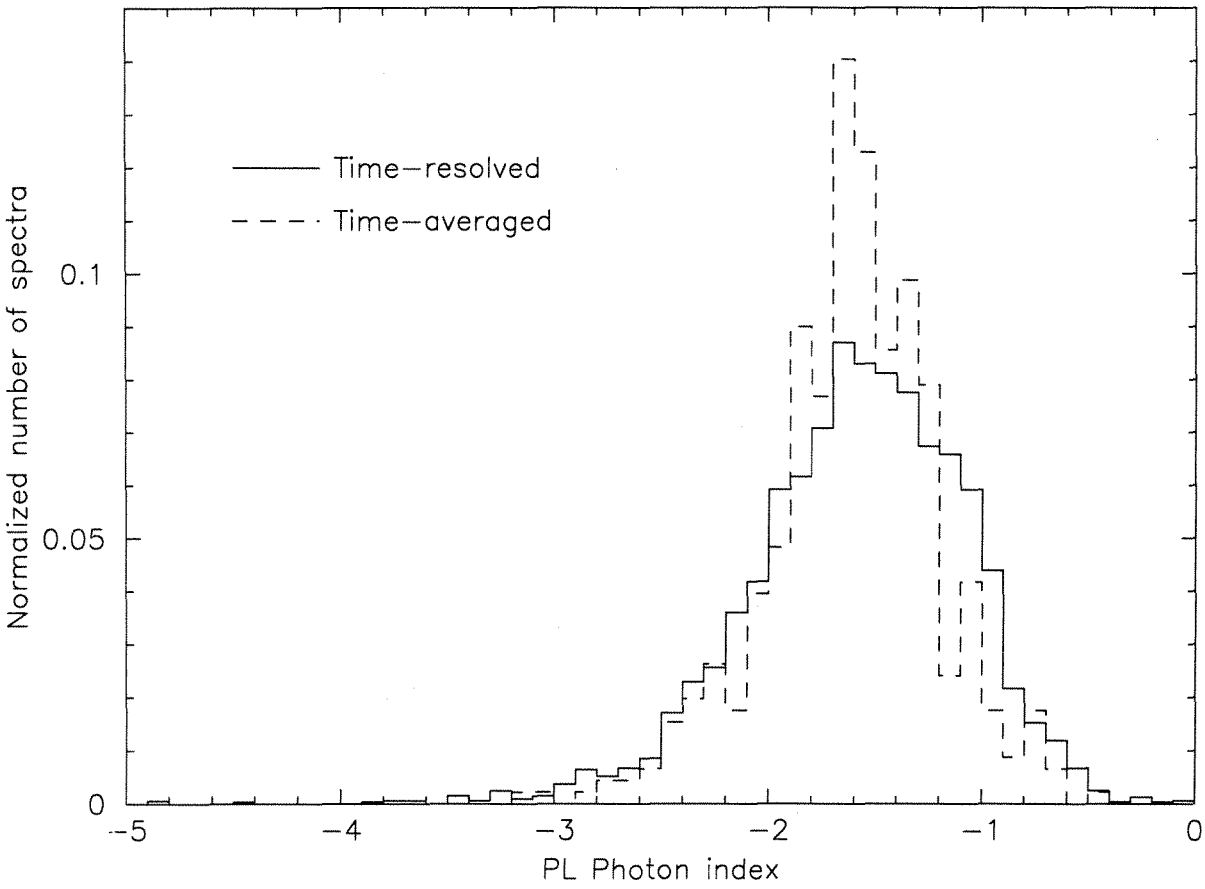

Fig. 16.— Histograms of the BAT photon index in a PL fit for the time-resolved (solid) and the time-averaged (dash) spectra. The histograms are normalized by a total number of spectra.

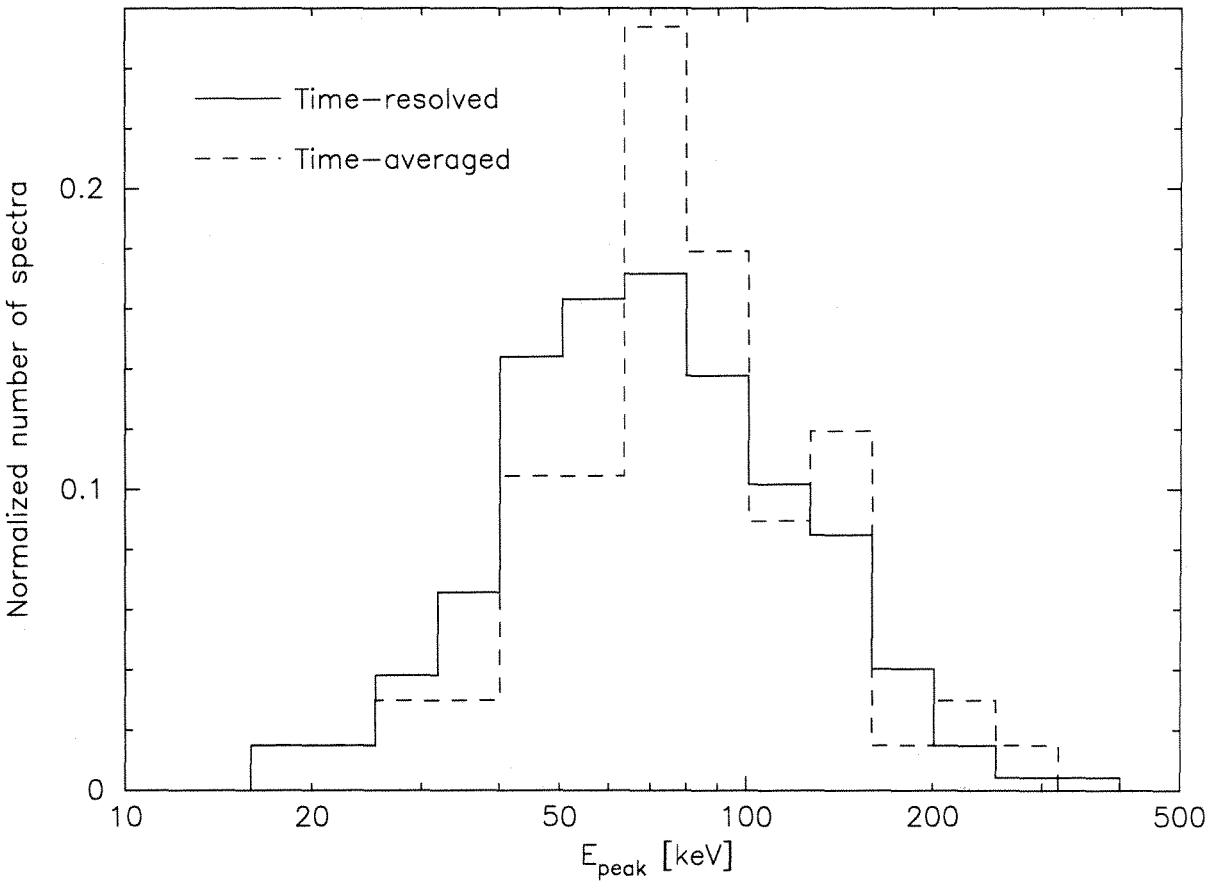

Fig. 17.— Histograms of the BAT $E_{\rm peak}$ in a CPL fit for the time-resolved (solid) and the time-averaged (dash) spectra. The histograms are normalized by a total number of spectra.

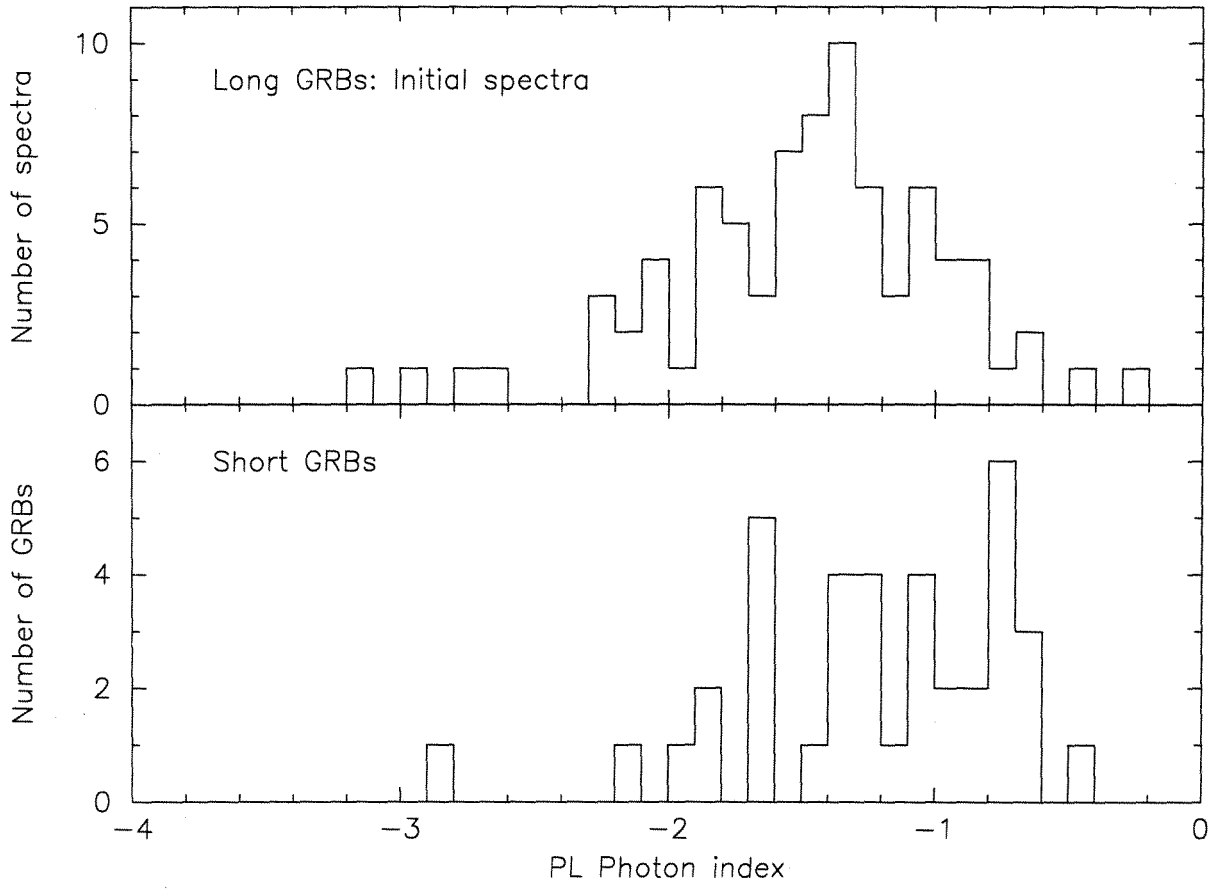

Fig. 18.— Histograms of the BAT photon index in a PL fir for initial spectra of long GRBs (top) and for short GRBs (bottom).

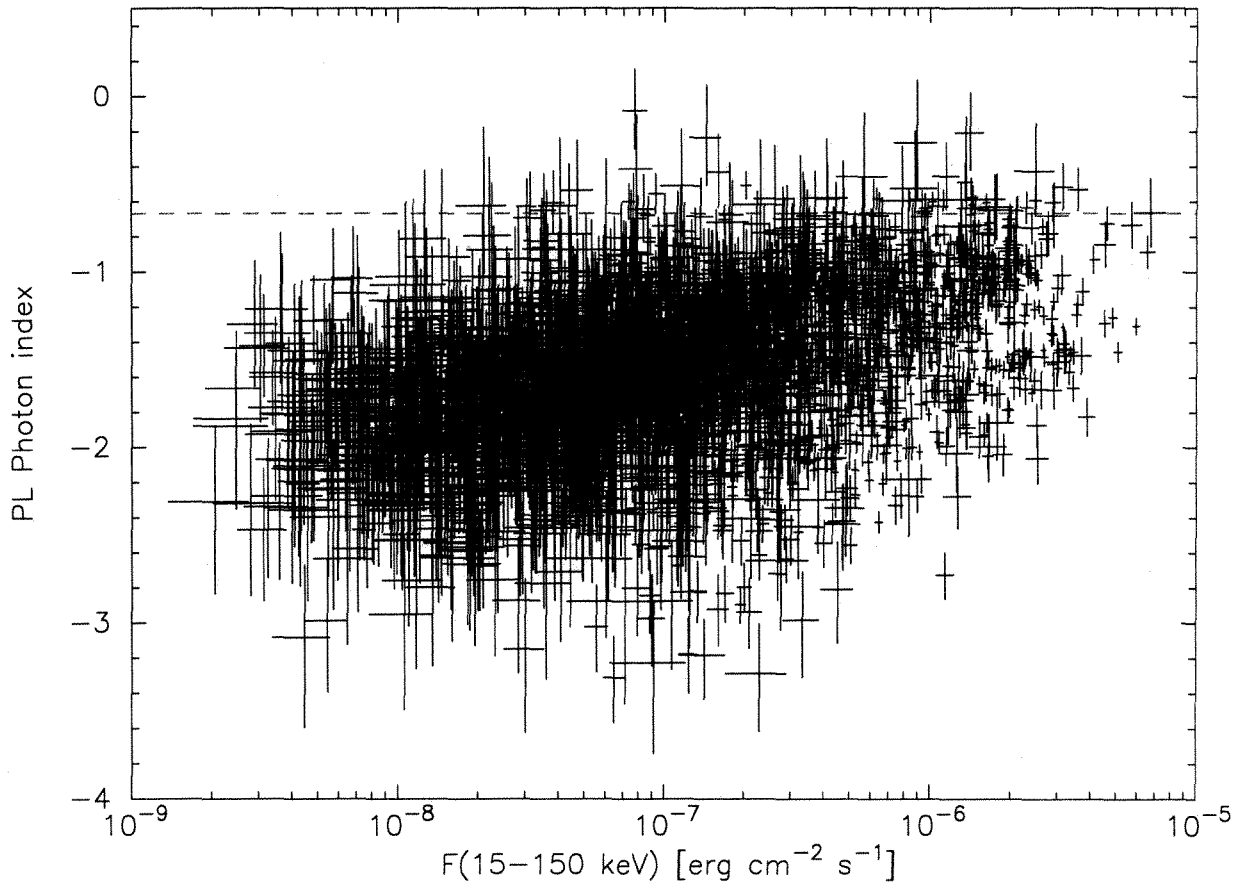

Fig. 19.— Distribution of the BAT photon index in a PL fit vs. energy flux in the 15-150 keV band. The red dashed line shows the photon index of -2/3. The total number of time-resolved spectra is 2968.

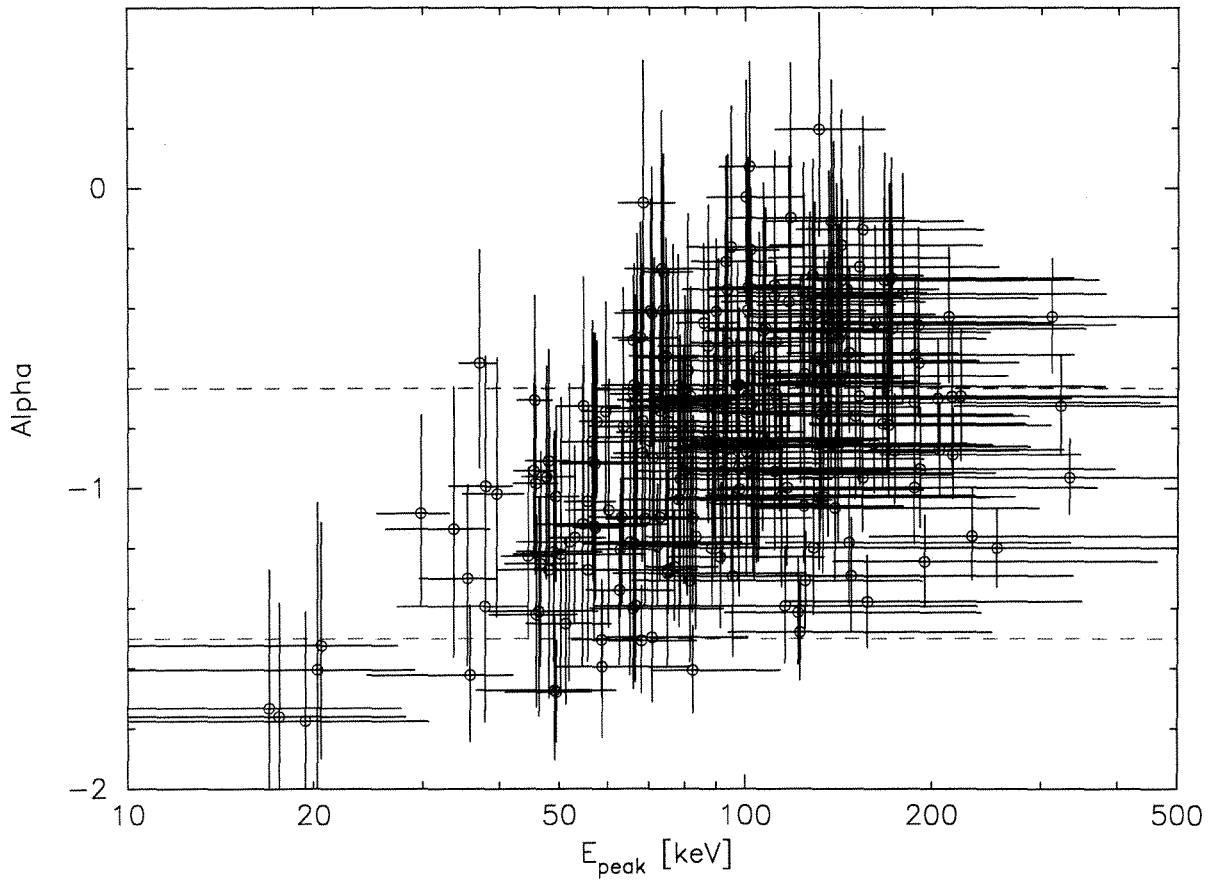

Fig. 20.— Distribution of the BAT photon index α and $E_{\rm peak}$ in a CPL fit. The red dashed lines show the photon index region from $-3/2$ to $-2/3$. The total number of time-resolved spectra is 234.

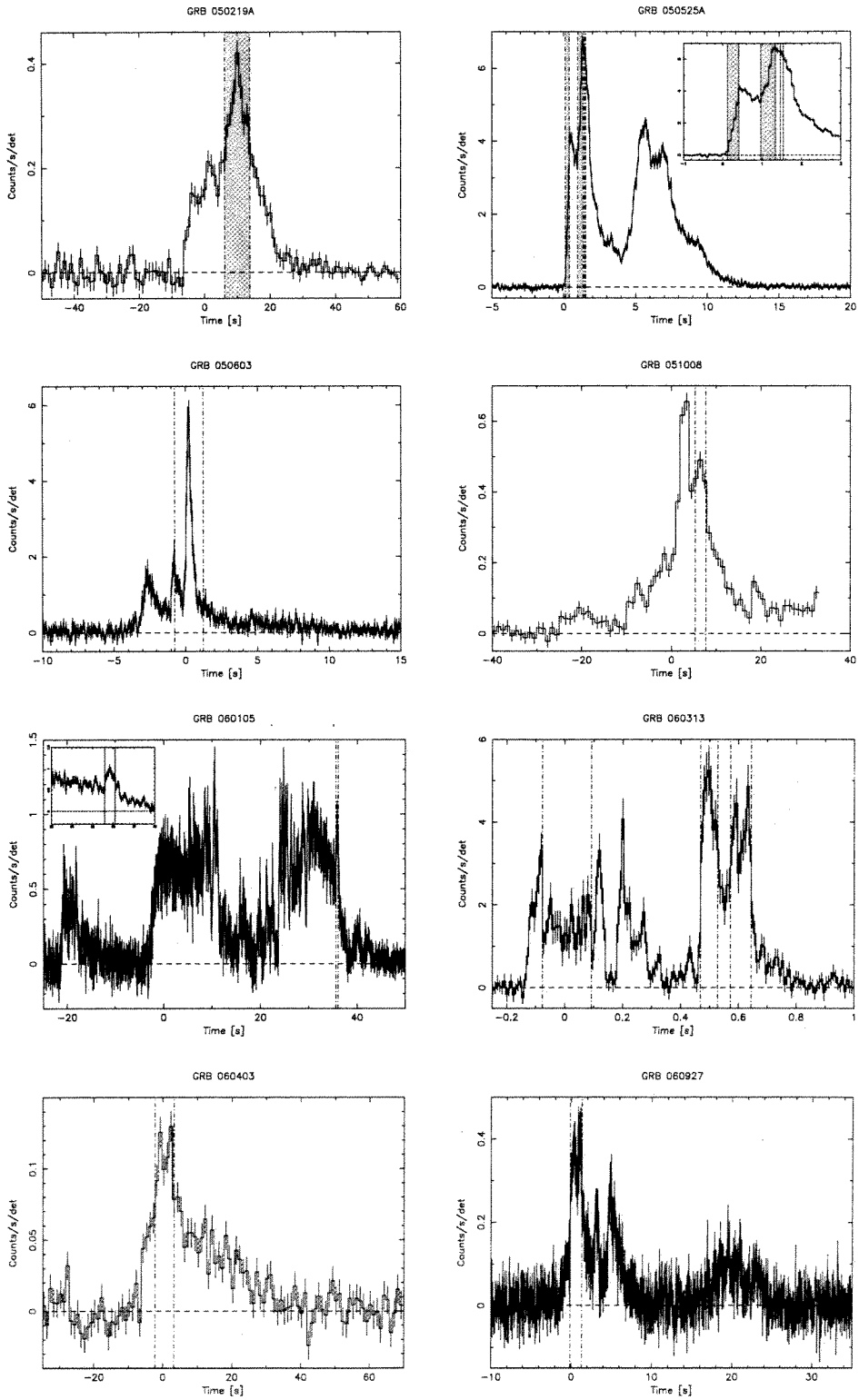

Fig. 21.— The BAT light curve with the interval showing the spectra exceeding the limits of the SSM as hatches. The red hatch is the interval exceeding the limit $> 3.2\ \sigma$. The yellow hatch is the interval exceeding the limit $> 1.6\ \sigma$ but $< 3.2\ \sigma$.

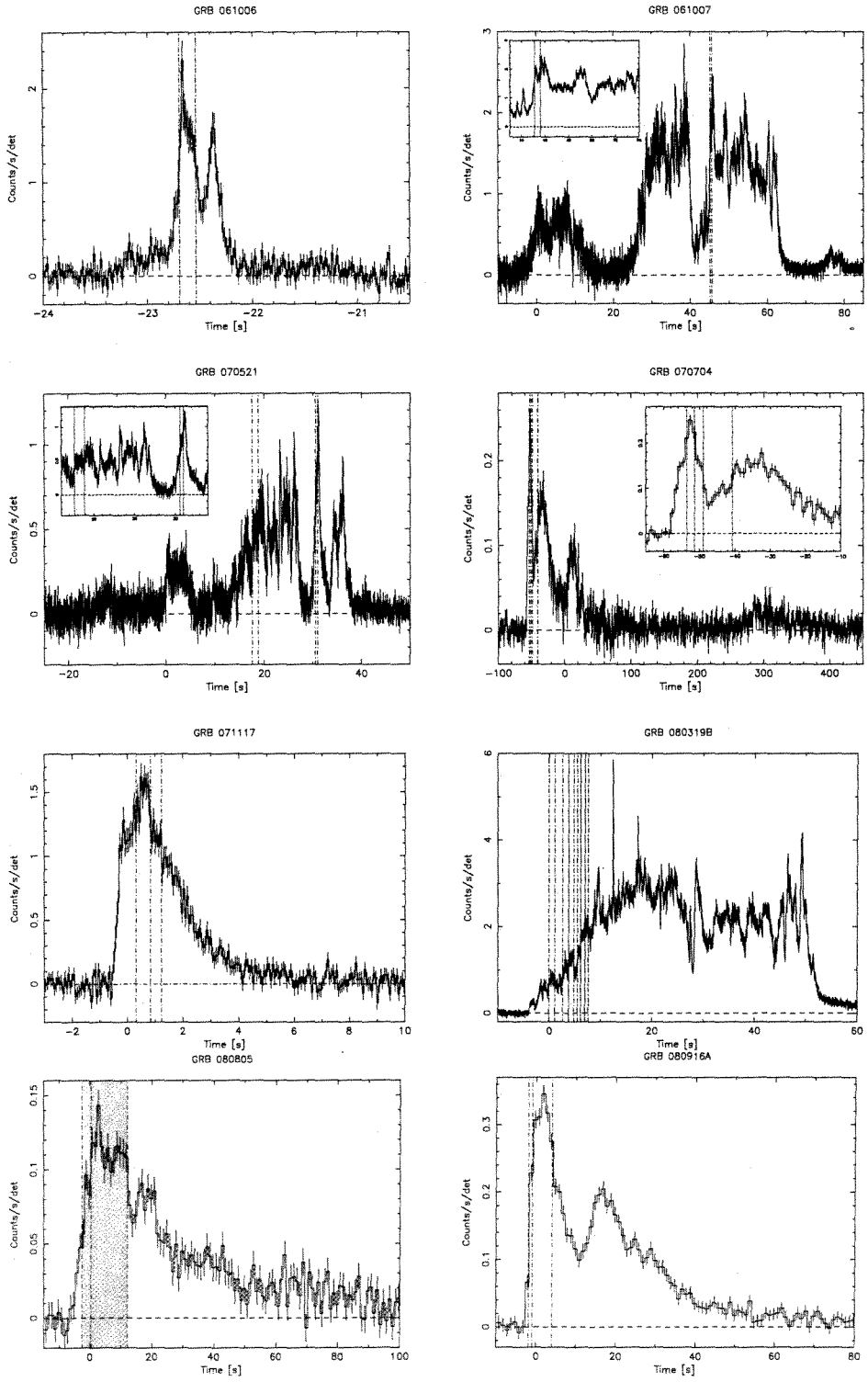

Fig. 22.— Continue

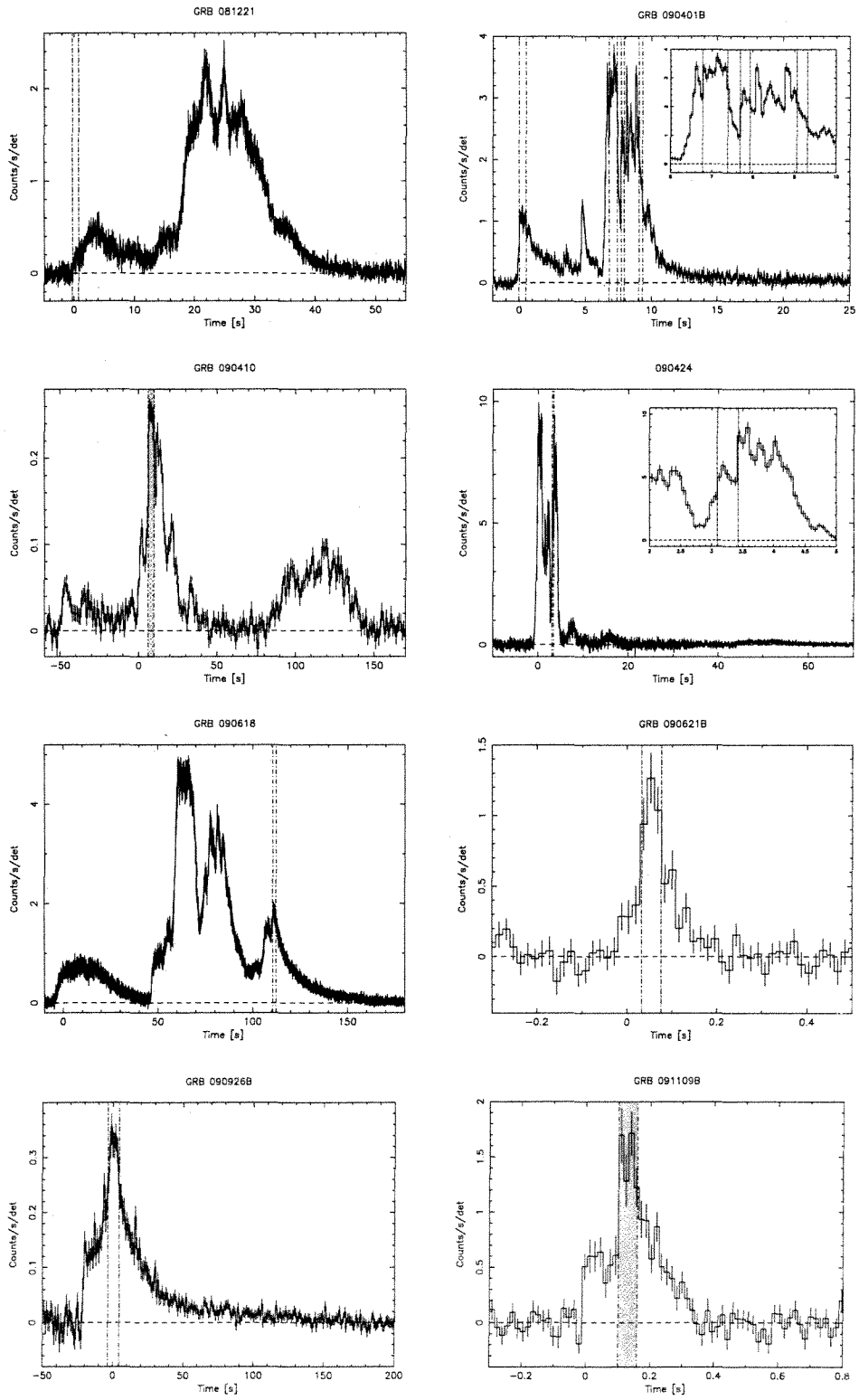

Fig. 23.— Continue

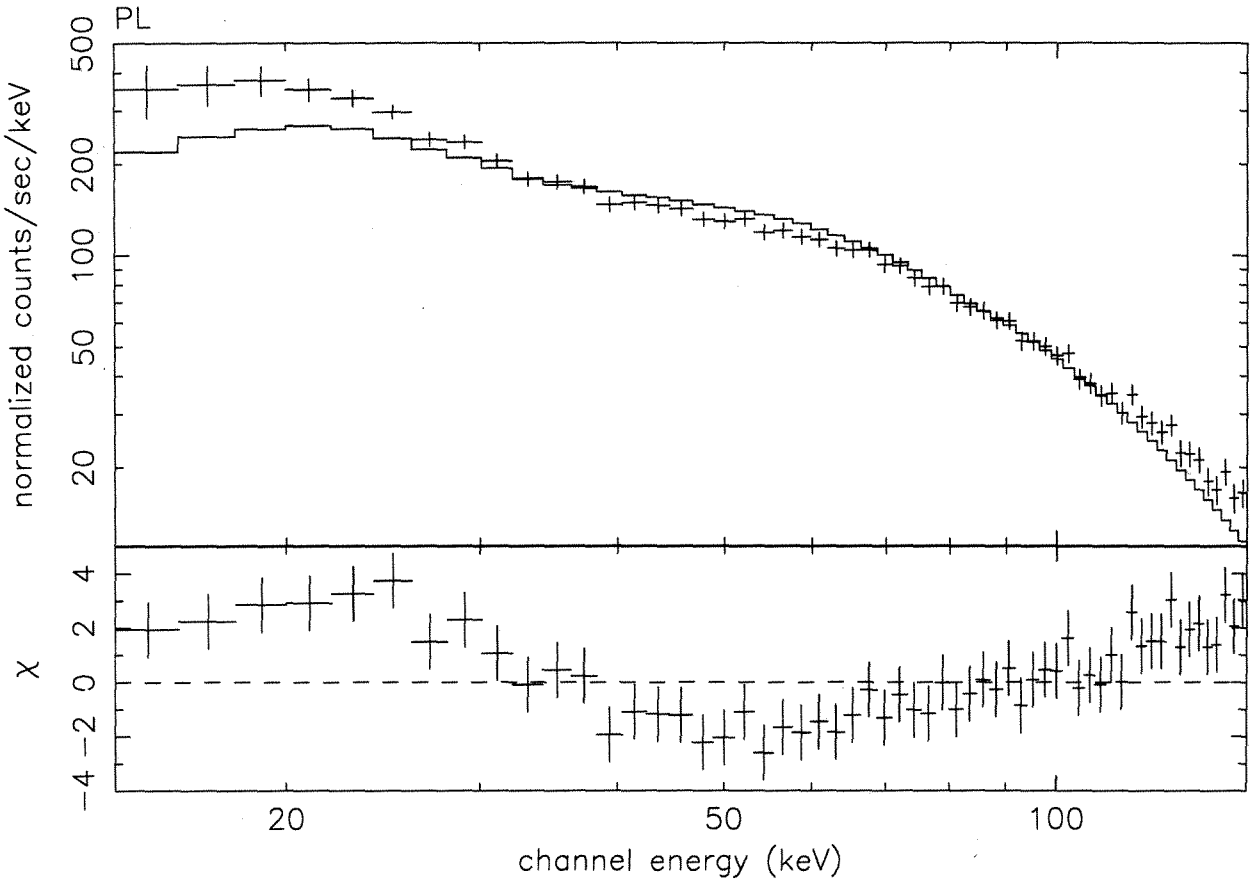

Fig. 24.— The simulated BAT spectrum of the *Fermi* GRB 090902B interval b spectral parameters as the input spectrum. The best fit spectral model (solid line) is a PL.

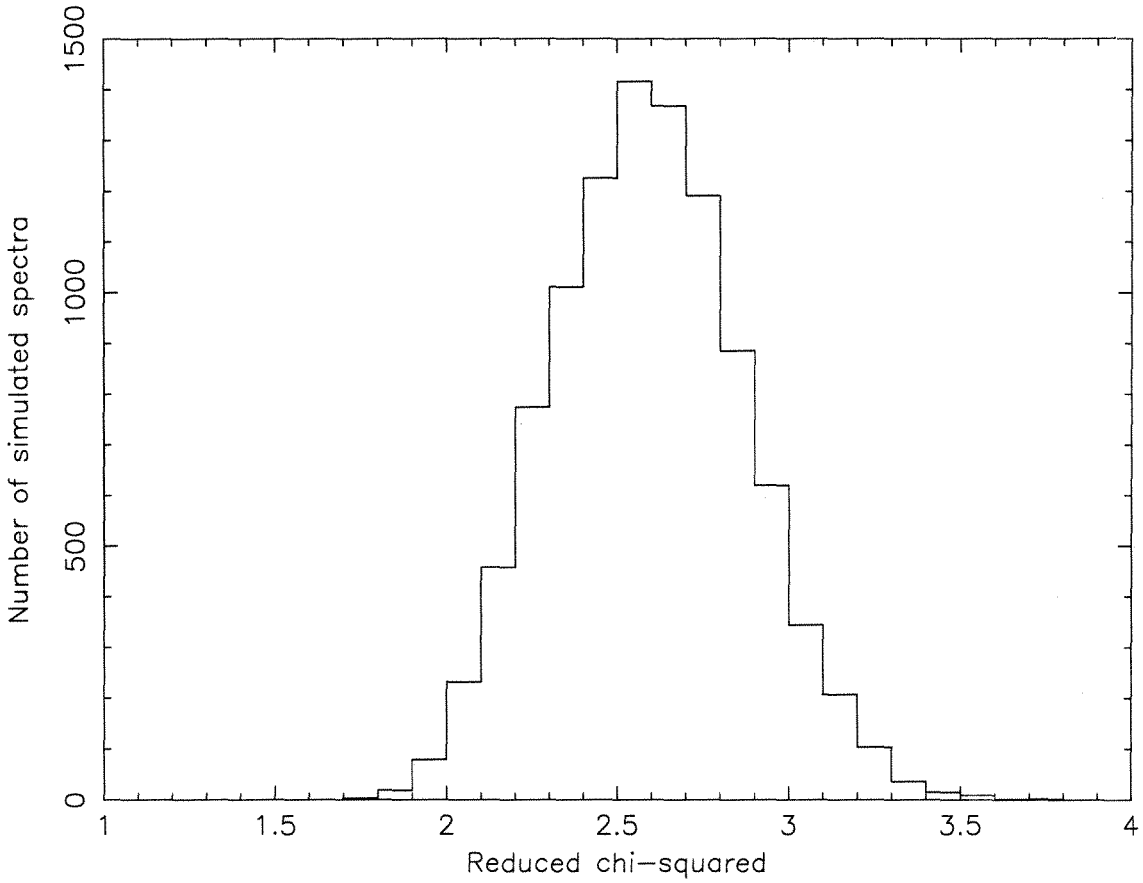

Fig. 25.— Histogram of reduced χ^2 in a PL fit of 10,000 BAT simulated spectra of the *Fermi* GRB 090902B interval b spectral parameters as the input spectrum.

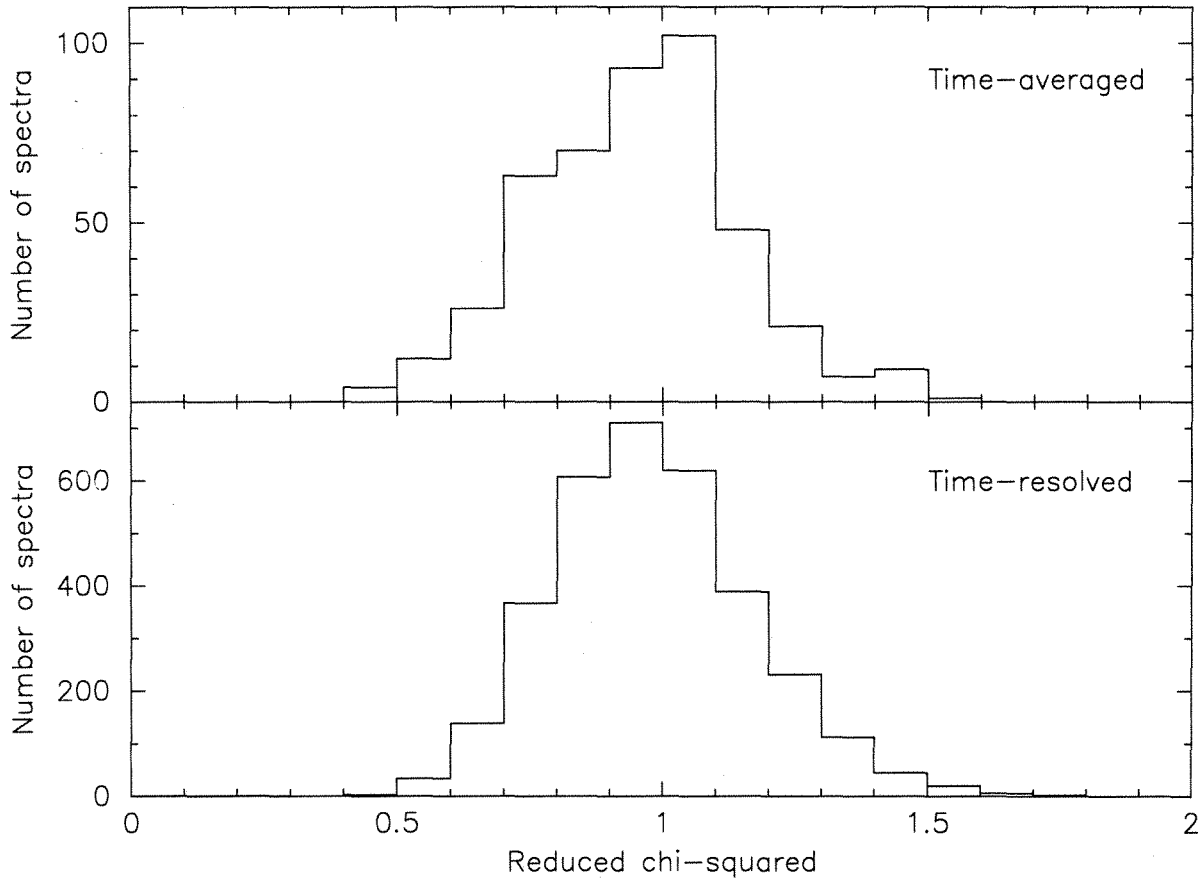

Fig. 26.— Histogram of reduced χ^2 in the best fit model (either a PL or a CPL model) for the time-averaged spectra (top) and the time-resolved spectra (bottom). The Gaussian fit to the histograms shows the peak of 0.95 with a σ of 0.19 and the peak of 0.96 with a σ of 0.18 respectively.

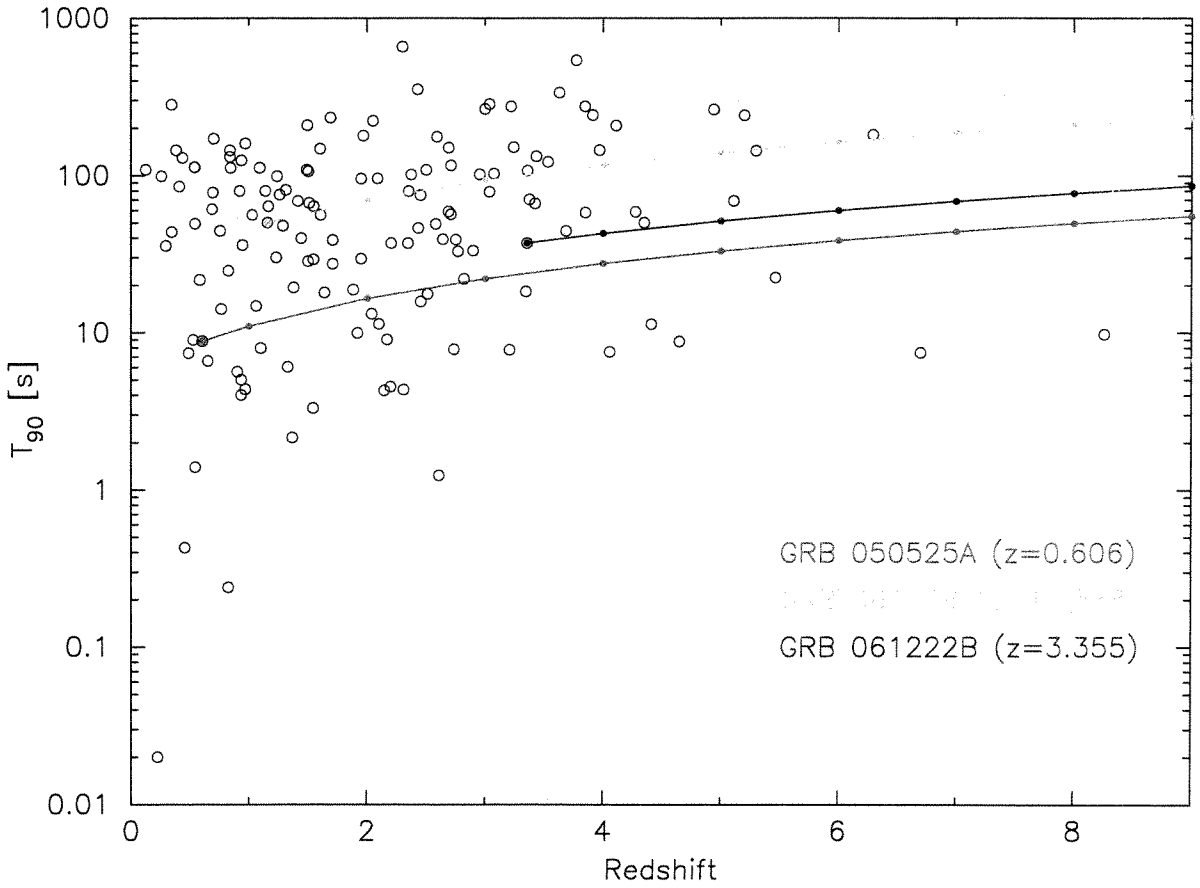

Fig. 27.— Distribution of the BAT observed T_{90} vs. redshift. For three known redshift GRBs, GRB 050525A (z=0.606), GRB 061126 (z=1.1588) and GRB 061222B (z=3.355), we calculated the trajectories of estimated observed T_{90} as a function of redshift assuming that the duration changes only by the time-dilation effect.

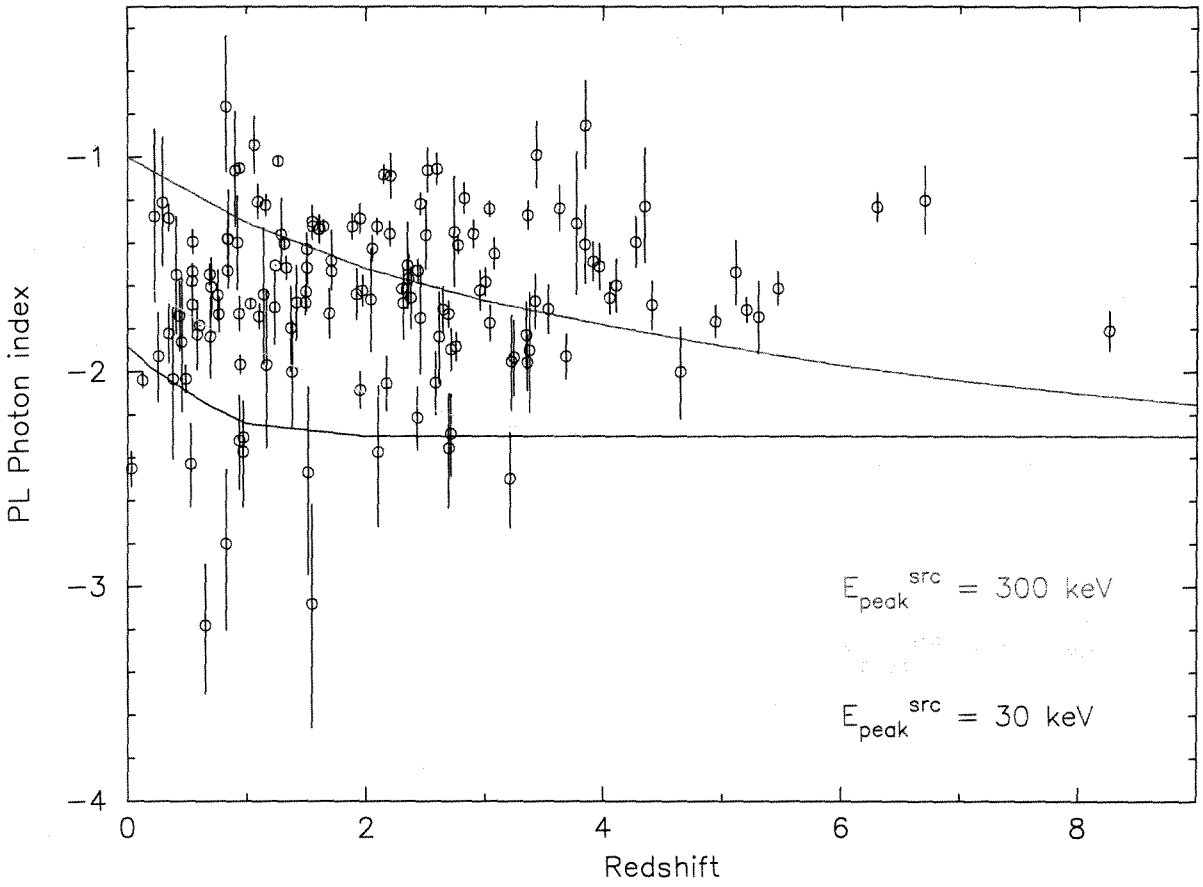

Fig. 28.— Distribution of the BAT observed PL photon index vs. redshift. The overlaid curves are the estimations of the BAT observed PL photon index as a function of redshift assuming the observed BAT PL photon index is the redshifted spectrum of the typical Band function shape with the rest-frame $E_{\rm peak}$ of 300 keV (red), 100 keV (green) and 30 keV (blue).

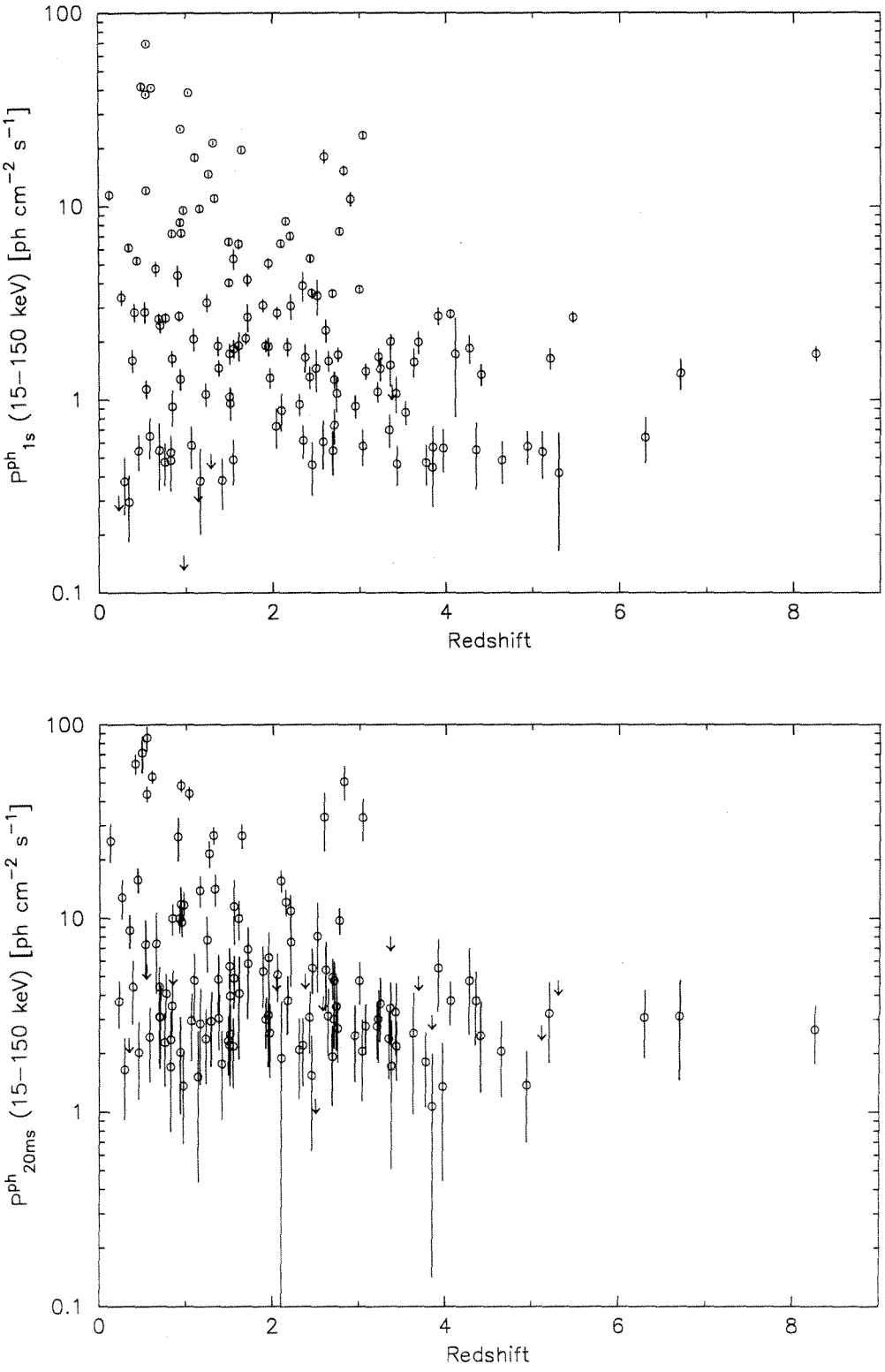

Fig. 29.— Distribution of 1 s (top) and 20 ms (bottom) observed peak photon flux in the 15-150 keV band vs. redshift.

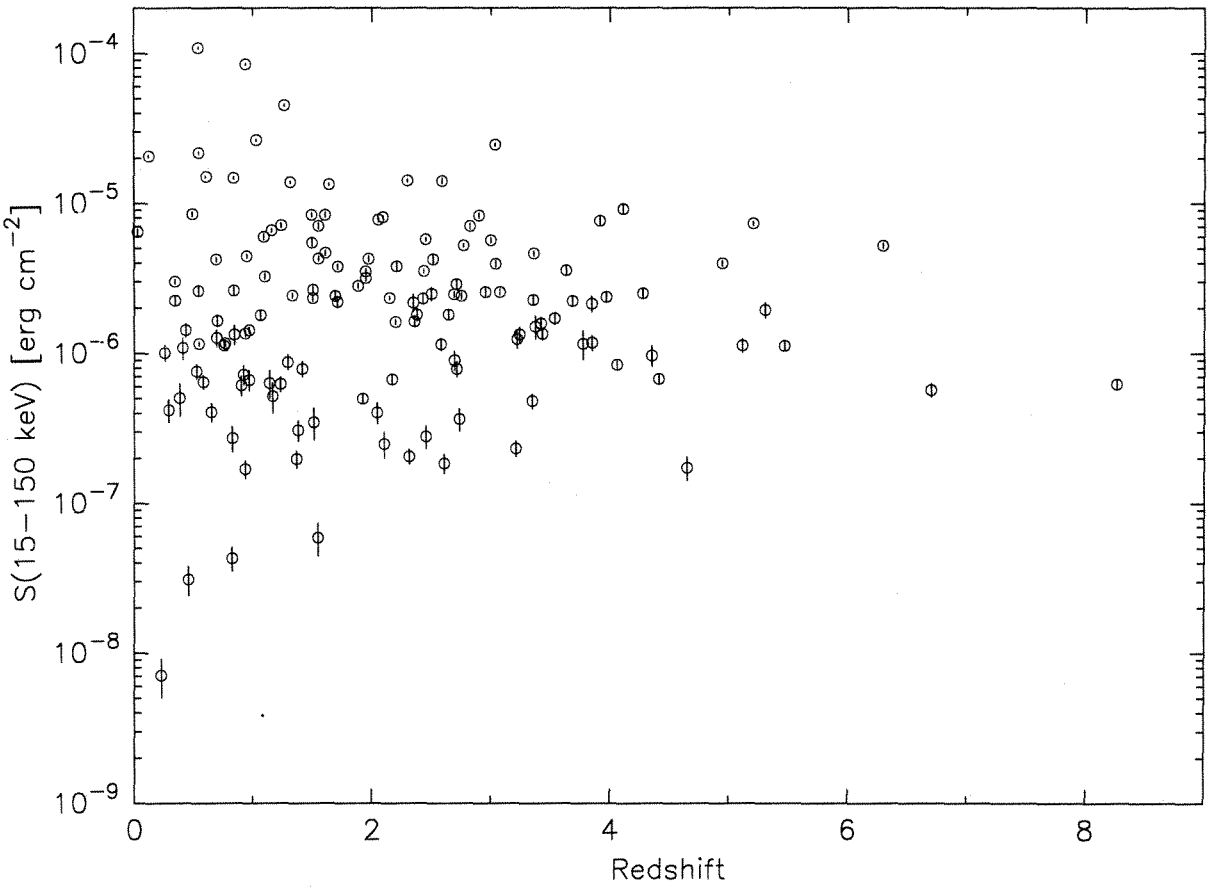

Fig. 30.— Distribution of the BAT observed energy fluence in the 15-150 keV band vs. redshift.

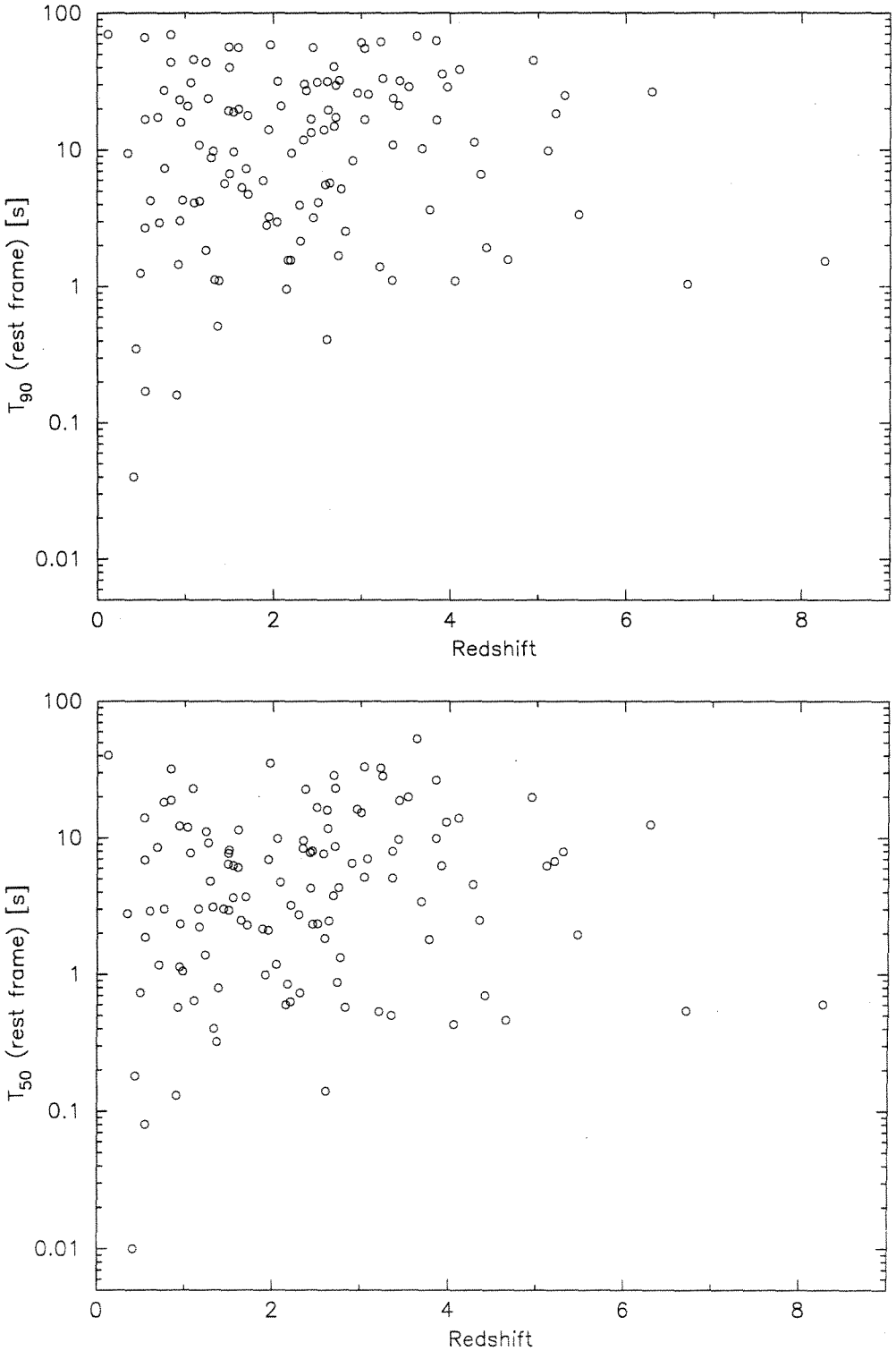

Fig. 31.— Distributions of T_{90} (top) and T_{50} (bottom) in the 140-220 keV band at the GRB rest frame vs. redshift.

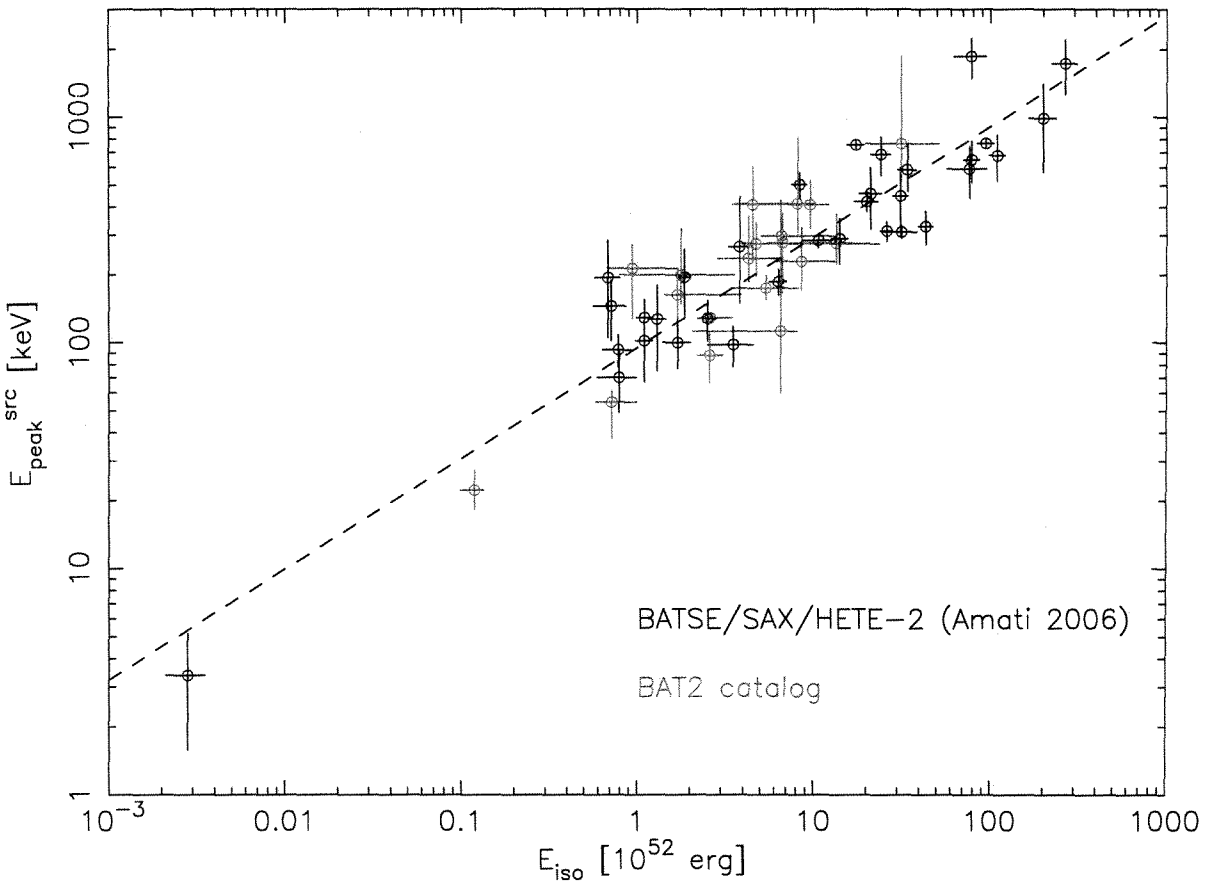

Fig. 32.— The correlation between $E_{\rm peak}^{\rm src}$ and $E_{\rm iso}$ for the *Swift* GRBs (red) and other GRB missions (black). The dashed line is the best fit correlation between $E_{\rm peak}^{\rm src}$ and $E_{\rm iso}$ reported by Amati (2006): $E_{\rm peak}^{\rm src} = 95 \times (E_{\rm iso}/10^{52})^{0.49}$.